Λ/η ;/ ,η"7

/Λ/ :...

0S '...3

EXPERIMENTAL MEASUREMENTS OF THE LAMINAR SEPARATION BUBBLE /... ON AN EPPLER 387 AIRFOIL AT LOW REYNOLDS NUMBERS

Gregory M. Cole and Thomas J. Mueller

NSG 1419

FORWARD

The work reported herein was performed by the Department of Aerospace and Mechanical Engineering, University of Notre Dame, for NASA Langley Research Center, Hampton, Virginia under Contract No. NSF 1419. The technical direction was provided by R.J. McGhee. Additional support necessary to bring this work to a meaningful conclusion was supplied by the University of Notre Dame. This research was performed between September 1, 1988 and December 31, 1989. The material in this report was submitted by the first author as a thesis in partial fulfillment of the requirements for the Degree of Master of Science in Aerospace Engineering.

EXPERIMENTAL MEASUREMENTS
OF THE LAMINAR SEPARATION BUBBLE
ON AN EPPLER 387 AIRFOIL AT LOW REYNOLDS NUMBERS

Abstract

An experimental investigation was conducted to measure the flow velocity in the boundary layer of an Eppler 387 airfoil. In particular, the laminar separation bubble that this airfoil exhibits at low Reynolds numbers was the focus of the study. Single component laser doppler velocimetry data were obtained at a Reynolds number of 100,000 at an angle of attack of 2.0°. Static Pressure and flow visualization data for the Eppler 387 airfoil were also obtained. The difficulty in obtaining accurate experimental measurements at low Reynolds numbers is addressed. Laser doppler velocimetry boundary layer data for the NACA 66_3-018 airfoil at a Reynolds number of 160,000 and angle of attack of 12° is also presented.

TABLE OF CONTENTS

LIST OF FIGURES

NOMENCLATURE

AR_b	bubble aspect ratio, $AR_b = l_1 / h_b$
c	airfoil chord
C_L	section lift coefficient
C_M	section moment coefficient
C_p	pressure coefficient, $C_p = (P - P_\infty) / q_\infty$
h_b	bubble height, $h_b = \delta_{1t} - \delta_{1s}$
H_T	height of transition
H_{12}	shape factor, $H_{12} = \delta_1 / \delta_2$
H_{32}	shape factor, $H_{32} = \delta_3 / \delta_2$
l_B	length of laminar separation bubble, $l_B = l_1 + l_2$
l_1	length of laminar region of separation bubble
l_2	length of turbulent region of separation bubble
P	local static pressure
P_∞	freestream static pressure
q_∞	freestream dynamic pressure
R_c	Reynolds number based on chord, $R_c = U_\infty c / v$
R_{l_1}	Reynolds number based on l_1, $R_{l_1} = U_e l_1 / v$
R_{δ_1}	Reynolds number based on δ_1, $R_{\delta_1} = U_e \delta_1 / v$
R_{δ_2}	Reynolds number based on δ_2, $R_{\delta_2} = U_e \delta_2 / v$
U	local tangential velocity component
U_e	external or edge velocity
U_{ext}	external or edge velocity
U_∞	freestream velocity

x	distance along airfoil chord from leading edge
y	normal height above airfoil surface
y_D	dividing streamline height

Greek Symbols

α	angle of attack
γ	separation angle, $\gamma = \tan^{-1}((\delta_\tau - \delta_s) / l_1)$
δ	boundary layer thickness
δ_1	boundary layer displacement thickness, $\delta_1 = \int_0^\delta (1-U/U_e)dy$
δ_2	boundary layer momentum thickness, $\delta_2 = \int_0^\delta (U/U_e)(1-U/U_e)dy$
δ_3	boundary layer energy thickness, $\delta_3 = \int_0^\delta (U/U_e)(1-(U/U_e)^2)dy$
μ	absolute viscosity of air
ν	kinematic viscosity of air, $\nu = \mu / \rho$
ρ	density of air

Subscripts

c	airfoil chord
e	external or edge of boundary layer
r	reattachment
s	separation
t	transition
∞	freestream condition

Abbreviations

LDV	laser doppler velocimetry

CHAPTER I

INTRODUCTION

1.1 Background

Interest in low Reynolds number aerodynamics has increased as new technology has opened up flight regimes previously thought impractical or even unattainable. The advancements made in materials and electronics make small remotely piloted vehicles (RPV's), large high altitude RPV's, man powered aircraft, solar powered aircraft, and very high aspect ratio aircraft, wind turbines, and small gas turbine blades possible. These applications all operate at low Reynolds numbers. Mueller (1985) gives a more comprehensive overview of low Reynolds number applications and Drela (1988) provides an interesting study of human powered aircraft low Reynolds number aerodynamics.

Reynolds number is a dimensionless quantity that relates viscous forces to inertial forces for fluids in motion. By definition Reynolds number is a function of a characteristic length, velocity, density, and absolute viscosity. Low Reynolds number can now be thought of as referring to flows in a given fluid were the velocities and physical dimensions are small. The term low Reynolds number for these applications refers to R_c in the range from 50,000 to 500,000. This is far from the creeping or all laminar flow regime, but below that usually associated with manned flight. It is interesting to note that most birds operate in this Reynolds number range. Very low Reynolds number flows, Reynolds numbers below 10, are fully laminar and can be solved analytically. High Reynolds number flow around an airfoil can be accurately solved with the help

of boundary layer theory. In this case it is assumed that viscous effects are confined to a thin layer next to the surface and are solved by simplified boundary layer equations, while the flow outside the boundary layer is considered inviscid.

1.2 Low R_c Airfoil Flow Field

The low Reynolds number flow regime is particularly difficult. The flow field features laminar and turbulent flow , separated flow, and large wakes. Low Reynolds number laminar boundary layers are relatively stable or in this case persistently so. This laminar boundary layer that forms on the forward surface is unable to resist any appreciable adverse pressure gradient of the form that exists behind the pressure peak on an airfoil. The flow separates forming a laminar shear layer. This shear layer is not a free shear layer as the close proximity of the airfoil surface stabilizes it but it is less stable than an attached boundary layer. The initial laminar shear layer transitions over a length into a turbulent shear layer by amplification of disturbances present in any flow. The common form of these amplified disturbances are two dimensional Tollmein-Schlichting waves. A turbulent shear layer is a good conductor of momentum through the boundary layer and entrains high momentum fluid from the outside flow, thus thickening rapidly. The transition process is complete when this turbulent shear layer contacts the airfoil surface and becomes an attached turbulent boundary layer. If the separated shear layer, laminar or turbulent, does not reattach the airfoil flow field is subcritical. Subcritical flows are characterized by large wakes and extensive laminar flow. This entrainment of fluid results in a turbulent boundary layer that is thicker than a turbulent boundary resulting from an attached transition process. In a mean sense the shear layer encloses a region of fluid near the airfoil's surface. The enclosed

fluid and the separated shear layer is called a laminar separation bubble. Also the enclosed region of fluid exhibits one or more recirculation zones. Figure 1.1 shows a general bubble model and its assumed flow field (Horton 1968). In general a laminar separation bubble will reduce an airfoil sections lift and increase drag compared to an attached transition process but is preferable to the massive wake that results from laminar separation without reattachment.

Laminar separation bubbles can occur on both airfoil surfaces, sometimes simultaneously, and alter the pressure distribution around the airfoil. This change in the pressure distribution manifests itself as a reduction in the pressure peak (from that expected by an inviscid flow) followed by a pressure plateau. Figure 1.2 shows the pressure distribution on an airfoil with a laminar separation bubble. The pressure plateau location is coincident with that of the laminar portion of the separation bubble. The transition to turbulent flow results in a rapid pressure rise brought about by fluid entrainment. This pressure rise often overshoots the inviscid pressure that would exist at the reattachment location. The location of the point of equality between the actual and inviscid pressure marks the location of reattachment. At this point a simple distinction between short and long bubbles will be made. A short bubble will only slightly perturb the airfoil's pressure distribution while a long bubble significantly changes the pressure distribution. A bubble also produces a thick turbulent boundary layer that is susceptible to turbulent separation. Turbulent separation will further increase drag and reduce lift while also altering the airfoil pressure distribution. This in turn affects bubble size and location. This coupling of characteristics is what makes this flow regime so difficult to model.

Another difficult feature of low Reynolds number aerodynamics is a phenomena called hysteresis. Hysteresis can occur in lift , drag, and moment characteristics of airfoils with separation bubbles (Mueller (1985), Marchman

(1987), McGhee (1988), Selig (1984), and Althaus (1986)). Hysteresis results when a laminar separation bubble behaves differently for increasing angle of attack than for decreasing angle of attack, thus affecting aerodynamic characteristics like lift, drag, and moment. This presents a serious problem for those interested in stability and control of vehicles operating at low Reynolds numbers. Two types of hysteresis are most common, pre-stall and stall hysteresis.

Pre-stall hysteresis is associated with long bubbles located at mid-chord. If angle of attack increases from a low value the bubble extends aft and may even extend into the wake to create a trailing edge stall. As angle of attack is further increased the flow transition point moves forward and a short bubble forms near the leading edge. If at this point angle of attack is reduced the bubble will jump back to a mid chord location at a lower angle than that for the initial formation of the short bubble.

Stall hysteresis is usually associated with a short leading edge bubble. As angle of attack increases the bubble bursts, extends across the airfoil without reattachment. The bursting destroys the airfoil's pressure peak with a resulting drastic reduction in lift that is like a leading edge stall. If angle of attack is reduced the bubble shortens at an angle lower that that for bubble bursting.

1.3 Scope of Present Work

The interdependence of the flow field characteristics of low Reynolds number aerodynamics such as laminar separation, transition, turbulent reattachment, and turbulent separation has slowed the formulation of empirical and analytical models. Accurate experimental results are useful for development of new models and comparison with computational solutions.

Increasing the low Reynolds number data base was the primary function

of the research presented in this study. Boundary layer data for this purpose was obtained by LDV measurements. The advantage of this method over the more commonly used hot-wire anemometry method is the ability to discern flow direction and magnitude unobtrusively and directly. Data for two airfoils supporting two different types of laminar separation bubbles is presented. Measurements on the Eppler 387 airfoil include LDV boundary layer profiles at $R_c = 100,000$ and $\alpha = 2.0°$ across the upper surface, with particular emphasis on the bubble region. The conditions and model size, chord = 304.8 mm, were chosen to give a large steady bubble. LDV boundary layer measurements were also made on the upper surface of a NACA 66_3-018 airfoil at $R_c = 160,000$ and $\alpha = 12.0°$. This exact airfoil model has previously been tested at Notre Dame with hot-wire and LDV techniques.

The results of this research are presented with particular emphasis on measurement uncertainty and errors. The low Reynolds number regime provided a challenge for the measurement techniques used. Some of the factors involved include low velocities, small physical dimensions, and unsteadiness in the flow field of interest. The specific details of which are discussed later in this thesis.

CHAPTER II

EXPERIMENTAL APPARATUS

The Notre Dame Aerospace Laboratory was the site for this research. All equipment and facilities are housed in this building. The south low speed wind tunnel was utilized for all experiments. These include the flow visualization, static pressure measurements, and the laser doppler velocimetry (LDV) boundary layer measurements.

2.1 Wind Tunnel

The wind tunnel used in this investigation is the south low speed low turbulence wind tunnel originally designed by F. N. M. Brown for low speed flow visualization. This is an open circuit indraft type tunnel with square cross section through the inlet and test section with a transition to a circular cross section in the diffuser. The inlet features a 3-D 24:1 contraction ratio from 2.95m square to 0.61m square in 1.48m. Preceding the inlet are twelve anti-turbulence screens. The same test section was used for all experiments. This section featured three plate glass side walls, one plexiglass back wall with a model sting holder, and measured 0.61m x 0.61m x 1.83m internally. A diffuser with 4.2 degree half angle leads to the eight bladed 1.2m diameter fan driven by an 18.6 kW variable speed A.C. motor. Figure 2.1 shows a dimensioned layout of the wind tunnel. Figure 2.2 shows the test section used and the positions of the

model and the pitot tube.

2.2 Airfoil Models

The Eppler 387 airfoil models were constructed in the Aerospace Laboratory shop by machining an aluminum master plug and constructing molds from which models could be cast in epoxy. The airfoil models used had a 0.3048m chord and quarter chord sting mount location and various spans. The coordinates for the Eppler 387 airfoil were provided by NASA Langley and are tabulated in Table 2.1. Three models were used in the various tests. The surface/smoke flow visualization and pressure models had a 0.406m span. These models were mounted centered in the tunnel cross section between 0.61m x 0.61m plexiglass endplates. These endplates featured round leading and square trailing edges and located the airfoil quarter chord location 0.267m from the leading edge of the endplate. The pressure model included 66 ports for static pressure measurement. These ports are 0.79mm in diameter and are normal to the airfoil surface. All ports lead into Teflon tubing of 1.78mm O.D. and 1.27mm I.D.. Port positions are staggered along the span at a 60° angle to the leading edge. This was done to reduce port disturbance effects of upstream taps. Pressure port distribution is tabulated in Table 2.2 with both chord wise and normal coordinates given. The LDV model extended from one tunnel side wall to the other with a 0.61m span and was used without endplates.

2.3 Data Acquisition Equipment

A computer based data acquisition system was used to record data during pressure and LDV measurements. This system is based on a PDP 11/23 mini computer. This PDP 11/23 was configured with a Data Translation DT 2752 DMA 12 bit A/D, DEC DWV11-C real time clock, and an AAVII-C 12 bit

D/A. The A/D was configured to read up to eight channels with software adjustable gains of 1, 2, 4, and 8. This system had an input voltage range of plus or minus ten volts and a best resolution of plus or minus 0.61 mV (O'Meara 1985). The D/A is capable of four channels of plus or minus ten volts output. A PDP11/34 mini computer was used for data reduction and data plotting through Hewlett Packard 7470 A plotters.

2.4 Flow Visualization

Three types of flow visualization were utilized in this study. The primary goal of this research was documentation of the laminar separation bubble. As an initial investigation surface flow visualization was used to located the bubble. The flow structure of the bubble was photographed with smoke wire visualization. Smoke streak lines generated buy a kerosene smoke generator and smoke rake were used to study the macroscopic flowfield.

The smoke rake and generator were developed by F. N. M. Brown and are shown in Figures 2.3 and 2.4 respectively. This apparatus was also used to seed the flow for LDV measurements. This system operates by vaporizing kerosene dripped on electric strip heaters. The resulting smoke is then filtered, cooled, and distributed by the smoke rake. This smoke rake is adjustable in height by a remotely controlled electric motor.

Surface flow visualization utilized a fluorescent mixture of fluorescene, water, and photo flow. Black light illumination by two 40W bulbs allowed viewing of the bubble location by variations in the fluorescent intensity. This variation is due to visualization fluid flow thickness changes driven by external flow shear stress.

Smoke wire flow visualization produced smoke by vaporizing model train smoke fluid applied to a 0.003 inch diameter stainless steel wire. Illumination

for photography was provided by three General Radio model 1540 strobe lamps. These were positioned above the tunnel test section and projected light through a 0.025m slit masked off on the upper glass . Synchronized flash and smoke production was accomplished by a specially constructed control unit. This unit was developed by Mueller (1980) and by Batill (1980) for smoke wire photography. This control unit passed an adjustable current through the smoke wire for a specified time. After a set delay this unit triggered the camera shutter. The strobes were fired simultaneously by the camera's flash synchronization system. The only unique feature to this system is the position of the smoke wire. It is positioned in the spanwise direction at some point along the airfoils chord by specially made thin brass wire holders. These allowed the wire to be positioned at various heights from the airfoil surface and chord positions. The wire mounted directly to the airfoil model and no holes through the endplates were necessary. Flush mounting of these holders allowed the airfoil model to butt up against the endplates.

Photographs were taken in 35mm format by SLR cameras with a variety of focal lengths. Negatives and prints were processed in the Aerospace Laboratory's dark room.

2.5 Pressure Measurement Equipment

Pressure measurements were made by Spectra Systems Model 339H electronic manometers. Manometers with a pressure range of 0-140.6 mm H_2O and an analog output proportional to pressure of 0-5 volts were used. These manometers have a listed accuracy of ± 0.2mm H_2O. In all experiments a pitot static tube system utilizing this electronic manometer was used to determine tunnel flow speed.

Static pressure measurements on the Eppler 387 airfoil were conducted

utilizing a specially constructed model that had 66 pressure ports distributed around the cross section. The experimental setup is shown in schematic form in Figure 2.5. Pressure measurements were not made simultaneously but rather computer D/A controlled Scanivalves were used to divert airfoil static pressure to a single electronic manometer. The Scanivalve model-J 48 port Scanivalve was controlled by a modified model CTLR10/52-56 solenoid controller. This controller allows computer control of Scanivalve port step and home reset actions. Two manometers were used, one to measure tunnel speed and the other to measure airfoil static pressure, with their total pressure ports connected together. This feature is used to prevent the introduction of a pressure bias due to pressure drop across the anti-turbulence screens.

2.6 Laser Doppler Velocimetry

LDV is a non intrusive method to measure velocity, i.e. it can resolve flow speed and direction. In this experiment a forward scatter single component mode with frequency shifting was used. Frequency shifting allows resolution of flow direction. The LDV system consists of an argon laser, transmitting and receiving optics, signal processors, traversing equipment, and a kerosene smoke generator and rake for flow seeding.

The laser is an XL5000 manufactured by Excel. It is a blue-green 5W argon type that was used in a monochromatic mode with a wave length of 514.5 nm. Beam diameter is 1.2 mm measured to $1/e^2$ of the center intensity.

All optics were manufactured by TSI except where noted. Proceeding from the laser head the transmitting optics include a 91108 collimator to prevent beam divergence, 902-12 polarizer, 915-1 beamsplitter, 9182-11 spacer, 9182-12 Bragg cell with a model 9186A LV frequency shifter, 913 beam aligner, 9188A beam expander, 9181-2 beam blocker, and a model 939 focusing lens

with a 578.6 mm focal length. These components were supported on 9178-1 and 9179 optics stands. This system had an ellipsoidal measuring volume 0.14mm in diameter and 3.22 mm long. The receiving optics included a 9167-500 lens. This is a 500 mm focal length lens with k=2.81. Also included are model 9140 receiving optics body, a model 962 photomultiplier with a model 965 photomultiplier power supply, a model 976 beam pin hole blocker, and two model 976 optic stands.

The signal processor operates as the final link between the optical hardware's photomultiplier signal and the final analog output that represents flow velocity through the measuring volume. Processing of the photomultiplier signal was performed by the 9186A LV frequency shifter to account for laser light frequency shifting in the Bragg cell. The photomultiplier signal is created by the passage of particles through the measuring volume and is called a doppler burst. This doppler signal contains a frequency component created by geometric scattering, for the fringe spacing and particle diameters used in this experiment, of laser light in the measuring volume. Fringe spacing was 3.91 μm and the optimal particle diameter for this spacing was 0.98 μm. A low frequency component was also present as a result of intensity variations across the laser beam diameter. High frequency components were present when multiple particles passed through the fringes of the measuring volume and from signal noise. Band-pass filtering by the model 1994B input conditioner was used to select the correct frequency component that corresponds to the flow velocity. Further signal selection was based on the number of fringes that are crossed by a given particle. This selection is based on a cycles per burst criterion, where a cycle is created by a fringe crossing. Cycles per burst were measured in the 1995B timer module, time mode output was displayed in volts on the 1992 readout module, and the 1988 analog output module allowed the PDP 11/23

A/D to read a voltage inversely proportional to the velocity measured (doppler frequency). The computer A/D was incapable of reading data as fast as the signal processor. Therefore, a data ready pulse sent from the latter was used to trigger a Rutherford Electronics Model 814 pulse generator that sent periodic signals to a Schmitt trigger on the PDP 11/23. The output of the photodetector and the filtered output were monitored by two oscilloscopes. A schematic of the set LDV apparatus is shown in Figure 2.6 .

The flow field that needed to be sampled by the LDV required a 2-D traversing system. This system used a fixed arrangement of laser, transmitting, and receiving optics connected by a space frame. This arrangement was required for alignment of the forward scatter optics and was possible because of the transparent test section walls. The traversing system utilized a Bridgeport milling machine for three axis translation of the LDV system. All LDV components were attached to a Thermal Systems Inc. TSI model 9127 table that was gridded by threaded holes. This table replaced the milling machine head. The receiving optics were attached to this table by a space frame composed of thin wall tubing. This configuration maintained alignment between the transmitting and receiving optics. Figure 2.7 shows the LDV traversing system and its relation to the test section. This traversing system was capable of translation with a 0.0254mm least count by manual turning of lead screws.

The LDV measuring volume was seeded by kerosene smoke. The smoke generator and smoke described previously were used for this purpose. The smoke rake was positioned so a smoke streak line passed through the measuring volume. The kerosene smoke consisted of small droplets of kerosene that range in size from 1.0 to 3.0 microns at the smoke generator temperatures used (Visser 1988).

CHAPTER III

EXPERIMENTAL PROCEDURE

The experiments conducted on the Eppler 387 airfoil profile were intended to characterize the laminar separation bubble. To accomplish this several flow visualization as well as LDV and static pressure measurement techniques were used. The experiments were conducted at a Reynolds number of 100,000 based on a 304.8 mm chord and at 2° angle of attack. This test regime was chosen to study a laminar separation bubble of large physical dimension in a flow field with little turbulent separation of the boundary layer. This type of flow field would lessen the inherent unsteadiness of the turbulent reattachment process in the laminar separation bubble by reducing unsteadiness of the wake. Previous investigators (McGhee 1988) have determined the bubble to occupy around 40% of the airfoil's chord length at these conditions. It was felt that this would be a good addition to work that has previously been done at Notre Dame. This includes LDV measurements of a short bubble of about 6% chord on the NACA 66_3-018 airfoil (Fitzgerald, 1988) and this investigator) and the longer bubble on the Wortmann FX63-137 airfoil (Brendel, 1987). The flow conditions for the Eppler 387 require steady free stream velocities of approximately 5 m/sec at as low a turbulence intensity as possible. The freestream turbulence level affects the laminar separation bubble transition process. O'Meara (1985) contains test results that show the affects of freestream turbulence intensity on boundary layer parameters; while McGhee (1988) shows the affects of turbulence on aerodynamic characteristics like lift, drag, and moment. This required running all tests when the atmospheric

conditions were dead calm, i.e. wind speeds of 5 km/hr or less. No flow restrictors were used between the test section and diffuser. While flow restrictors can provide steadiness for large scale fluctuations, like wind gusts, they increase the tunnel turbulence intensity (O'Meara 1985).

3.1 Flow Visualization

The Notre Dame facility is particularly well suited for flow visualization due to its low turbulence open circuit design. The following methods were used in the study: fluorescent surface flow, smoke wire, and smoke tube visualization.

3.1.1 Fluorescent Surface Flow Visualization

This method is commonly used for determination of separation and reattachment locations. This experiment posed special problems due to the very low velocities and resulting low surface shear stresses. The visualization fluid viscosity was adjusted to the minimum that would still allow full surface wetting. This method required the test section to be opened and a thin layer of fluid painted on the model's surface. The tunnel motor was left on during this procedure. The flow pattern develops over time and was recorded photographically when the pattern was observed to be the most distinct. Illumination was provided by a black light placed above the tunnel test section. After each run the model's surface was cleaned to reduce fluid buildup that could alter the flow.

3.1.2 Smoke Wire Flow Visualization

Smoke wire flow visualization inside the laminar separation bubble was undertaken in an attempt to get away from titanium tetrachloride ($TiCl_4$). $TiCl_4$ produces a dense brilliant white smoke upon contact with the moisture in the air

but it also holds a few associated disadvantages. These include toxicity and harmful corrosive vapors. The most pressing reason to look for a new method was the possibility of introducing disturbances into the boundary layer with the $TiCl_4$ injection process. These disturbances could alter the boundary layer characteristics or induce premature transition in the bubble. An alternative method of surface application of titanium tetrachloride could eliminate some problems but precipitate build up on the model will still affect the boundary layer.

The smoke wire method was designed to eliminate these difficulties. The spanwise smoke wire was located at 75% of the chord on the upper surface very close to the model's surface. The Reynolds number of the wire based on diameter was about 2. This very low Reynolds number and the wires location in or very near the turbulent portion of the bubble reduced its effect on the bubble flow field. The disturbance of the boundary layer due to wire heating and buoyancy effects was minimized by the both location of the wire and the time delay between smoke production and shutter opening. Heated air was quickly mixed with cooler ambient air and transported upstream and downstream by the turbulent aft portion of the bubble. The disturbance influence on the sensitive laminar shear layer was also reduced by its introduction into the turbulent region.

The procedure used an adjustable time length and variable amperage current for the smoke wire heating. An adjustable time delay between wire heating and camera triggering allowed the smoke streak lines to fill the flow field of interest and to reduce the affects of the heated air on the flow characteristics. The smoke was produced by vaporizing oil that is applied to the wire with a small sponge brush. Smoke wire current was adjusted to a minimum setting that would still produced uniform dense smoke. The time of

current application was adjusted to allow complete oil vaporization. The settings described were optimized by trail and error and the time delay to camera shutter opening was 1.5 to 3.0 seconds.

3.2 Static Pressure Measurements

The static pressure measurements made on the Eppler 387 airfoil were done sequentially. The pressure measurements started at the leading edge and proceeded along the upper surface to the thirty third port (64% x/c) at which point the second Scanivalve was used to sequence ports. Measurements continued to the trailing edge and then covered the lower surface from the leading to trailing edge. At each port location 100 data points were taken at 100 Hz after a 1 second delay. This process was automated and run by computer software that also reduced the data and stored it on disk in pressure coefficient form. The standard form for pressure coefficient, C_p, was used. This data was later reduced to obtain integrated lift and pitching moment coefficients.

3.3 Laser Doppler Velocimetry

This form of velocity measurement was capable of measuring flow direction and magnitude of a velocity component. This gave it obvious advantages over hot-wire measurements, which only measure a flow magnitude and direction is assigned, in flow situations where reverse flow occurs. One such situation occurs in laminar separation bubbles. The major disadvantages included the slow speed of boundary layer measurements and the critical importance of proper bandpass filtering. The measurement of a single boundary layer velocity profile required about an hour and a half under ideal conditions.

The laminar separation bubble on the Eppler 387 airfoil was investigated

with the measurement of mean velocity profiles at thirty chord stations on the upper surface. These profiles are located upstream, in, and downstream of the bubble. The LDV data acquisition software was originally written by Brendel but used with modifications by Fitzgerald and this investigator. The measurement procedure began with model setup. The model was aligned in the tunnel normal to the side walls at the desired angle of attack. Position of the LDV system was aided by the use of the laser as a horizontal plumb. Careful initial positioning of the milling machine allowed measurements at all chord positions and heights without further adjustments to alignment. A pitot tube and electronic manometer were used to set tunnel velocity for a desired Reynolds number given the ambient conditions. Uncertainty in tunnel free stream velocity was 0.32 m/sec (about 6% of the freestream velocity), at R_c = 100000 and c = 304.8 mm, due to manometer uncertainty alone.

The initial step in the measuring process was the positioning the LDV probe volume at the desired chord position. The airfoil model has chord positions lightly scribed onto the upper surface for probe location. The probe volume was moved in a spanwise direction to a plane coincident with that of the seeding smoke tubes. Measurements were not made in the same plane as the scribings to reduce any roughness induced effects. In this position the plane of the beam crossing was aligned to be tangent to the airfoils surface and the probe height was zeroed. The former was easily accomplished by lowering the probe volume to a point just below the airfoils surface and observing the intersection of the beams on the model surface. The plane of crossing was adjusted until the length of the beam reflections were the same. The angle of this plane to horizontal was calculated by the software but usually differed slightly (< 1.0°, which was the least count of the angular displacement scale) from the angle visual inspection suggested. In these cases the angle obtained

visually was used. The zero height position of the probe was obtained by inspection of the signal from the photomultiplier. When approximately half of the probe volume was in the freestream and half reflected from the model's surface the photomultiplier signal was sinusoidal with frequency equal to the shift frequency. Initial height position uncertainty was on the order of the measuring volume diameter (0.14 mm) with this method. Finally the height of the smoke rake was adjusted so that a smoke streak line impinged at the airfoils stagnation point.

Measurements were made with normal increments of 0.3mm inside the boundary layer and larger increments outside. Increments normal to the airfoil surface were reduced by the software into horizontal and vertical components for manual adjustment of lead screws on the milling machine. At each measurement location 500 data points were taken and averaged to get a mean velocity. Previous measurements in the freestream had shown the average velocity change from one measurement to the next to reach a minimum for measurements averaged from 400 samples. This is a qualitative test as small variations in the freestream velocity prevented accurate, or complete, convergence. The selection of 500 samples of data was based on this test and consideration was given to the time required to sample the data. Long data collection times are a tolerable inconvenience but this length of time also introduces LDV measurement bias errors due to tunnel velocity fluctuations. The time required to take 500 points depended on the seeding and ranged from one to several minutes. In general seeding in the laminar portion of the bubble was poor while other portions of the flowfield allowed quite good seeding. The first measurement location on the surface required the use of low laser power to prevent signal washout from reflections. Locations off the surface allowed higher power settings, approximately 1.5 watts, for better signal to noise ratios.

A frequency shift of 1 MHz was used during all measurements. This shift allowed measurements of reverse flow up to 4.04 m/sec. Bandpass filter settings of 0.3-2 MHz were used very close to the surface inside the laminar regions of the bubble while settings of 0.3-5 MHz were used further from the surface and exclusively in profiles outside the bubble. Particle selection requirements included the following tests. Doppler bursts required 16 cycles, i.e., particles must pass through at least 16 fringes to be considered for velocity measurements. A comparison percent criterion of 10% was used to reduce background noise contributions. This criterion checked the repeatability of the time for each cycle within a burst. An amplitude limit control setting of 0.5 was also used. This prevented measurement of very large particles, particles that may not have accurately followed the fluid flow. Computer software displayed values for mean, RMS, and freestream velocities, Reynolds number, and Reynolds number variation on screen for evaluation after each measurement. Data at this location could then be retaken if some abnormality occurred during sampling. This disturbance could take the form of a large variation in tunnel speed from an atmospheric disturbance. As stated earlier data was collected during calm wind conditions after sunset but occasionally large gusts did occur which influenced the data collection process.

CHAPTER IV

EXPERIMENTAL RESULTS

The goal of this research was to document the laminar separation bubble on the Eppler 387 airfoil. Measurement difficulties and uncertainty at low Reynolds numbers are given special attention due to their significant presence. The data includes static pressure and LDV measurements as well as flow visualization photographs. Experimental data is useful for computational code verification and bubble model development. These codes (examples: Drela, 1987, 1989, and Eppler, 1986) often utilize empirical and semi-empirical models of the laminar separation bubble transition process. In addition, experimental data, especially data that spans several facilities, allows better understanding of the effects of tunnel environment on low Reynolds number airfoil performance.

4.1 Static Pressure Data

The static pressure measurements were made to locate the position of the bubble. This was done to verify certain aspects of the research. The locations of laminar separation, transition, and turbulent reattachment are sensitive to tunnel turbulence intensity as well as airfoil model accuracy and surface finish. Comparison of these results to results obtained at other facilities, namely the data obtained by McGhee (1988) in the LTPT at NASA Langley, lends them a measure of credibility.

The data is presented uncorrected and as such is distorted slightly due to the finite size and constrained nature of the wind tunnel flow field. This data is

20

intended to help document the flow field which contains a laminar separation bubble. Presented as such it is ideal for comparison with previous data, often presented uncorrected, taken at the Notre Dame wind tunnels. In particular it should be compared with data taken on similarly sized models some of which have supporting LDV data. Data at large angles of attack (>10.0°) was not taken because of the large model size and ensuing flow field distortion.

4.1.1 Static Pressure Measurement Error Analysis

The static pressure measurement uncertainty varied with the magnitude of the pressure and thus varied with angle of attack and Reynolds number. The largest uncertainties were present for high α and low Reynolds number. A representative value for the largest uncertainty was $\Delta C_p = 0.1796$ for $R_c = 75,000$ and $\alpha = 8.0°$. In contrast uncertainty could be as low as $\Delta C_p = 0.0072$ for $R_c = 300,000$ and $\alpha = 0.0°$. Uncertainty in C_p varied along the chord with variations in C_p. ΔC_p was largest for low freestream velocity and high airfoil static pressure. Pressure distribution repeatability is shown in Figure 4.1 for four different tests at $R_c = 100,000$ and $\alpha = 2.0°$. Two of thesé tests were specifically made to determine if hysteresis was present. The four plots for the tests group closely, almost within the uncertainty, which is $\Delta C_p = 0.0496$ for this case. The discrepancies are probably the result of uncertainty in angle of attack ($\Delta \alpha = 0.15°$) and variations in Reynolds number (approximately ±2%) during the testing. -

Figure 4.2 shows a comparison of pressure distributions measured at Notre Dame and NASA Langley at $R_c = 100,000$ and $\alpha = 2.0°$. Notice the data sets exhibit the same stagnation points. Also the locations of separation, transition, and reattachment are nearly coincident. These sets of data exhibit an offset or a difference in C_p of about 0.057. If these pressure distributions are

integrated for lift coefficient this offset is irrelevant. Integration of these data sets by the same program results in identical lift coefficients of $C_L = 0.611$. The cause of the offset is unknown. Previous tests (Brendel 1986) have shown the time constant for the tubing used in the pressure measurements to be on the order of 60 msec. A delay of over 16 time constants was used before measurements were recorded so pressure attenuation in the tubing should be small. It also seems unlikely that the offset is a result of a manometer calibration problem as manometer calibration was checked. A discrepancy in angle of attack may explain this offset. A maximum angle error between the airfoils tested in the two wind tunnels would be the sum of the angle of attack uncertainties. An estimated value for this uncertainty is twice the uncertainty for the Notre Dame data. This value would then be $\Delta\alpha = 0.30°$.

Lift curve slopes for identical airfoils tested in different facilities often contain discrepancies. It is possible that the flow environment or model differences could cause such an effect by altering the laminar separation bubble. A higher value of free stream turbulence intensity often acts like an increase in Reynolds number. This would shorten the bubble, altering the pressure distribution. The pressure distribution would likely show a more negative pressure peak. Another explanation may be tunnel wall interference but the expected trend for this would be pressure distribution distortion. A similar situation existed in comparing data from the Notre Dame wind tunnel to data taken in free flight. These pressure distributions from the free flight test showed lower values of C_p across the chord on the upper and lower surface. Lower values of C_p across the chord was the same trend seen between the NASA Langley data and the Notre Dame data. In the pressure distributions lower values of C_p are higher on the graph as negative C_p is plotted on the positive y axis.

4.1.2 Static Pressure Distributions

Figures 4.3-4.36 show the measured pressure distributions for the E387 airfoil. The location of various flow features is discernable in these pressure distributions. The laminar separation bubble alters the pressure distribution on the airfoil in a characteristic manner. The separated laminar shear layer exerts a nearly constant static pressure (separated flow maintains a nearly constant velocity)on the airfoil, creating a pressure plateau. Transition to turbulent flow results in a rapid pressure recovery region shown by a steep slope immediately following the plateau. The static pressure distributions show a laminar separation bubble is the exclusive·transition process observed for Reynolds numbers below 200,000. In some cases this bubble extends over a considerable chord length. At R_c=100,000 and α=2.0° as shown in Figure 4.13 laminar separation occurs at 40% x/c, transition at 76% x/c, and reattachment at 85% x/c. This compared well with locations determined by surface flow visualization. These locations were 40.% x/c and 80.% x/c for separation and reattachment respectively.

An attached transition process, transition without a laminar separation bubble, is observed at R_c=200,000 and R_c=300,000 for moderately high angles of attack. At R_c=200,000 this attached transition process is seen for α=7.0°,8.0°, and 9.0° and is shown in Figures 4.25, 4.26, and 4.27 respectively. At this Reynolds number a separation bubble is again seen at α=10.0°. The shape of this pressure distribution as shown in Figure 4.28 does not show the characteristic shape expected when a bubble is present. This may be the result of poor tap resolution. The taps on the upper surface are spaced every 2% x/c and are optimized to locate large mid-chord bubbles. A small bubble, a few percent chord in length at the leading edge, will not therefore be properly

resolved. The pressure distribution in Figure 4.28 also shows a considerable overshoot in pressure recovery at the end of the bubble. A similar overshoot was seen in static pressure distributions for the Wortmann FX63-137 airfoil (reference) at high angles of attack. In both of these cases the bubble was a short leading edge bubble on an airfoil at high angle of attack, α below but close to that for airfoil stall.

Similar behavior occurs at R_c=300,000 where attached transition is seen for α=7.0° and 8.0° as shown in Figures 4.34 and 4.35 respectively. A small leading edge bubble is seen in Figure 4.36 for the case of R_c=300,000 and α=10.0°. This bubble again shows a very large pressure recovery overshoot at the end of the bubble.

A summation of separation, transition, reattachment, and attached transition is shown in Figures 4.37-4.39 for Reynolds numbers of 100,000, 200,000, and 300,000 respectively. These locations were determined from the pressure distributions shown in Figures 4.8-4.36 and have an uncertainty of ±1% x/c. The locations of attached transition were taken from Eppler's program results (Eppler, 1986). The data for R_c=100,000 is shown in Figure 4.37 . This figure shows the long bubbles that form on the E387 airfoil at moderate angles of attack. As angle of attack increases the bubble moves forward and shortens in length. At an angle of attack of seven to eight degrees the bubble location moves rapidly forward to near the leading edge were a short bubble is formed. This is the same angle for which an attached transition process is seen at higher Reynolds numbers. The population of data points for the higher Reynolds numbers is sparse but the trend of bubble shortening and migration forward can still be seen. The attached transition process is represented by a single symbol for transition. At the higher Reynolds numbers the location of the short leading edge bubble is not shown due to the poor position resolution

caused by tap spacing.

4.1.3 Lift and Moment Curves

The measured pressure distributions were integrated for lift and quarter chord moment. The resulting coefficients do not have standard tunnel corrections applied. The worst case uncertainty in lift and moment coefficient was approximately twice the average uncertainty in pressure coefficient for a particular test case. This results in a representative uncertainty in lift coefficient, ΔC_L, of 0.1 for $R_c=100,000$ and $\alpha=2.0°$. The uncertainty in lift coefficient dropped to approximately $\Delta C_L=0.02$ for $R_c=200,000$. The uncertainty in moment coefficient may be assumed to on the same order as that for the lift coefficient. Uncertainty in pressure tap location was not known. This value could be assumed to be on the order of the tap hole diameter, which was .79 mm, for the chord wise coordinate, but was unknown for the other coordinate. Figure 4.40 shows the lift and moment curve slopes for the E387 airfoil at a Reynolds number of 100,000. The two sets of data come from Notre Dame and NASA Langley. The lift curves match well. The start of nonlinearity in the lift curve slope at high angle of attack is pronounced and both data sets agree in this respect. The linear portion of the curves seem to differ in slope with the lift curve slope of the Notre Dame data being the greater of the two. Lack of tunnel corrections could possibly account for this. The moment curves compare poorly but the same trend toward reduced negative pitching moment at high angles of attack is shown by both data sets. Figure 4.41 shows lift and moment versus angle of attack curves for the E387 at $R_c=75,000$. Figures 4.42-4.44 shows lift and moment curves for the E387 airfoil at Reynolds numbers of 100,000, 200,000, and 300,000 respectively. All of the lift and moment curves show the same trends with similar lift curve slope, lift curve slope round-off, and pitching

moment curve shapes. The data set for $R_c=75,000$ is incomplete but the higher Reynolds number cases do not show pre-stall hysteresis as might be expected for a long mid-chord laminar separation bubble.

4.2 Laser Doppler Velocimetry Boundary Layer Measurements

Boundary layer measurements by LDV are attractive in flow fields with reverse flow like that inside laminar separation bubbles. These measurements were made on the E387 airfoil at $R_c=100,000$ and $\alpha=2.0°$. LDV data will also be presented for a NACA 66_3-018 airfoil at $R_c=160,000$ and $\alpha=12.0°$.

4.2.1 E387 LDV Boundary Layer Measurements

The LDV data for $R_c=100,000$ and $\alpha=2.0°$ is plotted in dimensionless U/U_{ext} velocity plots. In these plots the vertical distance, y (mm), is normal to the airfoil's surface. The chord position is set manually and uncertainty in chord position is estimated to be about 1 mm or 0.33% x/c. This uncertainty arises from a combination of possible errors that include scribed airfoil chord locations and initial probe volume location.

Figures 4.45-4.47 show laminar boundary layers upstream of the laminar separation bubble. The pressure gradient on the E387 at these conditions is favorable up to 25% x/c and adverse after this chord station. The boundary layers in Figure 4.47 are for 38% x/c and 39% x/c and show the effects of an adverse pressure gradient with thicker boundary layers. The 39% x/c profile in Figure 4.47 b) shows near separation like behavior with an inflection point and small velocity gradient dU/dy at the surface. Figure 4.48 a) shows the velocity profile at 40% x/c to be the first separated velocity profile. This profile also exhibits reverse flow. The separation point is now determined by LDV data to occur at 39.5% ± 0.8% x/c.

A distinct region of the bubble is located from separation to 55% x/c. In this laminar region a distinct recirculation zone is seen. Figures 4.48-4.51 show these profiles. If the pressure distribution in Figure 4.13 for R_c=100,000 and α=2.0° is examined the region from separation to 55% x/c shows a slight pressure recovery with a small adverse pressure gradient. The LDV measurements in this region were made with relatively good seeding and are presented with relatively good confidence (i.e., accurate to with ±15%).

The velocity profiles downstream of this recirculation region show very little reverse flow as can be seen in Figures 4.52-4.54 for chord stations of 56% to 66% x/c. As previously mentioned the seeding for LDV measurements in this region was poor. The pressure distribution over this region shows a pressure gradient that is very nearly zero. This plateau of zero pressure gradient roughly extends from 54% x/c to 76% x/c. Flow visualization photographs like those in Figures 4.76-4.79 show a possible Tollmein-Schlichting disturbance that is first noticed around 66% x/c.

The pressure distribution in Figure 4.13 suggests transition to turbulent flow in the shear layer at 76% x/c. This is the beginning of the rapid pressure recovery region of a turbulent boundary layer. The velocity profiles from 68% x/c to 74% x/c show odd shapes as seen in Figures 4.55-4.56 . This may be a result of improper bandpass filtering in the LDV measuring process or a velocity bias. A velocity due to fluctuating flow would be towards higher velocities. Considering the possibility of improper filtering and poor seeding these profiles may yet show a possible boundary layer profile. The flow in this region may contain circulation. The net flow through this aft region of the bubble may be nearly zero, yet instantaneous streamwise and reverse flow with a recirculation pattern may be present periodically. The boundary layer measurements are a long term average of this behavior so actual average measurements of reverse

flow may be unlikely. Vorticity seems to be shed from the shear layer during transition, a point located above the airfoil surface. This corresponds with the shape of the profiles which suggest a core location about 3.5 mm above the surface at 70% x/c and about 6 mm at 74% x/c. This vorticity is rapidly dissipated and is not seen at 76% x/c.

The shear layer grows rapidly after transition and the boundary layer profile at 76% x/c shown in Figure 4.57 a) shows this. The profile exhibits reverse flow but the boundary layer thickness is very low, just over 2mm. This can be compared to the boundary layer thickness at 68% x/c which is over 6.5mm. The profiles at 78% x/c and 80% x/c shown in Figure 4.57 b) and 4.58 a) show nearly attached boundary layers. The profile at 81% x/c in Figure 4.58 b) is the first measured attached boundary layer after the bubble. LDV measurements suggest the reattachment location to be 80.5% ±.8% x/c. Figure 4.59 shows turbulent boundary layers at 90% x/c and 95% x/c.

The boundary layer velocity profiles have been integrated for displacement, momentum, and energy thickness. These values are plotted in Figure 4.60 . The integrated thicknesses show considerable scatter. This scatter was not unexpected as the uncertainty in the integrated values was large. Uncertainty in displacement thickness is about 0.1 mm. This value was on the order of the initial probe height position uncertainty. Uncertainty in momentum and energy thicknesses were about 0.3mm and 0.4 mm respectively. This was a result of the shapes of the profiles and the nature of the integration; where unity minus nondimensional velocity, nondimensional velocity, and products of these are integrated.

The rapid growth in displacement thickness marks the location of separation. The displacement thickness reaches a peak at 66% x/c. This peak is sometimes used as a marker for transition. In this case it is a marker for the

start of the transition process. Momentum and energy thicknesses show a rapid growth at the start of transition and peak at the end of the transition process at 76% x/c.

Shape factors can be obtained from the integrated thicknesses. The uncertainty in shape factors is larger that that for the integrated thicknesses . In the LDV tests on the E387 the uncertainty for H_{12} is on the order of 1.2 mm. Figure 4.61 is a graph of shape factor H_{12} versus x/c. This figure shows a gradual reduction in H_{12} in the favorable pressure gradient laminar boundary layer and an increase near separation. The laminar portion of the separation bubble, from 40% x/c to 64% x/c, shows large values of H_{12}. The remaining part of the bubble and the turbulent boundary layers aft of the bubble show low values for the shape factor H_{12}.

The shape factor H_{32} is a ratio of energy to momentum thickness. This shape factor can be used to determine the point of separation in semi-empirical boundary layer equations (Eppler, 1980, 1986). This value of H_{32} is 1.51509 for the separation profile. This value is not seen near separation but Figure 4.62 shows a general decline in H_{32} up to separation. The value of H_{32} at 39% x/c is 1.592. The magnitude of the shape factor in the bubble is widely varying. The curve of H_{32} versus x/c is only relatively smooth for chord stations outside of the bubble. The uncertainty in H_{32} is approximately 4 mm for this data in the bubble region.

4.2.2 LDV Measurement Uncertainty and Repeatability

Uncertainty in LDV measurements by direct calculation for the system used would be complex. Such things as uncertainty in focal length and aberration for optics and uncertainty in laser light frequency or coherency would be hard to quantify. Other factors like uncertainty in shifting frequency and

calibration of frequency shifting were not investigated. The LDV system should be accurate and repeatable, if properly adjusted, for measurements with good seeding in steady flows. Meyers (1979) listed LDV hardware uncertainty to be on the order of two and one half percent.

The quality of LDV measurements can be degraded by several measurement situations. Those pertinent to this experiment will be described. Low data density and its associated discontinuous signal, often found with poor or intermittent seeding, can result in velocity measurement errors. Fringe bias results when particles pass through the measuring volume fringes in a non-normal direction. This would be the case for boundary layer measurements in a laminar separation bubble. A bubble often contains recirculation regions and measurements with at fringe velocity vector angle up to 90° would seem probable. The probability of making a measurement decreases 10% when the velocity vector and the fringe normal differ in angle by 37°. Fringe bias is reduced by frequency shifting and high cycles per burst criterion, both of which were used in the measurements presented in this thesis. Another bias is a velocity bias associated with fluctuating flows. In an unsteady flow a high flow velocity measurement is more probable than a low one as high velocities carry a greater number of particles through the probe volume. This results in an erroneous average velocity measurement. In a LDV experiment conducted by Bogard (1979) on the viscous sublayer of a fully developed turbulent boundary layer in a channel, velocity bias errors of 10% were found. This was the difference between weighted and unweighted average velocity measurements. In Bogard's experiment LDV measurements were made with natural seeding in a water tunnel. Turbulence in the boundary layer was solely responsible for the bias. Velocity bias also can be attributed to multiple measurements on a single particle. Even the finite size of the probe volume contributes to velocity errors in

a flow region with a velocity gradient. Meyers (1979) listed maximum errors in measured turbulence intensity up to 0.5% due to probe volume size alone.

Previous investigators (Fitzgerald, 1988 and Brendel, 1987) have compared low Reynolds number LDV boundary layer measurements to hot-wire measurements. Comparison is very good for nondimensional tangential velocity in the outer regions of the boundary layer and above. Fitzgerald listed the accuracy of velocity measurements as ±0.15 m/sec for the hot-wire and <10% for the LDV measurements. Fitzgerald also noted that U_e varied greatly from chord station to chord station. These uncertainty values seem overly optimistic.

The largest factor in LDV velocity measurement for this experiment was proper resolution of an average velocity in an unsteady flow with poor seeding. The type of flow inside a laminar separation bubble. Proper weighting factors for individual velocity measurements are needed to eliminate velocity biases. The proper bandpass filtering is easy to determine in attached laminar and turbulent boundary layers by observation of the doppler bursts in the photomultiplier signal. The proper filtering is more difficult inside the bubble due to nonuniform seeding of the flow with smoke particles. The initial laminar region of the bubble described earlier was unexpectedly easy to measure. The following region was more difficult, with very sparse seeding, but what seemed to be the best filtering was used. In this region average velocities near zero were often composed of individual velocities that ranged from -2 m/sec to 2 m/sec. The profiles in the turbulent aft region of the bubble usually provide good quasi-steady seeding. These profiles were measured and looked quite strange with a pronounced "s" shape. These profiles were remeasured with different bandpass settings and seemed to show a region that was forced to low velocity by the filtering process. The original measurements were thus retained.

Another source of error includes wind tunnel free stream variations. Considering all factors a value for uncertainty in LDV measurements is estimated to be $\Delta U/U_{ext} = .15$ inside the laminar separation bubble's boundary layer and $\pm 15\%$ above and outside the bubble. Because the average velocity inside the bubble, measurements below the displacement thickness, can vary from approximately -20% to 80% of U_{ext}, the estimated uncertainty can range from 20% to 75%. Confidence in measurements is increased if they are repeatable in the long term. Figure 4.63 shows two such repeatability tests. These profiles show worst case repeatability for profiles were filtering and seeding was considered good. Both of these profile comparisons contain local areas were velocity measurements differed considerably. In general velocity profile measurements were repeatable to a difference less than 5%.

4.2.3 NACA 66$_3$-018 Airfoil LDV Measurements

LDV boundary layer measurements were made on the NACA 66$_3$-018 airfoil at R_c=160,000 and α=12.0°. This airfoil supports a short leading edge bubble at these conditions. The LDV system used is exactly the same as used for the E387 tests. The only equipment differences are found in model size and mounting. The model was mounted between plexiglass endplates in a similar fashion to the E387 pressure model and had a chord of 249.5 mm. Figure 4.64 shows the pressure distribution for this airfoil at these conditions. This pressure distribution suggests laminar separation at 3% x/c, transition at 6% x/c, and reattachment at 12% x/c, with uncertainties of one half the tap spacing or 0.5% x/c. The measured U/U_{ext} velocity profiles for the NACA 66$_3$-018 airfoil are shown in Figures 4.65-4.71. Laminar boundary layer profiles are found at 1% x/c and 2% x/c. The bubble profiles in Figures 4.66-4.68 a) show a single recirculation zone. The reverse flow region grows in thickness in the laminar

portion of the bubble as seen for the 4% x/c and 5% x/c chord locations in Figure 4.66 . The 6% x/c chord station in Figure 4.67 a) shows an increase in reverse flow magnitude with a thickness similar to that seen at 5% x/c. At 7% x/c, Figure 4.67 b), the reverse flow magnitude is similar but the thickness of the reverse flow region is decreasing. This profile also shows a smaller velocity gradient across the shear layer, the region between reverse flow and the streamwise flow. At 8% x/c the profile shows less reverse flow and an even lower velocity gradient across the shear layer as shown in Figure 4.68 a). Figure 4.68 b) for 10% x/c shows an attached boundary layer. This suggests a location for reattachment at 9. % x/c ±0.8% x/c. Figures 4.69-4.71 show turbulent boundary layers for chord stations from 15% x/c to 55% x/c. Note the y scale change in Figure 4.71 b).

These NACA 66_3-018 airfoil boundary layer profiles have been integrated for displacement, momentum, and energy thicknesses. Figure 4.72 shows these quantities plotted as a function of x/c. In this figure the rapid growth of δ_1 marks the location of laminar separation. This location is between 2% x/c and 4% x/c. The displacement thickness maximum occurs at 6% x/c. The momentum and energy thicknesses also begin a rapid growth at 6% x/c, oddly from negative values. This compares exactly to a location of 6. % x/c for transition obtained from the pressure distribution. The rapid growth in δ_2 and δ_3 ends at the 10% x/c chord position. Figure 4.73 show the shape factor H_{12} plotted as a function of chord position. The small magnitude negative values for momentum thickness in the laminar portion of the bubble result in large magnitude negative values for H_{12} in this region. The uncertainty in this shape factor is on the order of 40 or ±160% inside the bubble. However, positive values of momentum thickness are within these values uncertainties (±0.2mm). If this were the case the shape of the shape factor plot could look entirely

different with no large magnitude negative values. After transition at 7% x/c the shape factor assumes large positive values which rapidly fall in magnitude until reattachment. This figure does show classical behavior in the fact that the magnitude of H_{12} reaches a peak at transition. Figure 4.74 shows the shape factor H_{32} plotted versus chord position. This shape factor distribution shows a possible value, plus or minus the uncertainty which is 1.2 mm, equal to that for a theoretical separation boundary layer profile, on a flat plate with pressure gradient, of $H_{32} = 1.51509$. Separation for the NACA 66_3-018 airfoil at these conditions is 3% x/c as determined by the pressure distribution in Figure 4.64 . The magnitude of H_{32}, which is a ratio of energy thickness to momentum thickness, begins a rapid growth at transition at 6% x/c. This behavior is expected, as at transition, the energy content of the separated shear layer grows rapidly. The momentum thickness initially takes longer to grow but does so rapidly in the turbulent shear layer. This behavior is seen in Figure 4.72 where the difference between the energy thickness at 5% x/c and 6% x/c is distinct but that between the momentum thickness at these chord locations is almost zero.

4.3 Flow Visualization

Flow visualization photographs are an important supplement to the LDV and static pressure distribution measurements. The major limitation to the interpretation of this type of flow visualization is the fact that streamlines are not shown. Rather, typical flow visualization pictures identify streaklines. The flow field in and around the laminar separation bubble is unsteady and streaklines in unsteady flow can be deceptive. Hamma (1962) provides further insight into this phenomena.

The laminar separation bubble on the E387 airfoil covers a substantial

portion of the chord. This can be seen in Figure 4.75 where the streaklines and airfoil cross section are shown in the same true scale. The triangles mark the chord locations of laminar separation at 39.5% x/c, start of transition at 65.0% x/c, end of transition at 76.0% x/c, and reattachment at 80.5% x/c. Figure 4.76 and Figure 4.77 show similar photographs in an enlarged format. Notice the straight and sharply defined boundary between the streaklines and the outer flow in the laminar portion of the bubble. The considerable distance that transition occupies is also visible. The crest like structures visible are most likely two dimensional wave disturbances that are being amplified. The true shape of the streamlines in this transition region of the shear layer may look like sine waves bounded by an exponential envelope. The other obvious structures visible are the periodic smoke puffs. These are most likely caused by vorticity shed from the bubble.

During LDV measurements the flow field was seeded by smoke. A smoke tube was positioned to impinge on the airfoil at its stagnation point. The bubble, or more probably the laminar portion of the bubble, was often visible as a region of scarce smoke surrounded by dense smoke. Smoke would enter this region of the flow in bursts from the turbulent aft portion. During measurements the position of this region was mapped by visually identifying the edge of the smoke with the LDV probe volume. This region defines a dividing streakline of sorts. Brendel (1986) found the dividing streamline to coincide with the line of smoke that lies between the bubble and external flows. Althaus (1986) states similar results and also presents photographs. A dividing streamline in a laminar separation bubble is a streamline in the boundary layer across which the net mass flow is zero. Figure 4.79 shows this dividing streakline on a cross section of the E387. This dividing streakline correlates very well with flow visualization photographs and measured boundary layer velocity profiles. A

particularly interesting feature of this dividing streakline is the chord location of its aft most point at 76% x/c. This is the chord position of transition in the shear layer.

4.4 Laminar Separation Bubble Parameters

The characterization of laminar separation bubbles can be done by the examination of certain parameters. Table 4.1 shows a compilation of data for four different bubbles. These bubbles are present on the E387, Wortmann FX63-137, and NACA 66_3-018. This table is primarily composed of information calculated from LDV measurements. The hot-wire data for the Wortmann airfoil is included as it is for a similar angle of attack as the E387 data and at the same Reynolds number of 100,000.

The bubble aspect ratio, AR_b , term was calculated to show the large differences in bubble geometry that exist. The E387 has a very long thin bubble with AR_b=33.0 . In contrast to this was the bubble on the NACA 66_3-018 which has an aspect ratio of only 3.2 for the higher Reynolds number case. The success of a search for a universal bubble modeling criterion seems unlikely with this type of geometry range. Boundary layer profiles shown in Figures 4.45-4.58 for the E387 and Figures 4.65-4.71 for the NACA 66_3-018 show quite different flow fields for these two extremes in bubble geometry.

One important trend was seen for all of the airfoils. This is the relationship between the transition Reynolds number, R_{l_t} , and the Reynolds number based on momentum thickness at separation, $R_{\delta_{2s}}$. Large values for $R_{\delta_{2s}}$ represent separated shear layers that are in close proximity to the airfoil's surface. This close proximity has a stabilizing effect on the transition process, hence a larger value for R_{l_t} is expected. This trend is seen in Table 4.1 but no correlation is attempted due to the small number of data points.

In summary this experiment was very time intensive and somewhat difficult. Low flow velocities and unsteady phenomena were the major contributors to this difficulty. The major concern of this author in regards to the results is the necessity of proper bandpass filtering of the LDV photodetector output. Intermittent seeding created and compounded the filtering problem. In effect these difficulties required that you know the answer to a problem before you investigate it.

CHAPTER V

CONCLUSIONS AND RECOMMENDATIONS

The objective of this study was to measure the flow field in and around the laminar separation bubble on an E387 airfoil at low Reynolds numbers. The measurements were made using LDV at $R_c = 100,000$ and $\alpha = 2.0°$. Supporting static pressure measurements and flow visualization were also done. Static pressure measurements for the E387 airfoil at angles of attack from negative two to ten degrees at Reynolds numbers from 75,000 to 300,000 were made to locate the laminar separation bubble and were integrated for lift and moment curves. LDV measurements were also made on a NACA 66_3-018 airfoil at $R_c = 160,000$ and $\alpha = 12.0°$. A quote by McMasters (1979) may be appropriate at this point. "The wind tunnel is a marvelous tool for describing what happens, but seldom provides much guidance on why a particular event occurs."

5.1 Conclusions

The Eppler 387 exhibits a large laminar separation bubble at a mid-chord location for low angles of attack. At $R_c = 100,000$ and $\alpha = 2.0°$ this bubble extends from 39.5% ± .8% x/c to 81.5% ± .8% x/c as determined by LDV measurements. At these conditions the location of transition in the shear layer is at 76% ± .8% x/c as determined by the peak in displacement thickness calculated from LDV measurements.

A compilation of data obtained by the LDV method at low Reynolds numbers on airfoils with laminar separation bubbles is tabulated in Table 4.1 . Examination of this data reveals a few trends.

38

The transition Reynolds number of the separated shear layer increases with increasing Reynolds number based on momentum thickness at separation. Brendel reached a similar conclusion and the new cases shown in Table 4.1 support this. This suggests that the transition Reynolds number parameter is not a constant as some investigators have suggested. The Reynolds number based on momentum thickness at separation provides a measure of the stabilizing effects that the airfoil's surface has on the separated shear layer.

Previous investigators (Fitzgerald 1988) found discrepancies in trends for integrated parameters between hot-wire and LDV data for the NACA 66_3-018 airfoil at R_c=140,000 and α=12.0°. New measurements on the NACA 66_3-018 airfoil at R_c=160,000 and α=12.0° show a local minimum in H_{32} at transition. This compares favorably with Fitzgerald transformed hot-wire data trends. Transformed hot-wire data is data that has been corrected for flow direction and it typically exhibited larger magnitude reverse flows than Fitzgerald's LDV data. Fitzgerald's LDV data shows a local minimum in H_{32} at transition. The transformed hot-wire data shows a local peak in H_{32} just after transition. Physically this indicates the energy dissipation to momentum loss ratio is large just after transition. The E387 measurements showed no discernable trend in H_{32} in the bubble but energy dissipation thickness did reach a peak at transition. The bubble examples in Table 4.1 all show a general increase in H_{12} in the bubble region except for the NACA 66_3-018 airfoil at R_c=160,000.

Figure 5.1 shows a proposed flowfield for the E387 at R_c=100,000 and α=2.0° in the vicinity of the laminar separation bubble. This model shows a recirculation zone in the early laminar portion of the bubble. The central zone of the bubble is a laminar dead air region. This region may exhibit small streamwise and reverse flow oscillations that are not shown in the average velocity boundary layer profiles. The final region shown is the turbulent aft

portion. Horstmann (1981), van Ingen (1985), and McGhee have presented presumed bubble models that show three flow regions inside the bubble. These models were created to explain surface flow phenomena that was present on the airfoil surface inside the bubble. The periodic shedding of vorticity seems to come from a point in the shear layer were disturbances are first noticeably amplified. Flow visualization photographs confirm the periodic shedding process.

5.2 Recommendations

This study of low Reynolds number laminar separation bubbles, as in most studies, will probably raise more questions than it answers. The following are a few recommendations for further research.

1. Improvements in the test facility and test equipment:

Improved resistance to the influence of wind gusts is needed. Incorporation of gust filters for the wind tunnel motor shed will expand the envelope of conditions in which low speed tests can be run.

An improved bandpass filter with an expanded selection of frequencies is needed.

LDV measurements in the laminar separation bubble need an improved seeding arrangement.

An automated LDV traversing system would speed data acquisition.

Simultaneous high frequency static pressure measurements may allow resolution of unsteady bubble flow characteristics.

2. Expansion of the low Reynolds number data base:

More boundary layer measurements should be made with LDV and hot-

wire techniques. Were applicable the hot-wire technique should be used to save time.

LDV measurements should be made on the E387 at R_c=200,000 and angle of attack α=1.0°. At this Reynolds number and angle of attack the laminar separation bubble still covers over 30% of the chord. Previous LDV experience with the NACA 66_3-018 airfoil at a Reynolds number of 100,000 indicated that velocities in this flow regime was nearly impossible to measure.

It would be interesting to measure boundary layers on low Reynolds number airfoils with flow control devices. Pneumatic turbulators are one such device that seems particularly promising. Horstmann (1981), Boermans (1989), and van Ingen (1985) have shown flow control devices, namely fixed boundary layer trip strips and pneumatic turbulators, can reduce drag. Pfenninger (1988) has suggested flow control over substantial portions of the upper surface may improve low Reynolds number airfoil performance by reducing the large pressure drag associated with a laminar separation bubble.

TABLES

TABLE 2.1

EPPLER 387 AIRFOIL COORDINATES

Upper Surface		Lower Surface	
x/c	y/c	x/c	y/c
0.00000	0.00000	0.00000	0.00000
0.00044	0.00234	0.00091	-0.00286
0.00519	0.00931	0.00717	-0.00682
0.01423	0.01726	0.08190	-0.01017
0.02748	0.02562	0.03596	-0.01265
0.04493	0.03408	0.05827	-0.01425
0.06643	0.04238	0.08569	-0.01500
0.09185	0.05033	0.11800	-0.01502
0.12094	0.05775	0.15490	-0.01441
0.15345	0.06448	0.19599	-0.01329
0.18906	0.07037	0.24083	-0.01177
0.22742	0.07529	0.28892	-0.00998
0.26813	0.07908	0.33968	-0.00804
0.31078	0.08156	0.39252	-0.00605
0.35505	0.08247	0.44679	-0.00410
0.40077	0.08173	0.50182	-0.00228
0.44767	0.07936	0.55694	-0.00065
0.49549	0.07546	0.61147	0.00074
0.54394	0.07020	0.66472	0.00186
0.59272	0.06390	0.71602	0.00268
0.64136	0.05696	0.76475	0.00320
0.68922	0.04975	0.81027	0.00342
0.73567	0.04249	0.85202	0.00337
0.78007	0.03540	0.88944	0.00307
0.82183	0.02866	0.92205	0.00258
0.86035	0.02242	0.94942	0.00196
0.89510	0.01679	0.97118	0.00132
0.92554	0.01184	0.98705	0.00071
0.95128	0.00763	0.99674	0.00021
0.97198	0.00423	1.00000	0.00000
0.98729	0.00180		
0.99677	0.00043		
1.00000	0.00000		

42

TABLE 2.2

EPPLER 387 PRESSURE TAP COORDINATES

Upper Surface		Lower Surface	
x/c	y/c	x/c	y/c
0.00	0.0000	0.00	0.00
0.02	0.0209	0.02	-0.0103
0.04	0.0317	0.04	-0.0129
0.06	0.0399	0.06	-0.0143
0.08	0.0466	0.08	-0.0148
0.10	0.0524	0.10	-0.0150
0.12	0.0575	0.15	-0.0145
0.14	0.0617	0.20	-0.0132
0.16	0.0656	0.25	-0.0114
0.18	0.0689	0.35	-0.0077
0.22	0.0743	0.40	-0.0058
0.24	0.0765	0.45	-0.0040
0.26	0.0783	0.50	-0.0023
0.28	0.0798	0.55	-0.0009
0.30	0.0807	0.60	-0.0005
0.32	0.0817	0.65	0.0016
0.34	0.0822	0.70	0.0024
0.36	0.0824	0.75	0.0030
0.38	0.0821	0.80	0.0034
0.40	0.0817	0.85	0.0034
0.42	0.0808	0.90	0.0029
0.44	0.0797	0.95	0.0020
0.46	0.0784		
0.48	0.0767		
0.50	0.0750		
0.52	0.0728		
0.54	0.0706		
0.56	0.0681		
0.58	0.0655		
0.60	0.0629		
0.62	0.0600		
0.64	0.0572		
0.66	0.0542		
0.68	0.0511		
0.70	0.0481		
0.72	0.0449		
0.74	0.0418		
0.76	0.0386		
0.78	0.0354		
0.80	0.0322		
0.85	0.0241		
0.90	0.0150		
0.95	0.0078		

TABLE 4.1

SEPARATION BUBBLE PARAMETERS

From LDV Data Except as Indicated

Airfoil	E387	FX63-137 (hot-wire)	FX63-137	FX63-137 (lower surface)	NACA 66$_3$-018	NACA 66$_3$-018
angle of attack	2.0°	3.0°	7.0°	-5.0°	12.0°	12.0°
R_c (x 10^{-5})	1.0	1.0	1.0	1.0	1.4	1.6
S (%chord)	39.5	42	33	2	1.2	3.0
T (% chord)	76	69	53	10	7.0	6.0
R (% chord)	80.5	80	59	†	12	9.0
chord (mm)	304.8	305	305	305	249.5	249.5
l_1 (mm)	111.3	83	61	25	2.48	1.94
AR_b	33.0	15.4	20.3	9.6	5.8	3.2
γ	2.6°	3.7°	2.8°	7.0°	9.6°	16.3°
Rl_1 (x10^{-3})	32.5	41	31	12	16.1	9.4
$R_{\delta_{1s}}$	670	609	597	191	654	488
$R_{\delta_{2s}}$	160.6	194	180	57	100.7	75
$R_{\delta_{1t}}$	1990	3084	2136	1422	3408	3375
$R_{\delta_{2t}}$	119	503	345	71	271	125
δ_{1s} (mm)	1.65	1.2	1.2	0.4	0.589	0.39
δ_{1t} (mm)	2.41	6.6	4.2	3.0	3.07	2.7
δ_{2s} (mm)	0.404	0.40	0.36	0.12	0.09	0.06
δ_{2t} (mm)	1.26	1.07	0.68	0.15	0.244	-0.10
H_{12s}	4.07	3.15	3.33	3.33	6.72	2.6
H_{12t}	1.91	6.13	6.21	20	12.51	-25.9
H_{32s}	1.63	1.54	1.56	1.5	1.43	1.5
H_{32t}	1.74	1.37	1.49	1.82	1.74	-0.41
U_∞ (m/sec)	5.3	†	†	†	9.9	10.3
U_{e_s} (m/sec)	6.4	†	†	†	17.8	20.0

† indicates no table entry
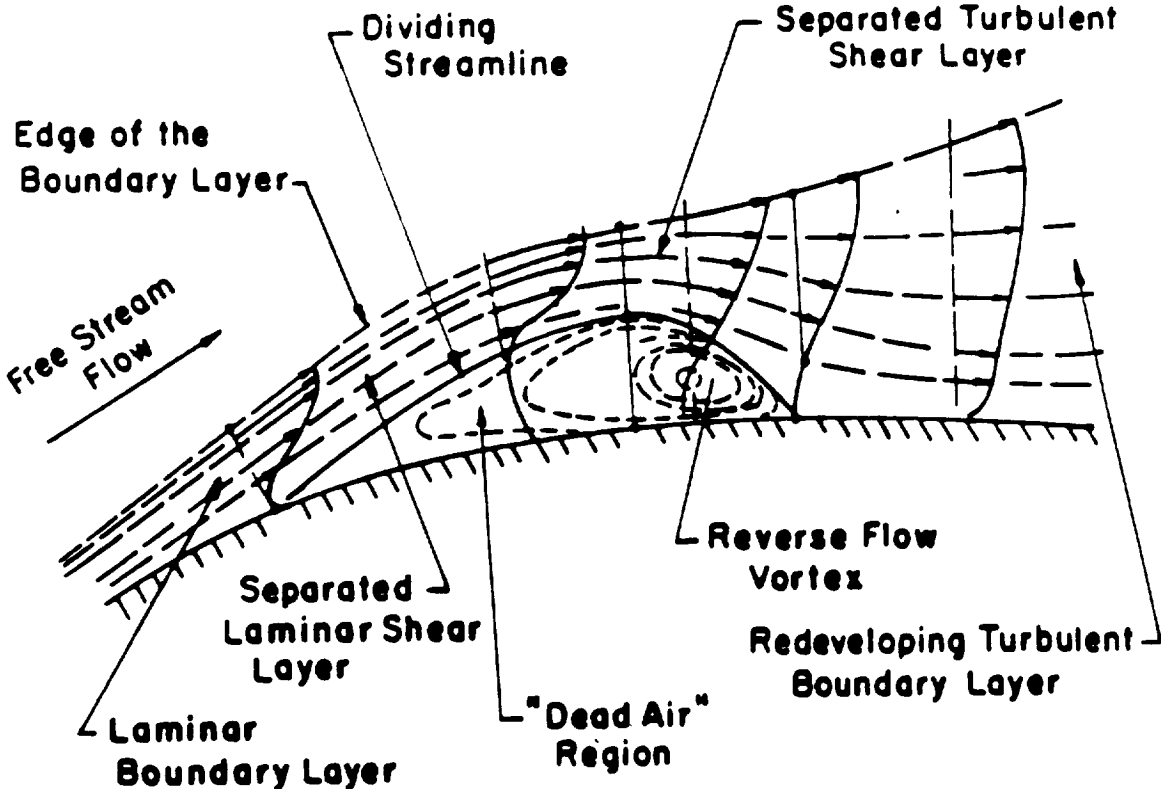
Figure 1.1   The Flowfield in the Vicinity of a Laminar Separation Bubble (Horton, 1968)
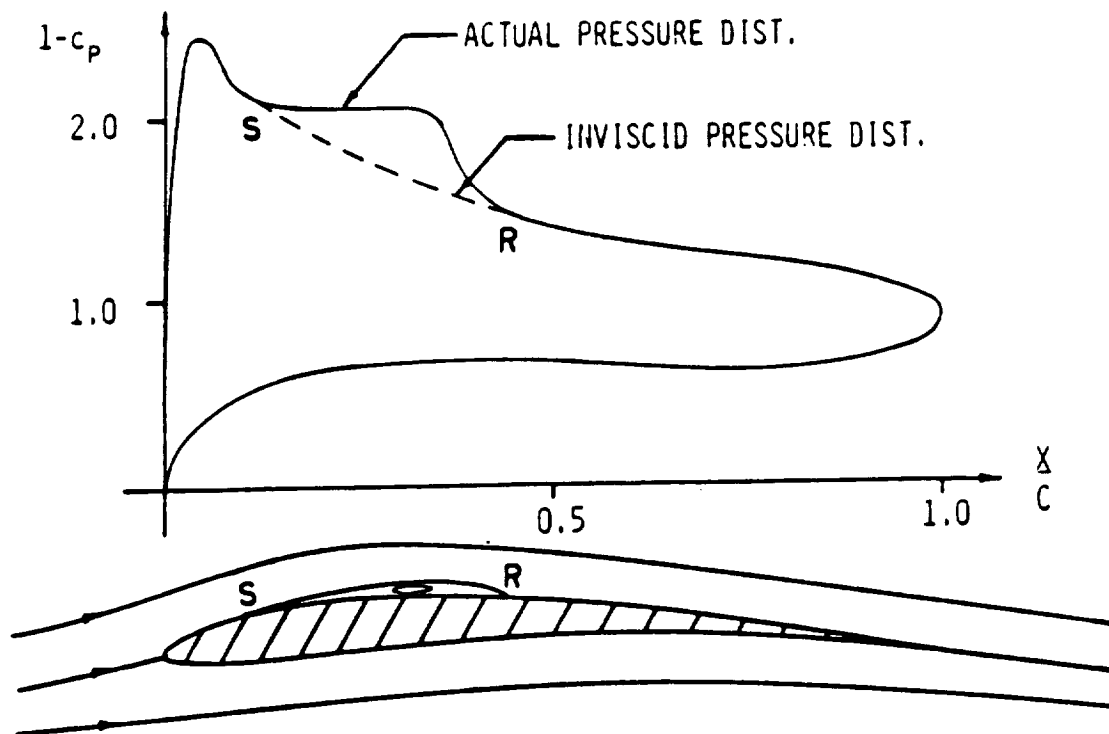
Figure 1.2   Characteristic Pressure Distribution on an Airfoil with a Laminar Separation Bubble of the "Short" Type (Russell,1979)
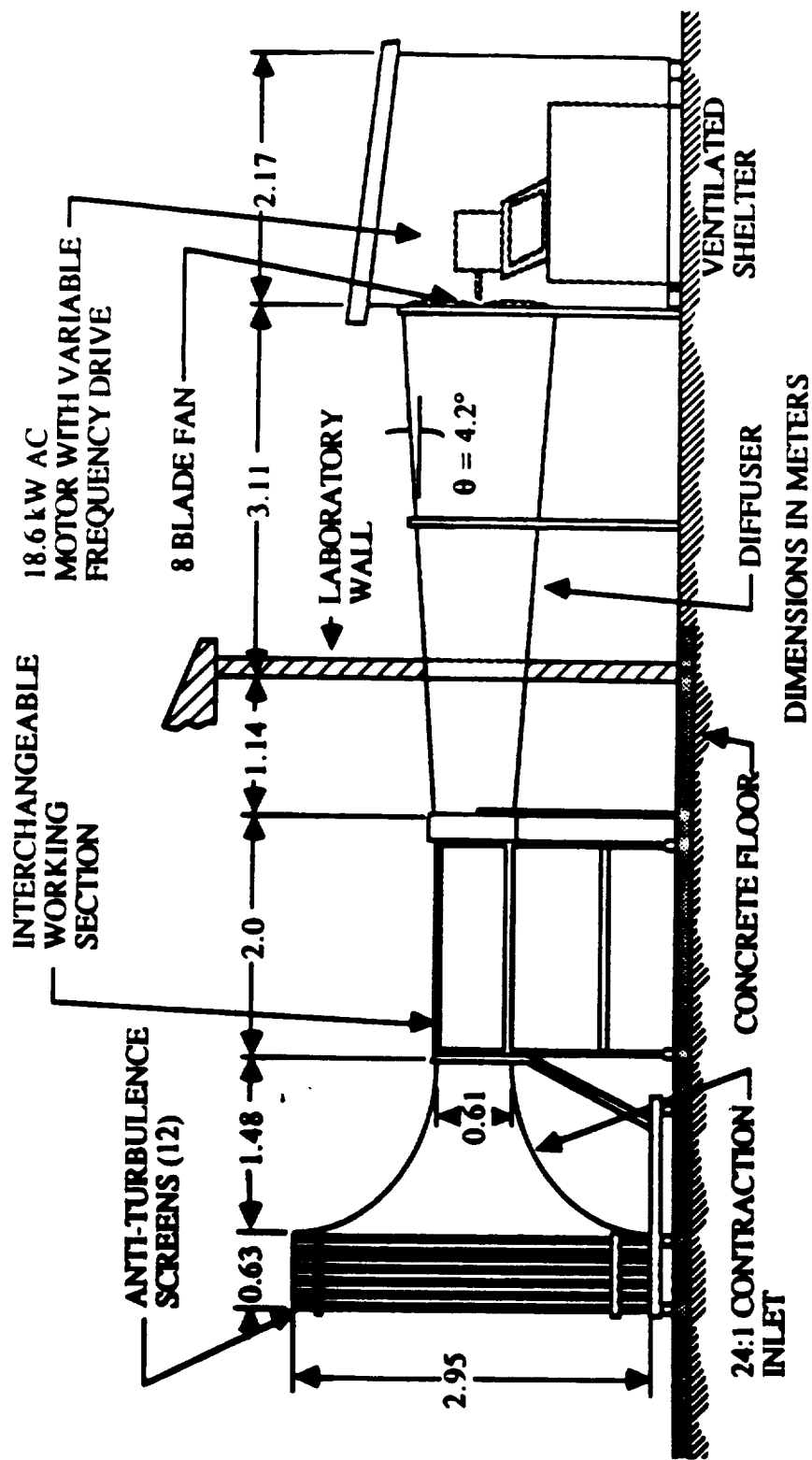
Figure 2.1   Notre Dame Aerospace Laboratory Low Speed Wind Tunnel
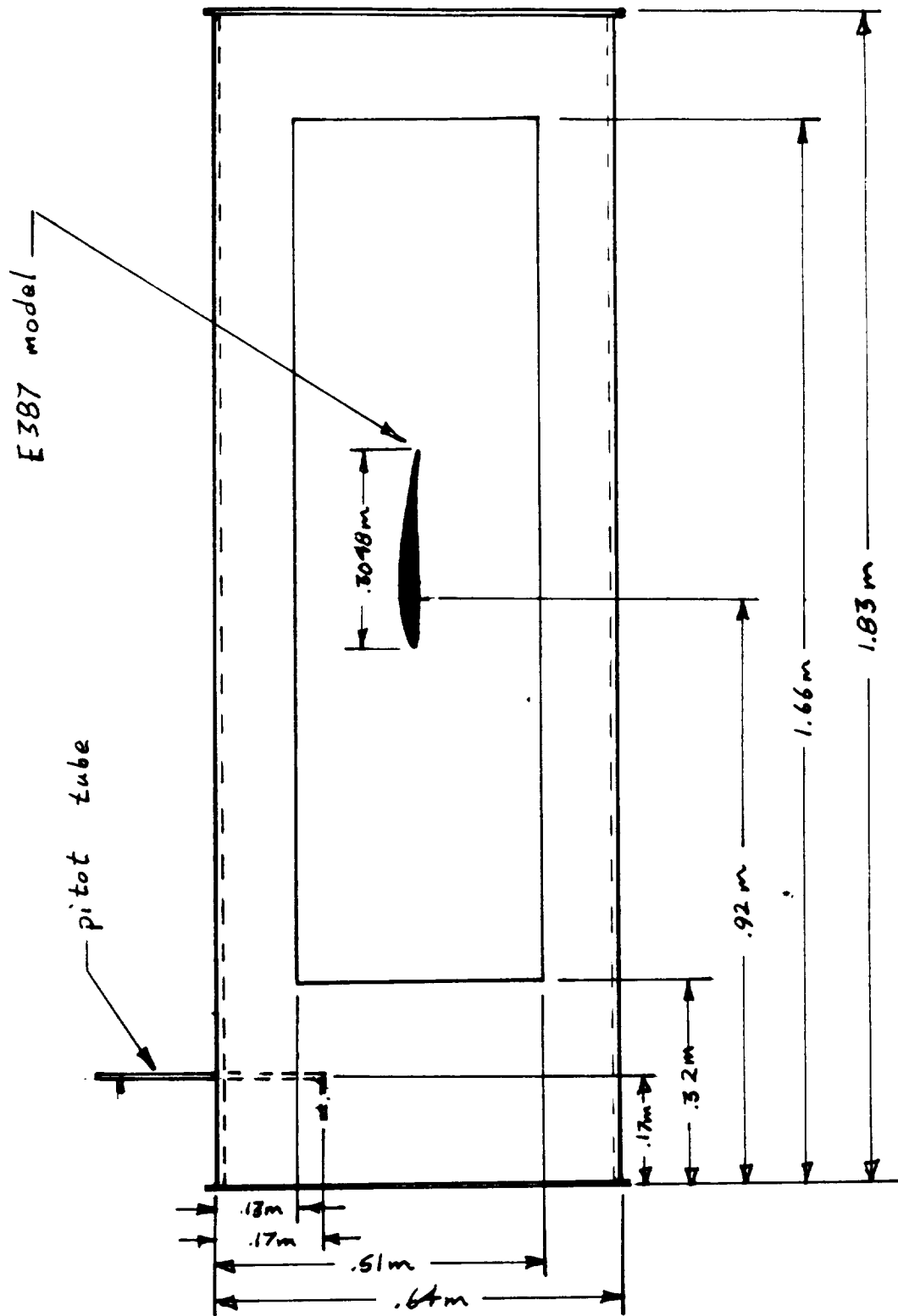
Figure 2.2   Wind Tunnel Test Section
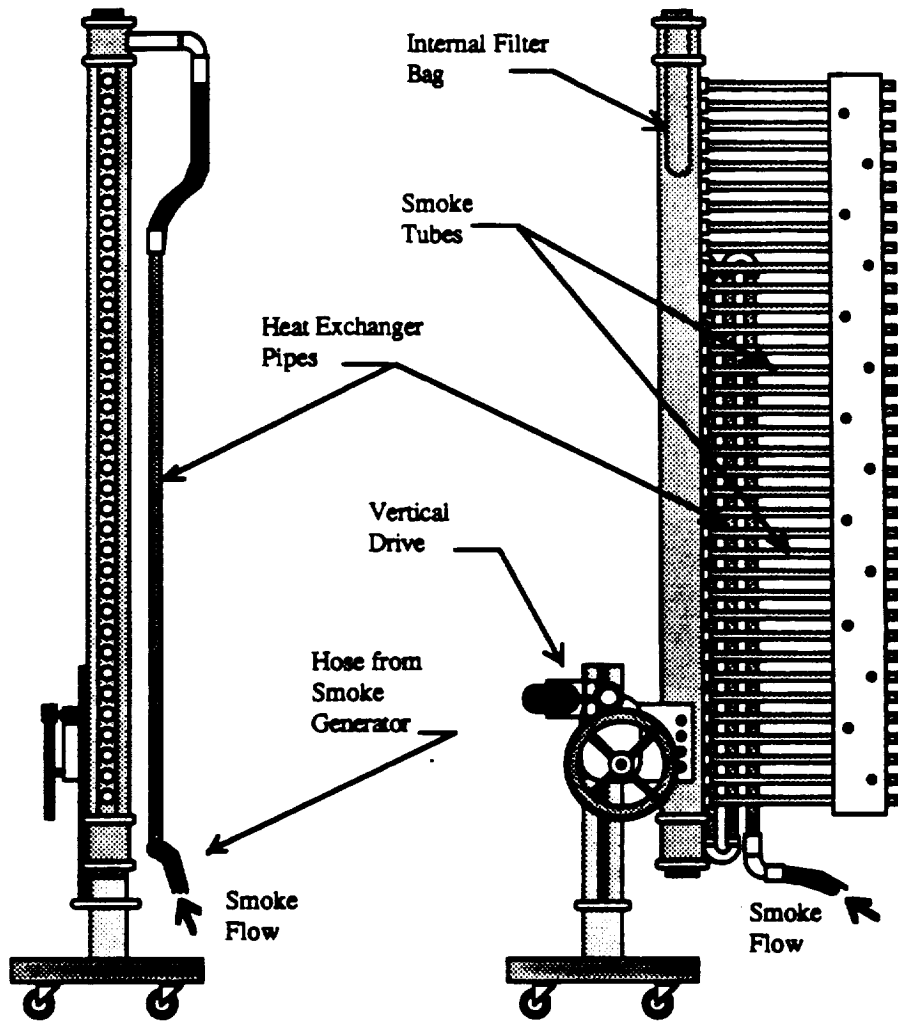
Figure 2.3   Smoke Rake
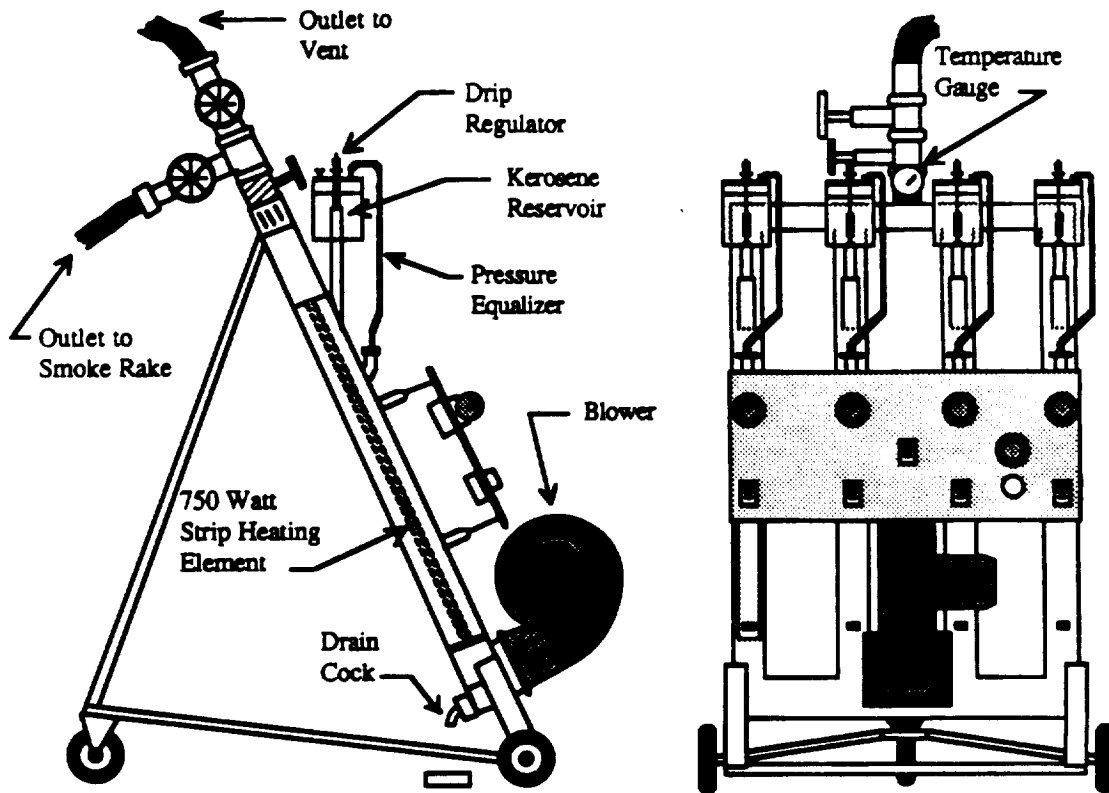
Figure 2.4   Smoke Generator

PITOT-STATIC PROBE

AIRFOIL PRESSURE TAP MODEL

P_{STATIC} P_{TOTAL}

TUBING

4W

SV SV

SC SC

EM EM EM

A/D

PDP 11/23 MINI-COMPUTER

D/A

EM   ELECTRONIC MANOMETER
4W   4-WAY VALVE
SV   SCANIVALVE
SC   SCANIVALVE SOLENOID
         CONTROLLER
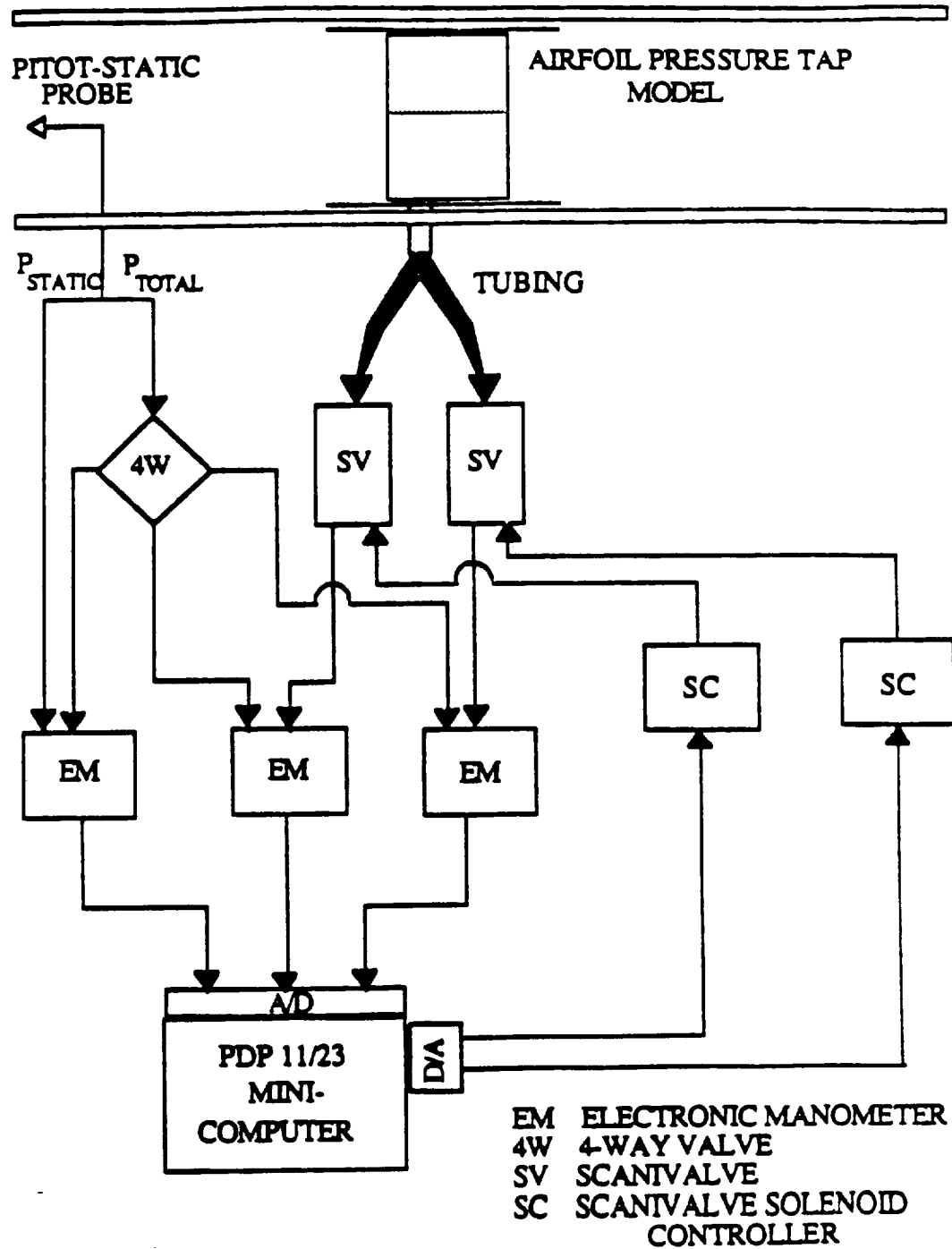
Figure 2.5   Static Pressure Measurement Equipment Schematic

P	PHOTOMULTIPLIER
PP	PHOTOMULT. POWER SUPPLY
EM	ELECTRONIC MANOMETER
BC	BURST COUNTER
FS	FREQUENCY SHIFTER
PG	PULSE GENERATOR
ST	SCHMITT TRIGGER
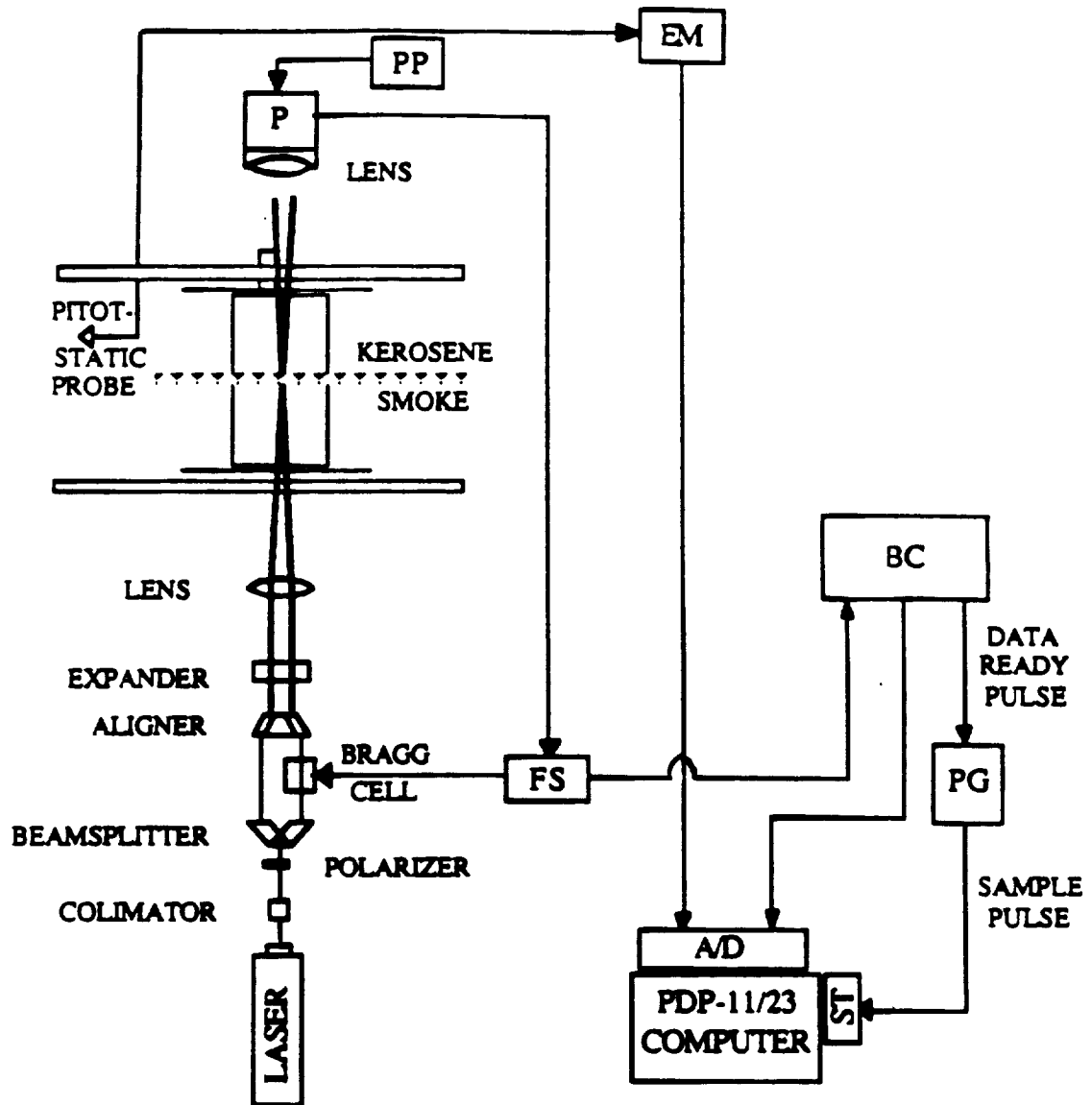
Figure 2.6   Laser Doppler Velocimetry Equipment Schematic

Receiving optics and photomultiplier

Test section

Receiving optics support frame

Rotary table

Spanwise traverser

Vertical traverser

Chordwise traverser

Table support and casters

Transmitting optics
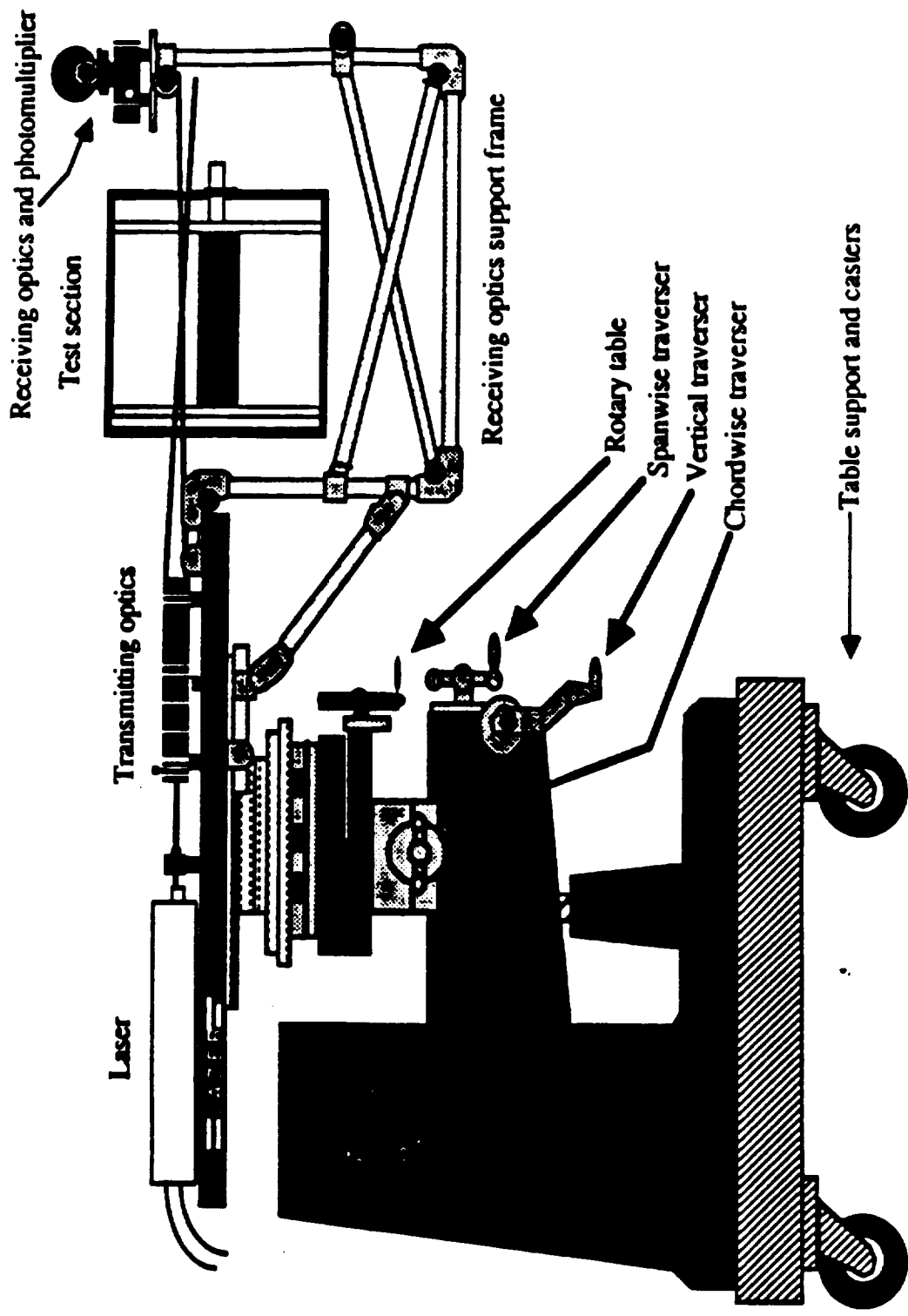
Laser

Figure 2.7   Laser Doppler Velocimetry Traversal System
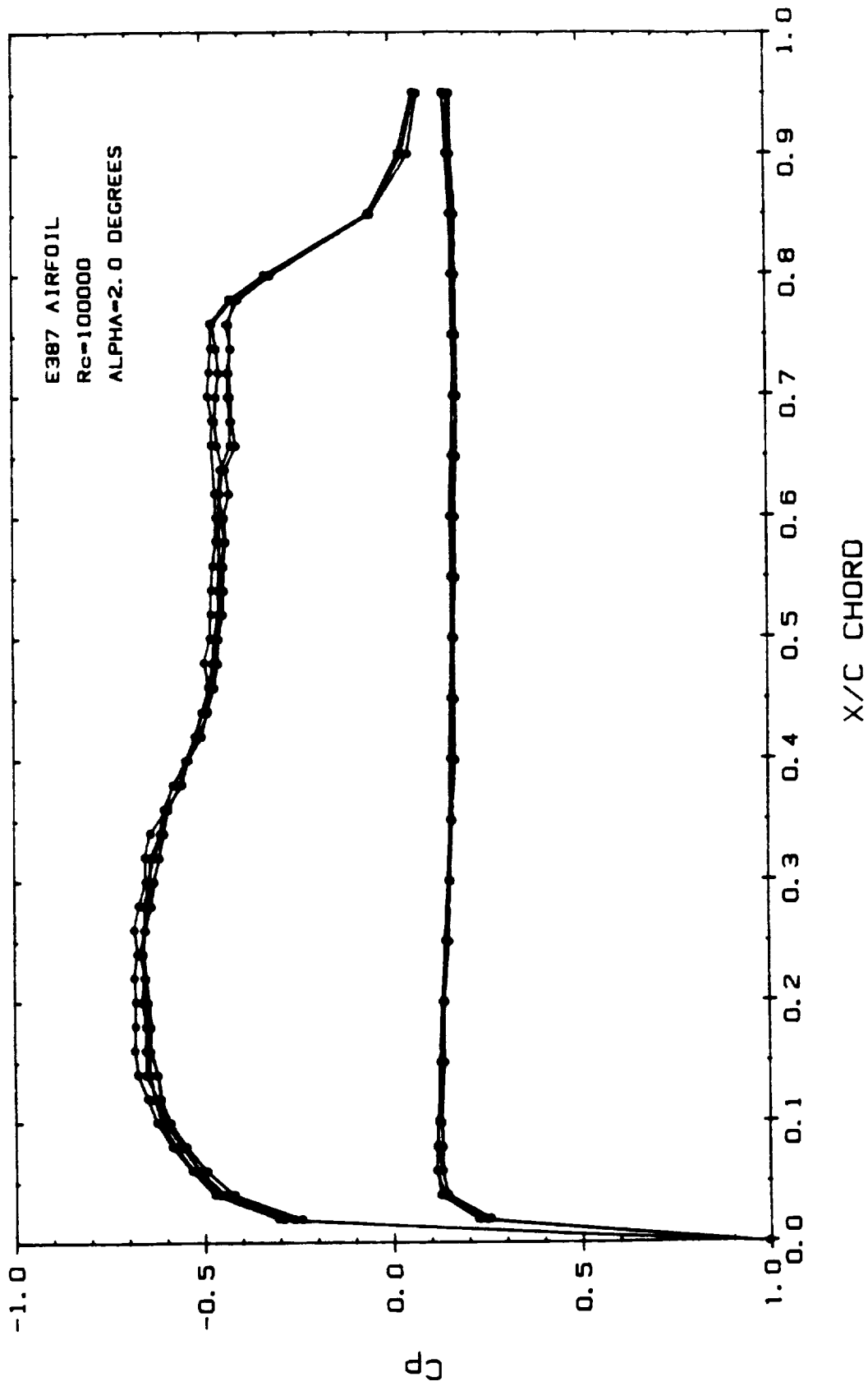
Figure 4.1   Static Pressure Measurement Repeatability for E387 Airfoil
at $R_c = 100,000$ and $\alpha = 2.0°$
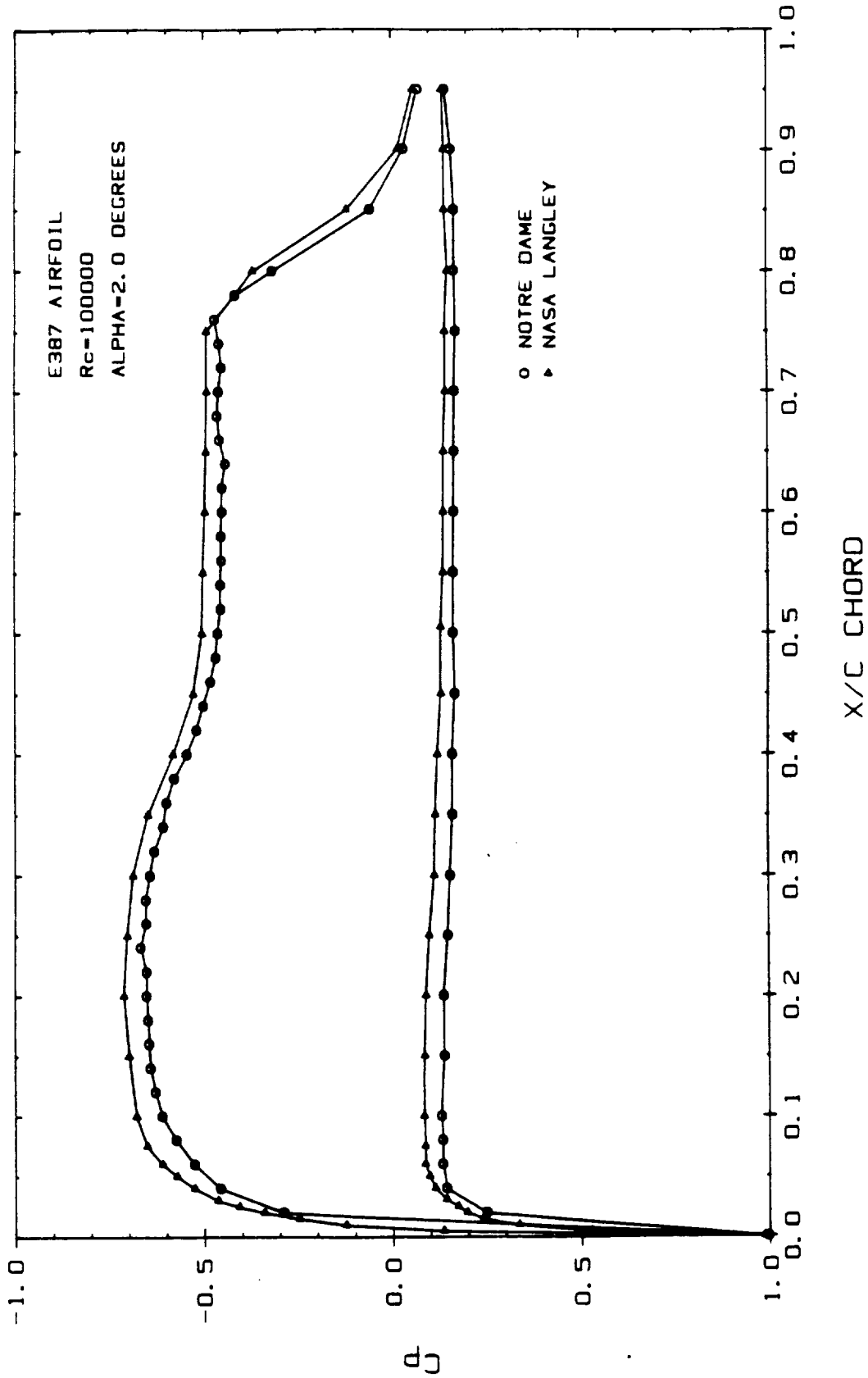
Figure 4.2   Static Pressure Measurement Comparison for Notre Dame and
              NASA Langley Tests of E387 Airfoil at R_c =100,000 and α = 2.0°
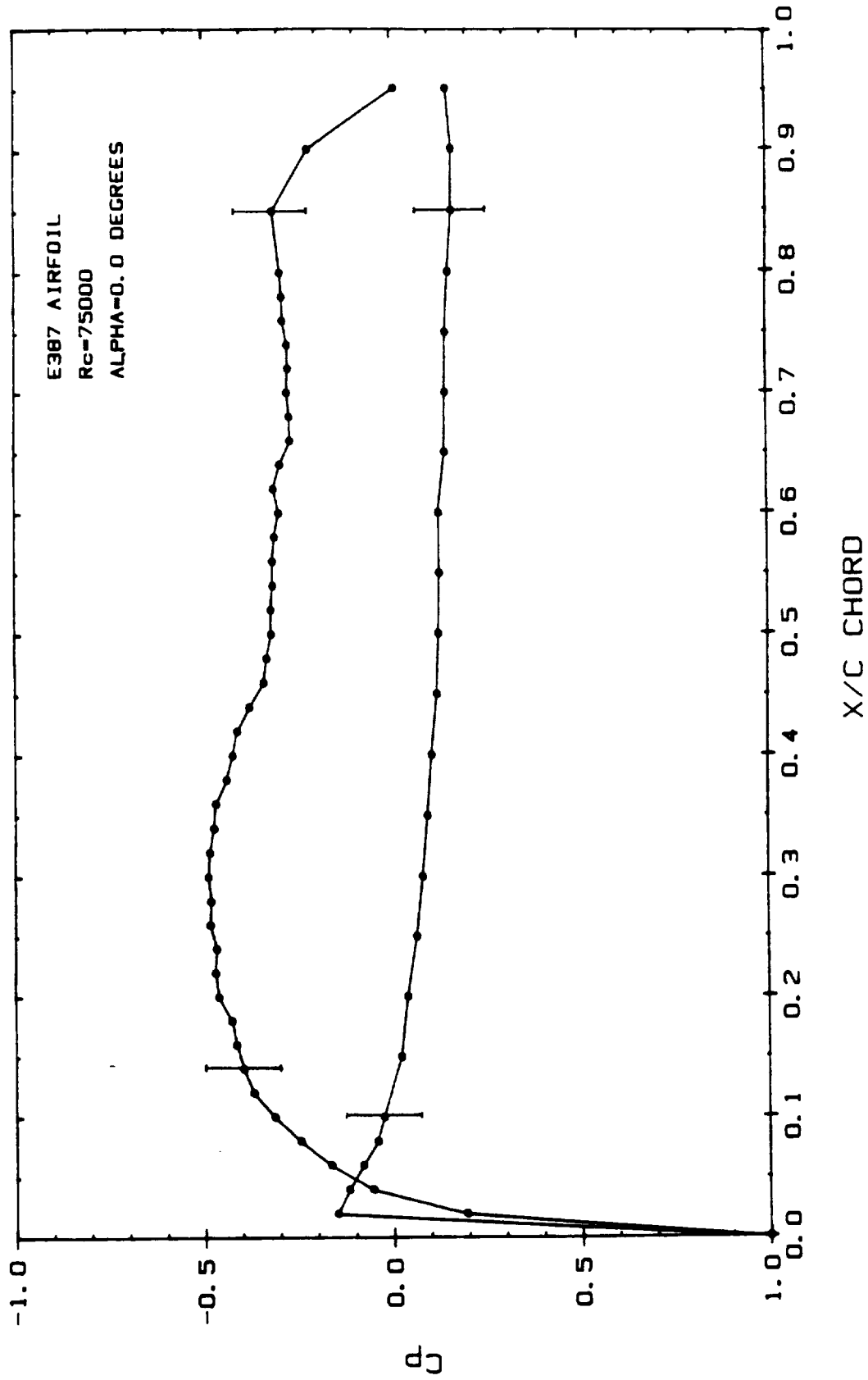
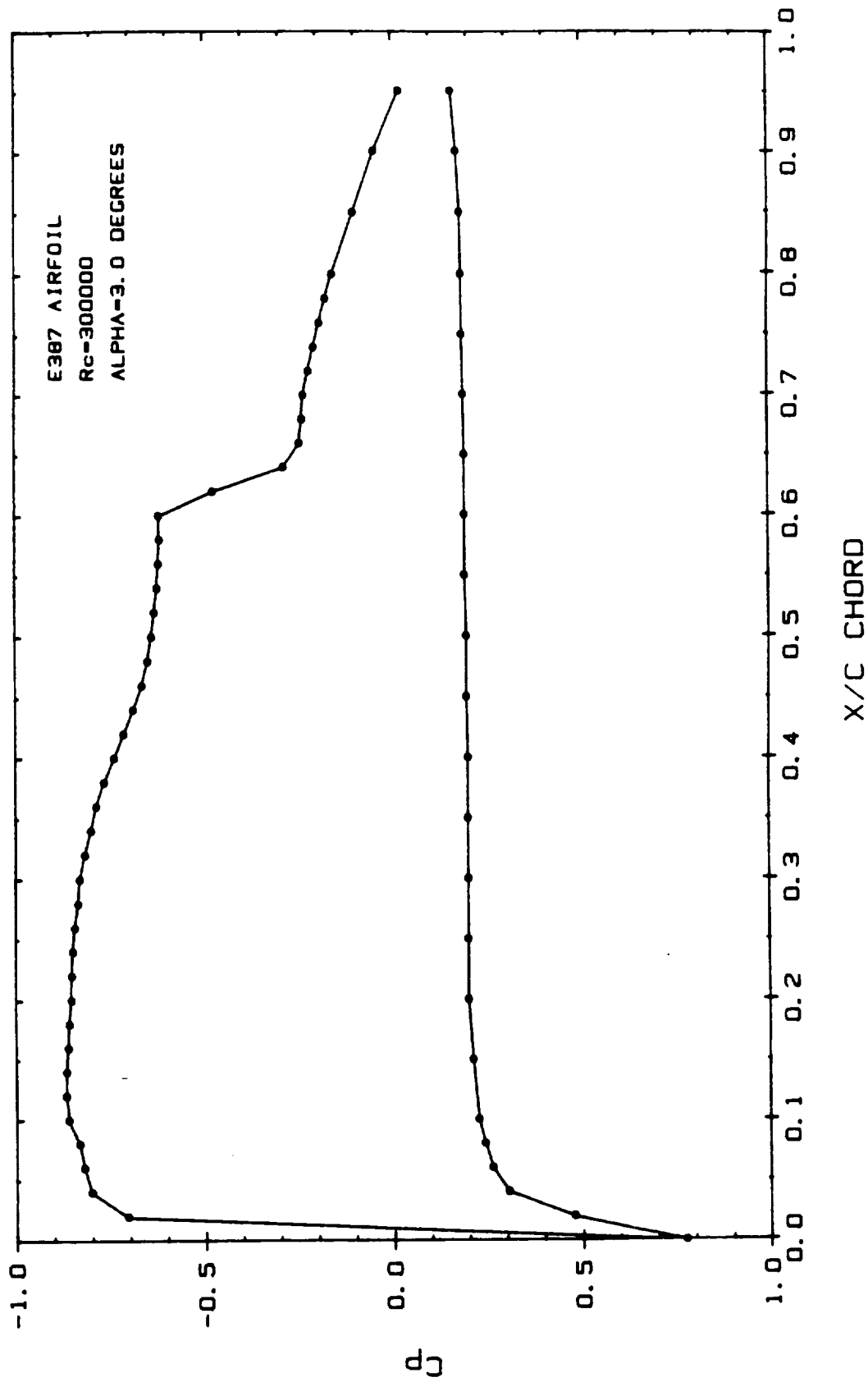Figure 4.3　Static Pressure Distribution for E387 Airfoil, $R_c = 75,000$, $\alpha = 0.0°$
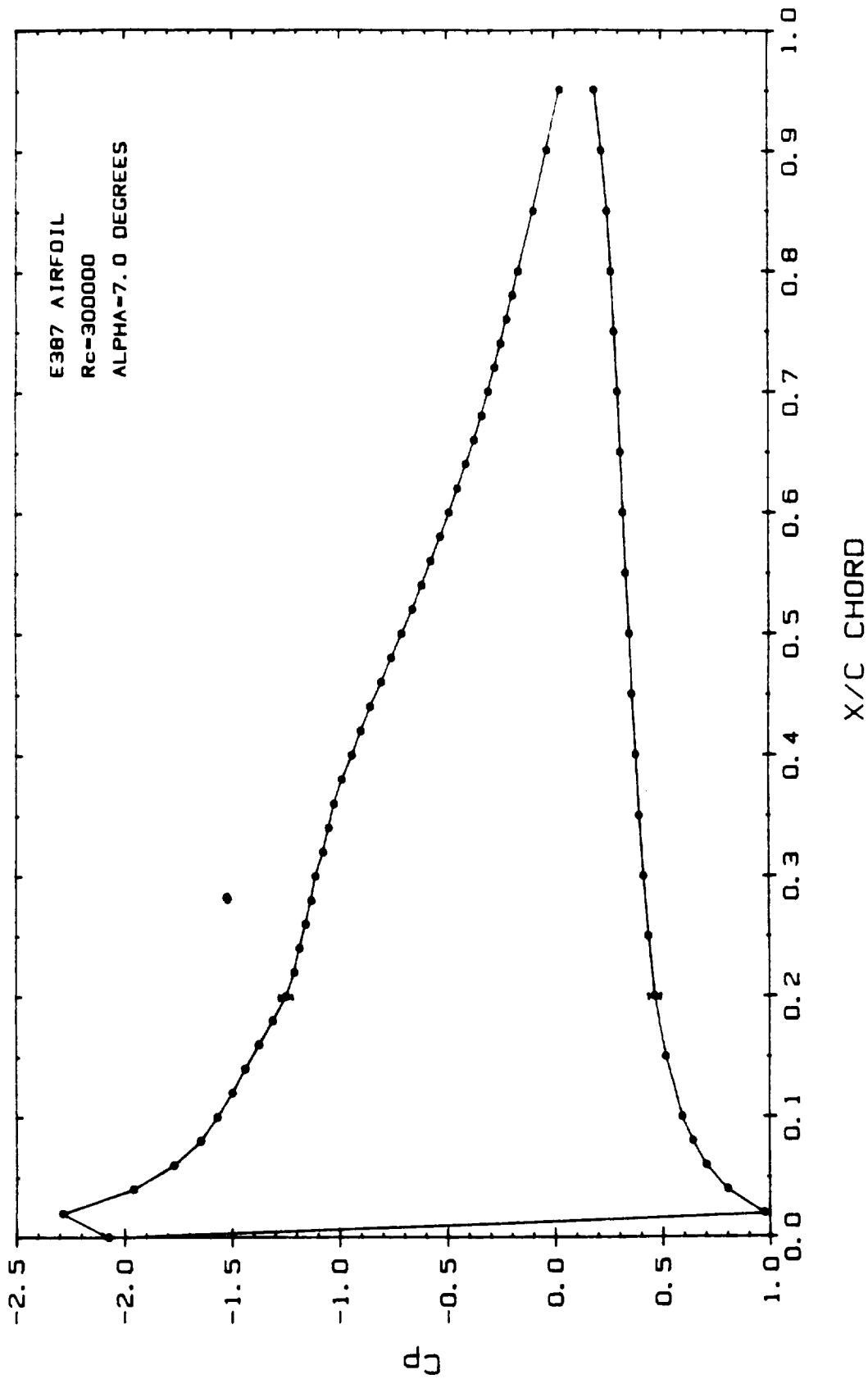
E387 AIRFOIL
Rc=75000
ALPHA=1.0 DEGREE

X/C CHORD

CP
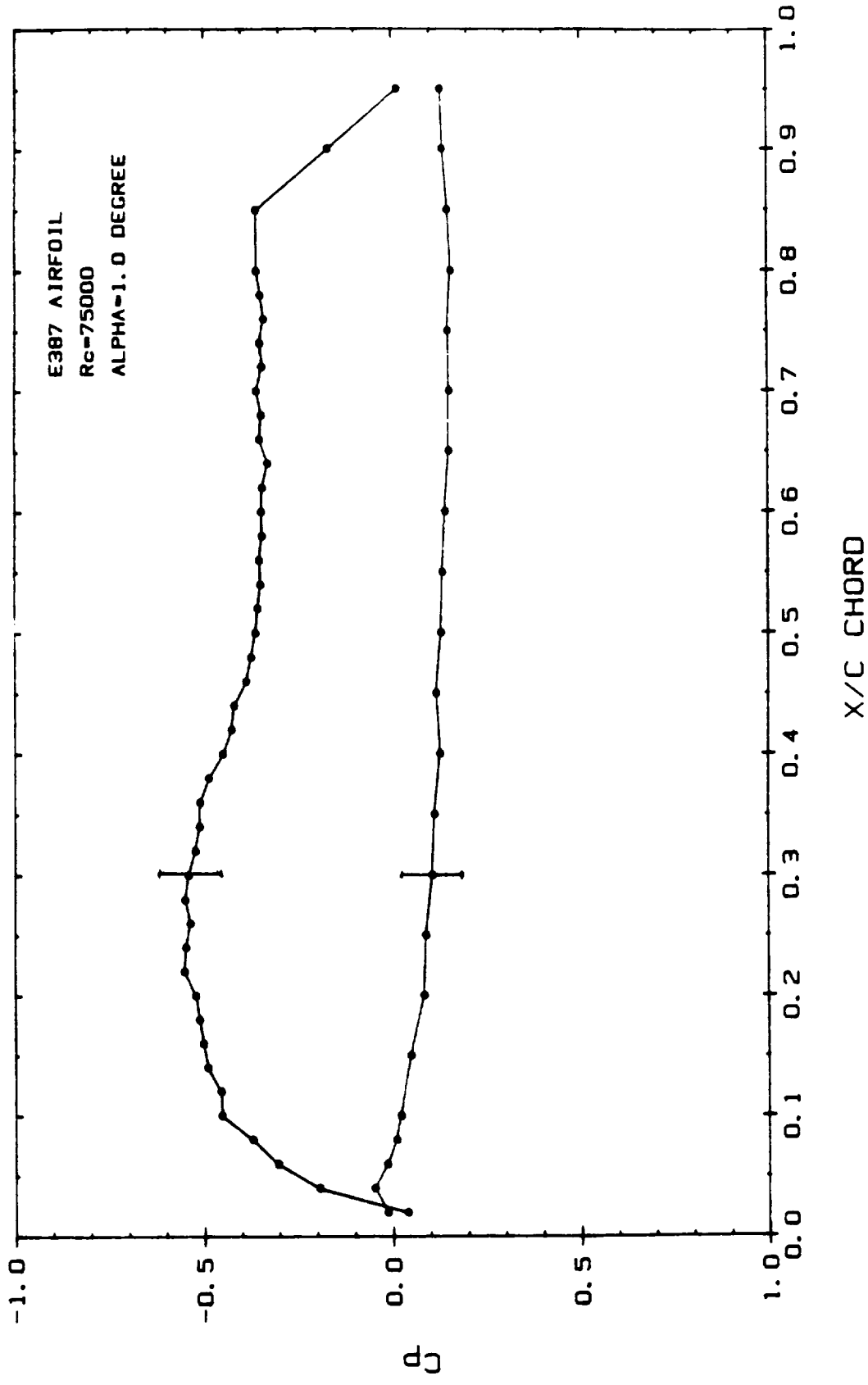
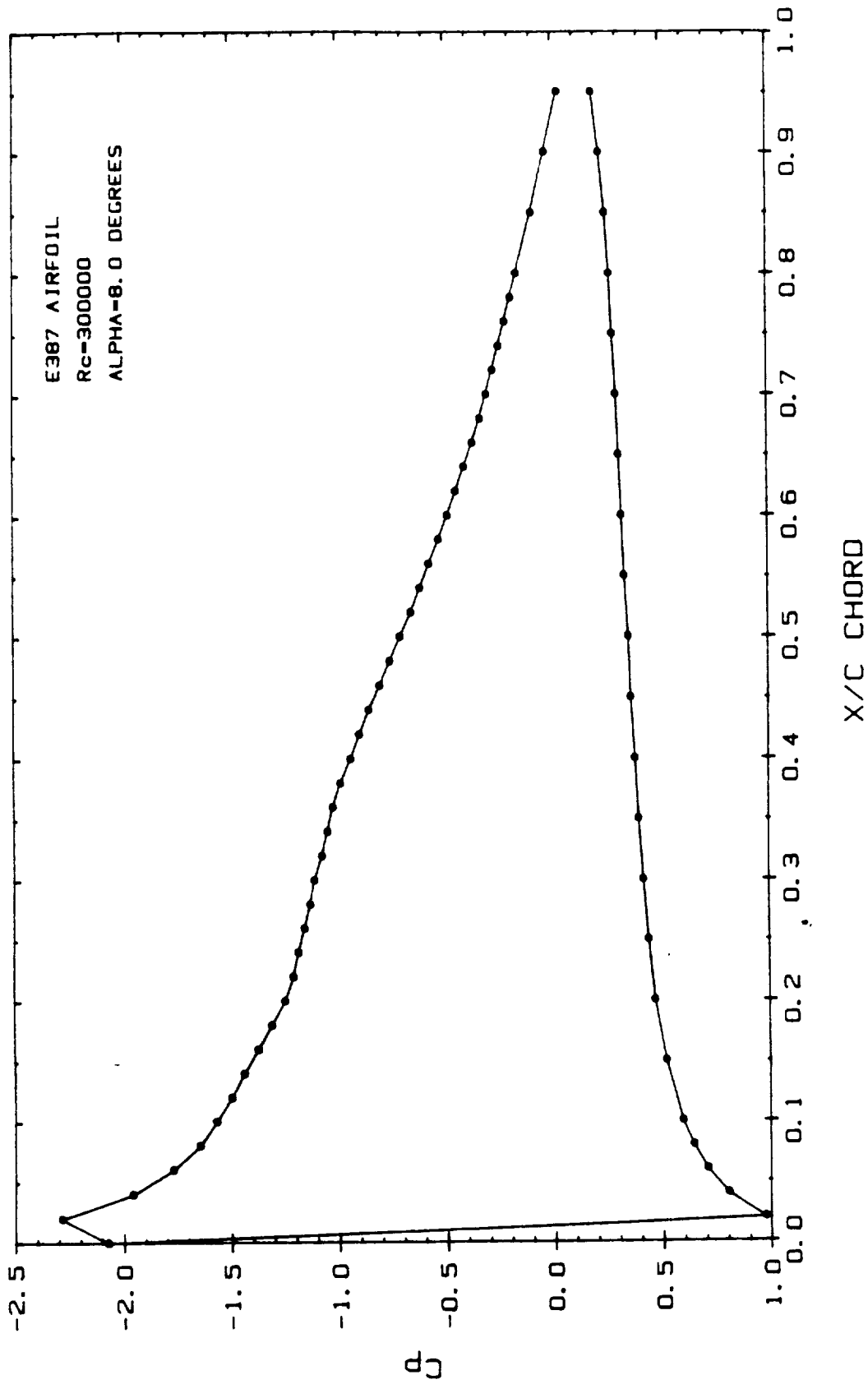Figure 4.4   Static Pressure Distribution for E387 Airfoil, $R_c = 75{,}000$, $\alpha = 1.0°$
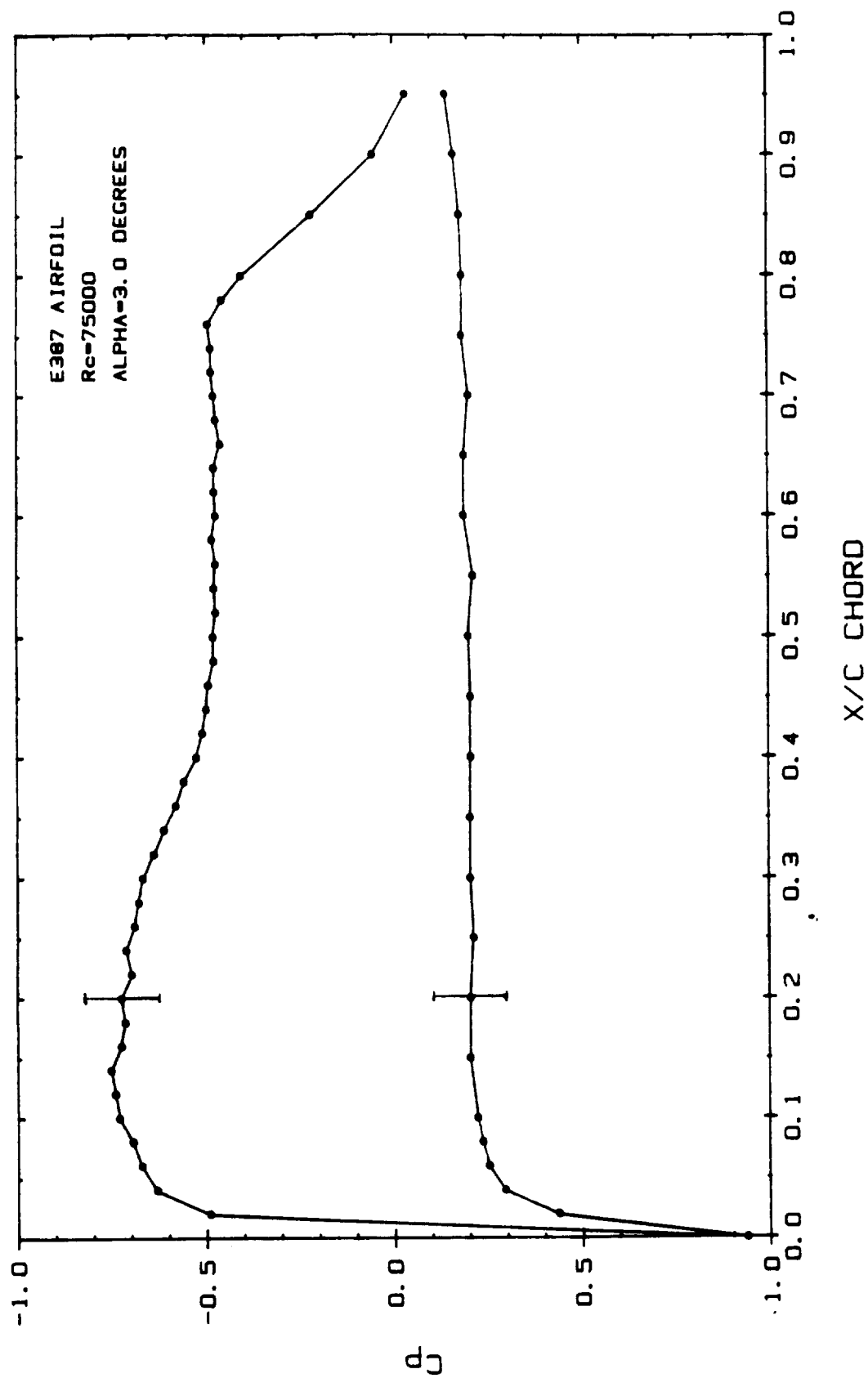
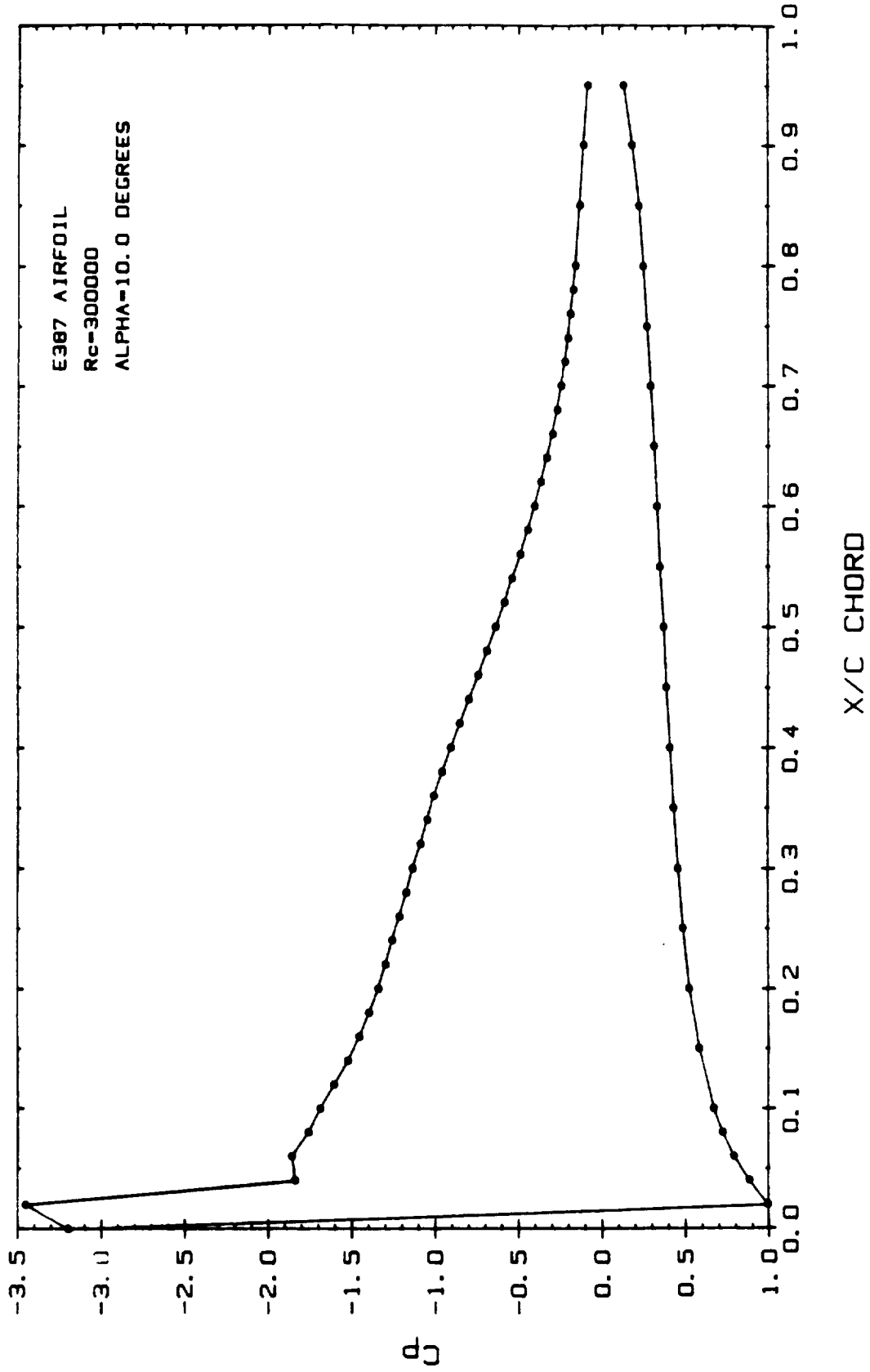Figure 4.5   Static Pressure Distribution for E387 Airfoil, $R_c = 75,000$, $\alpha = 3.0°$
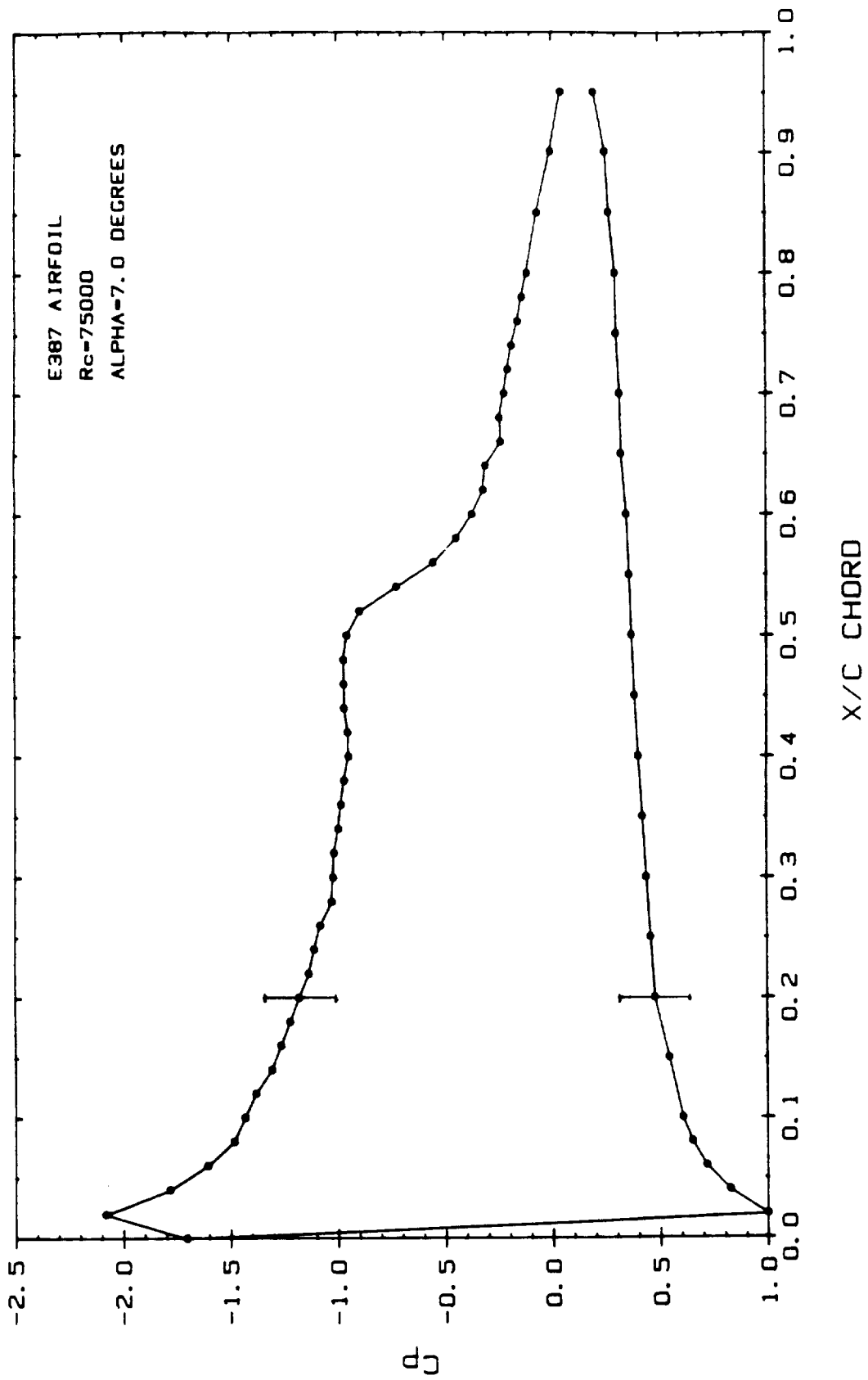
Figure 4.6   Static Pressure Distribution for E387 Airfoil. $R_c = 75,000$, $\alpha = 7.0°$

E387 AIRFOIL
Rc=75000
ALPHA=7.0 DEGREES

X/C CHORD

Cp

59

E387 AIRFOIL
Rc=75000
ALPHA=8.0 DEGREES

X/C CHORD

C_p
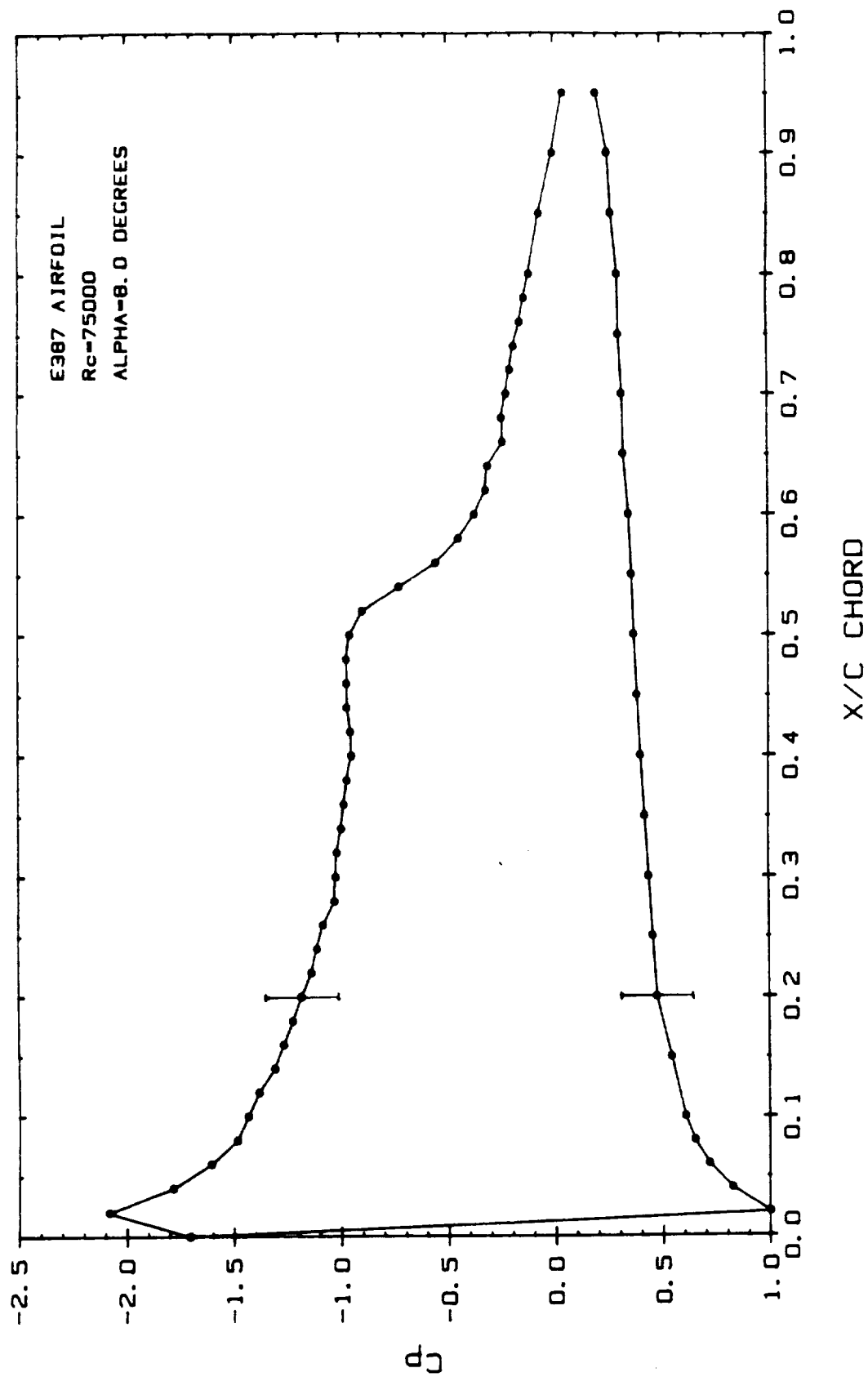
Figure 4.7   Static Pressure Distribution for E387 Airfoil, R_c = 75,000 , α = 8.0°
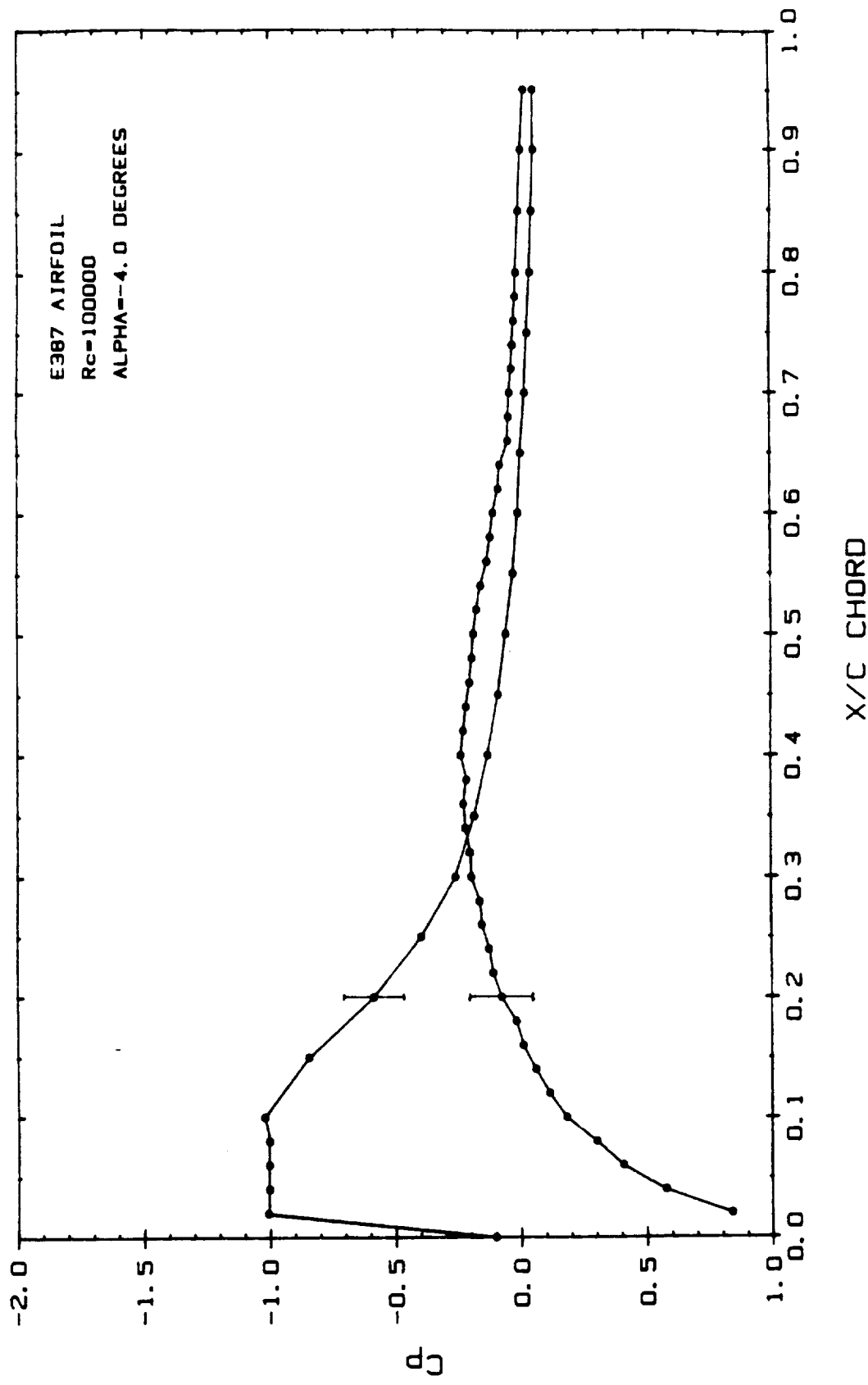
Figure 4.8   Static Pressure Distribution for E387 Airfoil
$R_c = 100,000$, $\alpha = -4.0°$

X/C CHORD
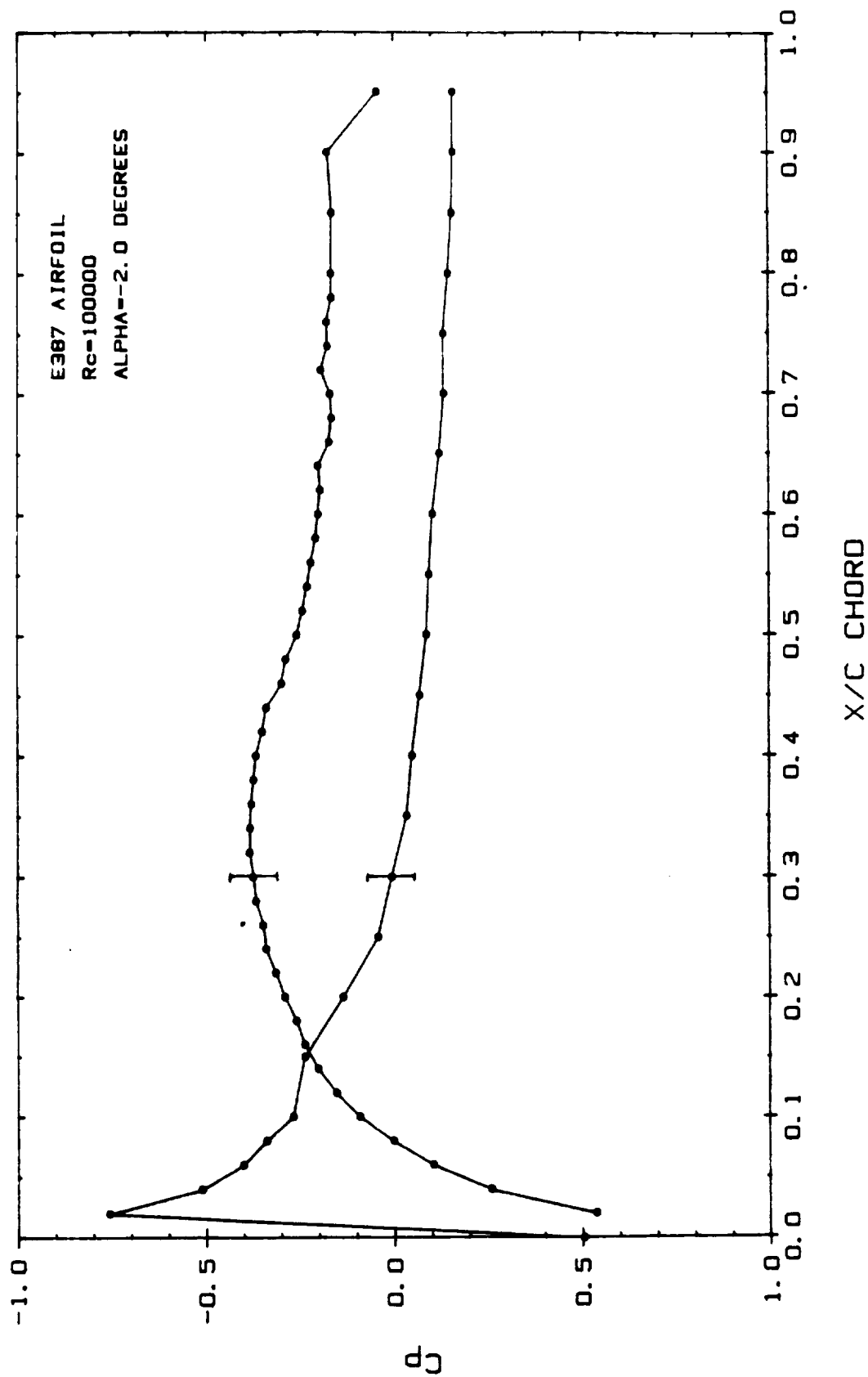
Figure 4.9   Static Pressure Distribution for E387 Airfoil
R_c = 100,000 , α = -2.0°
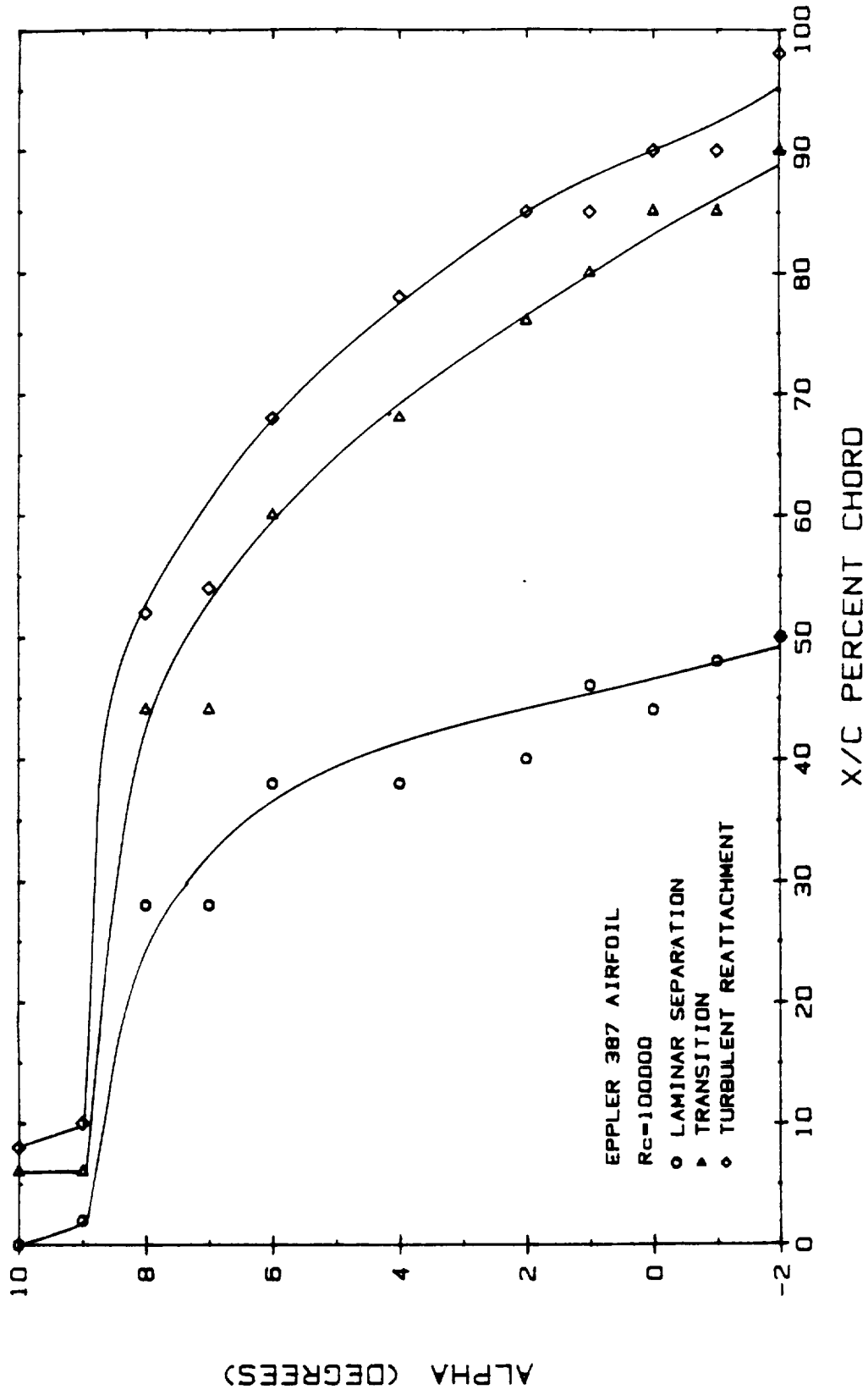
E387 AIRFOIL
Rc=100000
ALPHA=-1.0 DEGREE

X/C CHORD
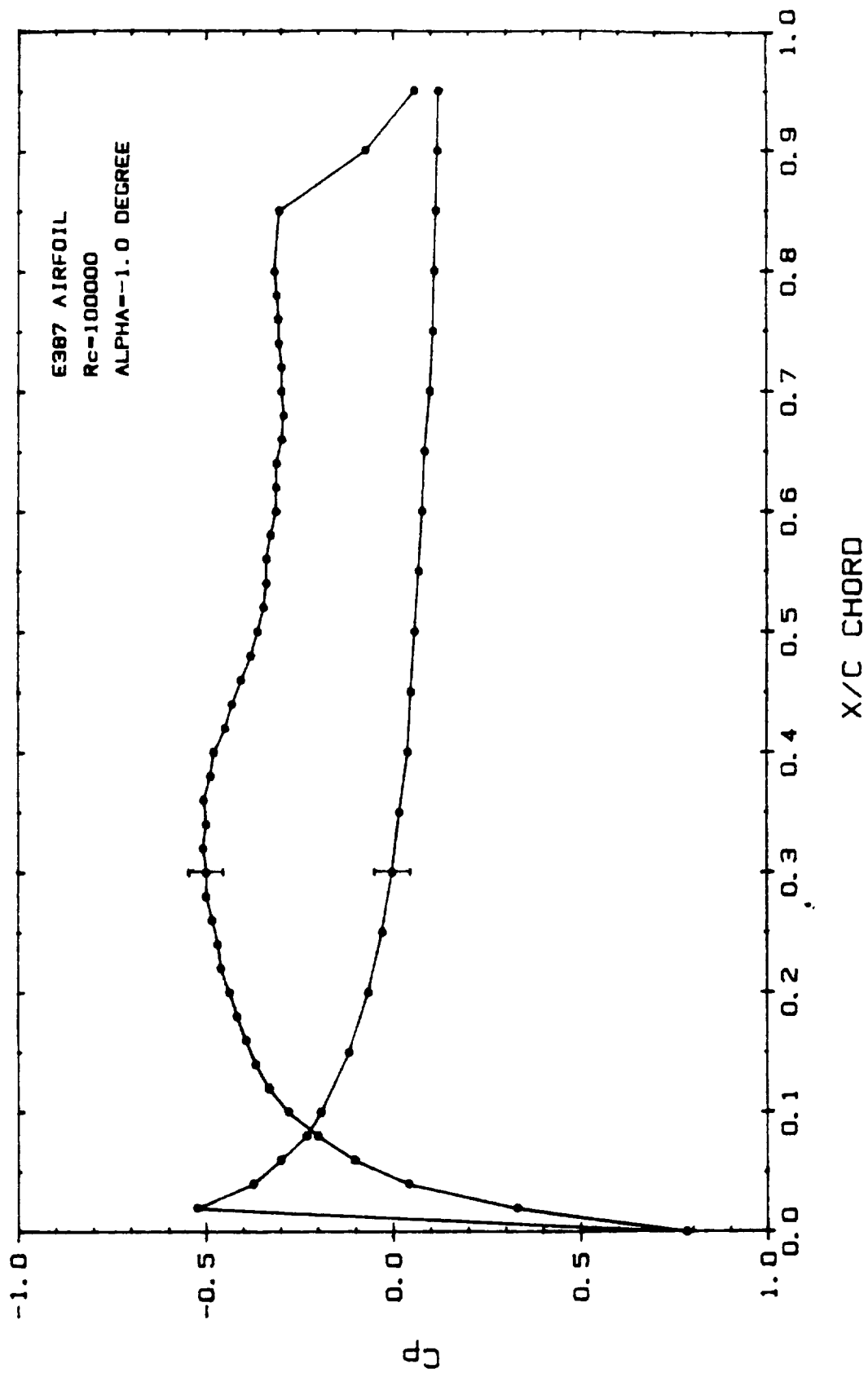
Figure 4.10   Static Pressure Distribution for E387 Airfoil
$R_c = 100,000$, $\alpha = -1.0°$

E387 AIRFOIL
Rc=100000
ALPHA-0.0 DEGREES

X/C CHORD
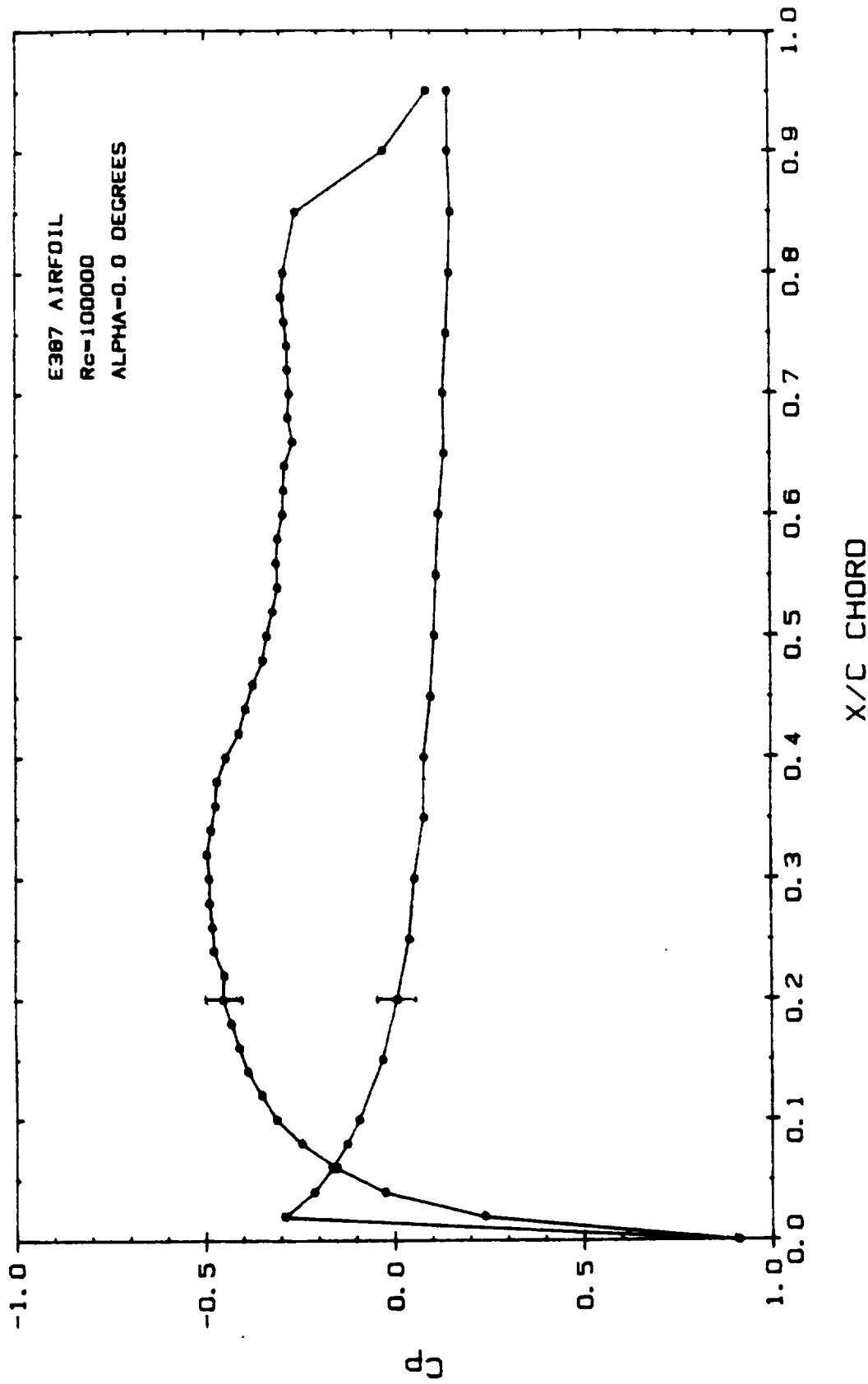
Figure 4.11   Static Pressure Distribution for E387 Airfoil
$R_c = 100,000$, $\alpha = 0.0°$
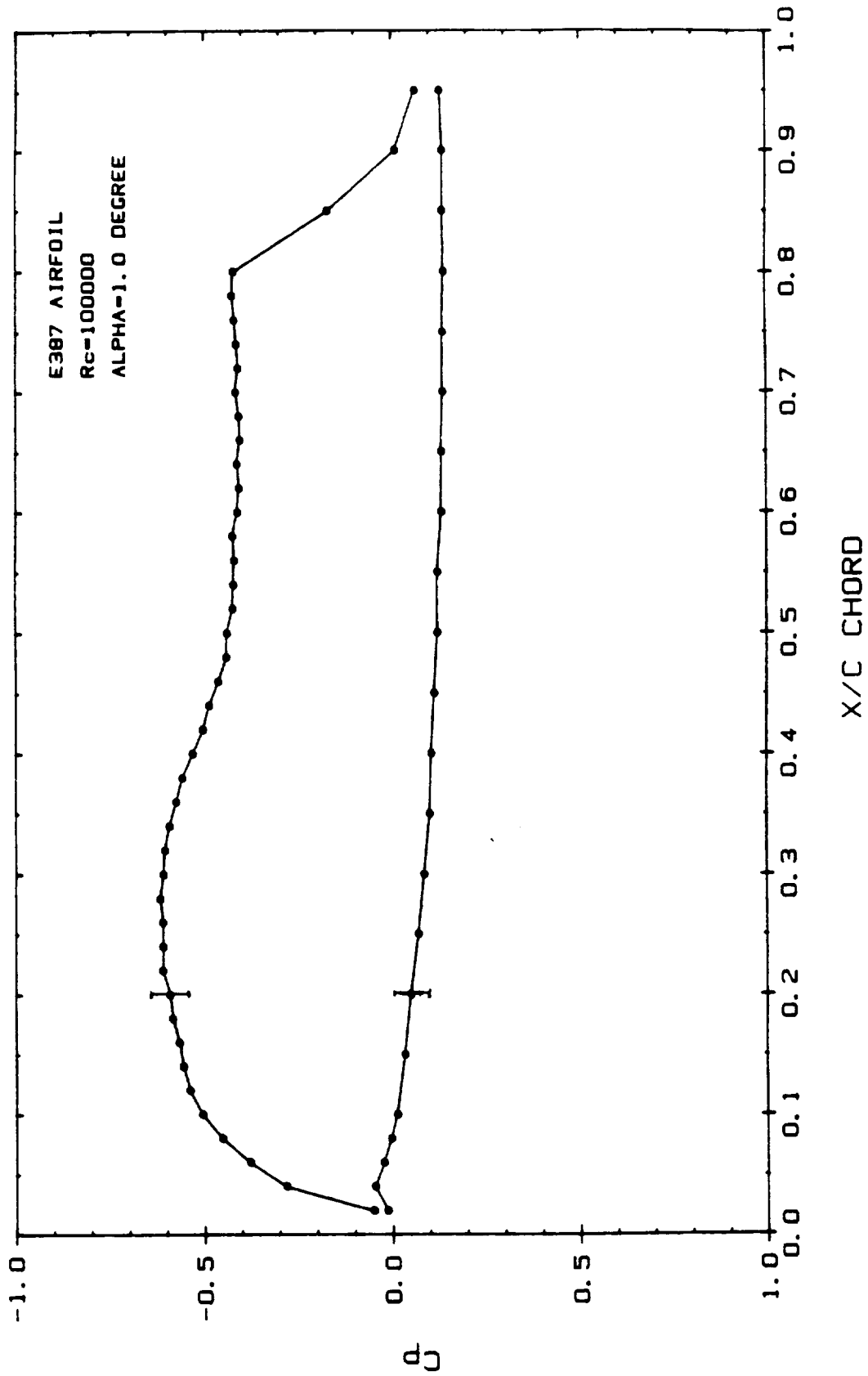
Figure 4.12 Static Pressure Distribution for E387 Airfoil
R_c = 100,000 , α = 1.0°
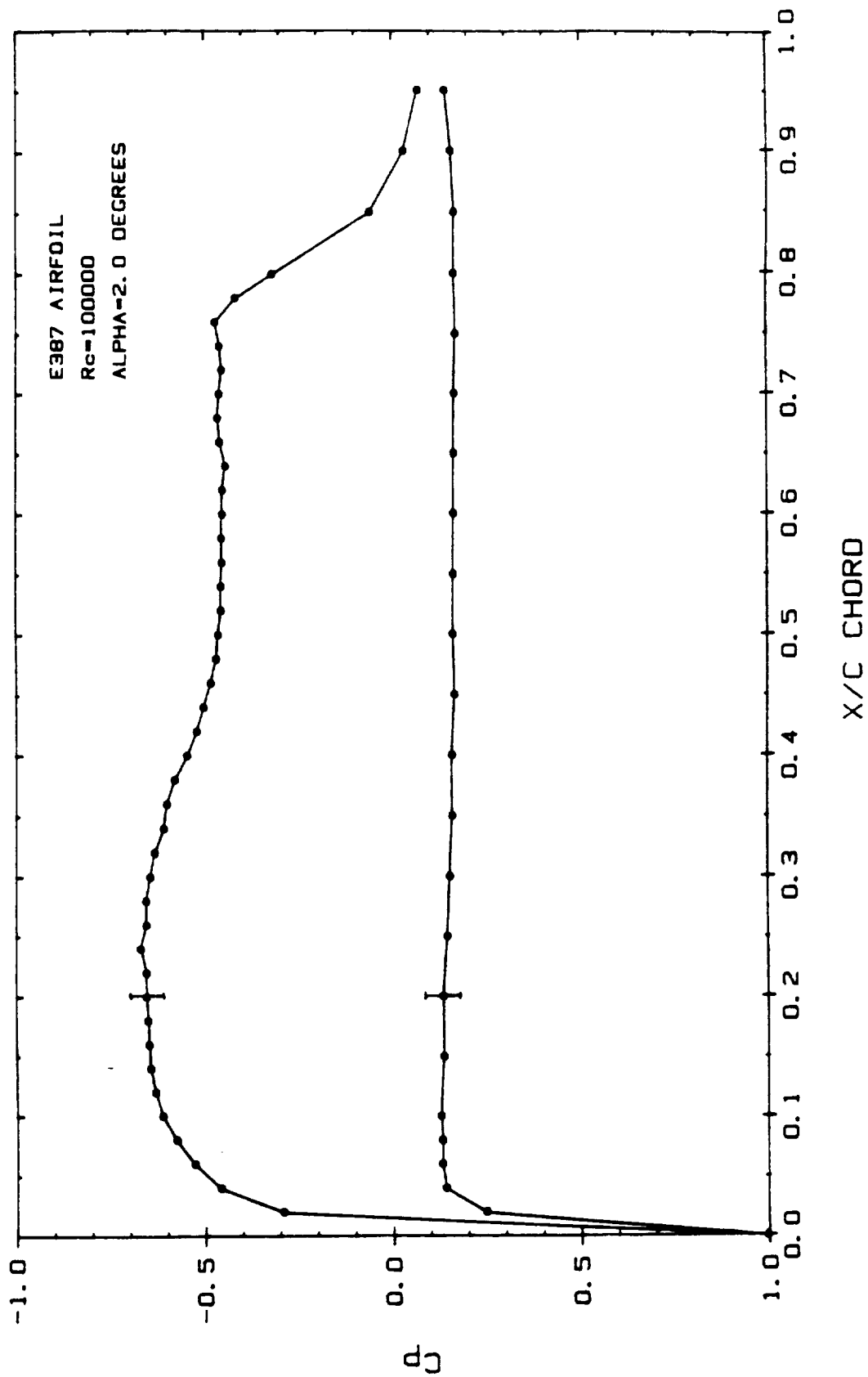
Figure 4.13 Static Pressure Distribution for E387 Airfoil
$R_c = 100,000$, $\alpha = 2.0°$

E387 AIRFOIL
Rc=100000
ALPHA=4.0 DEGREES

X/C CHORD
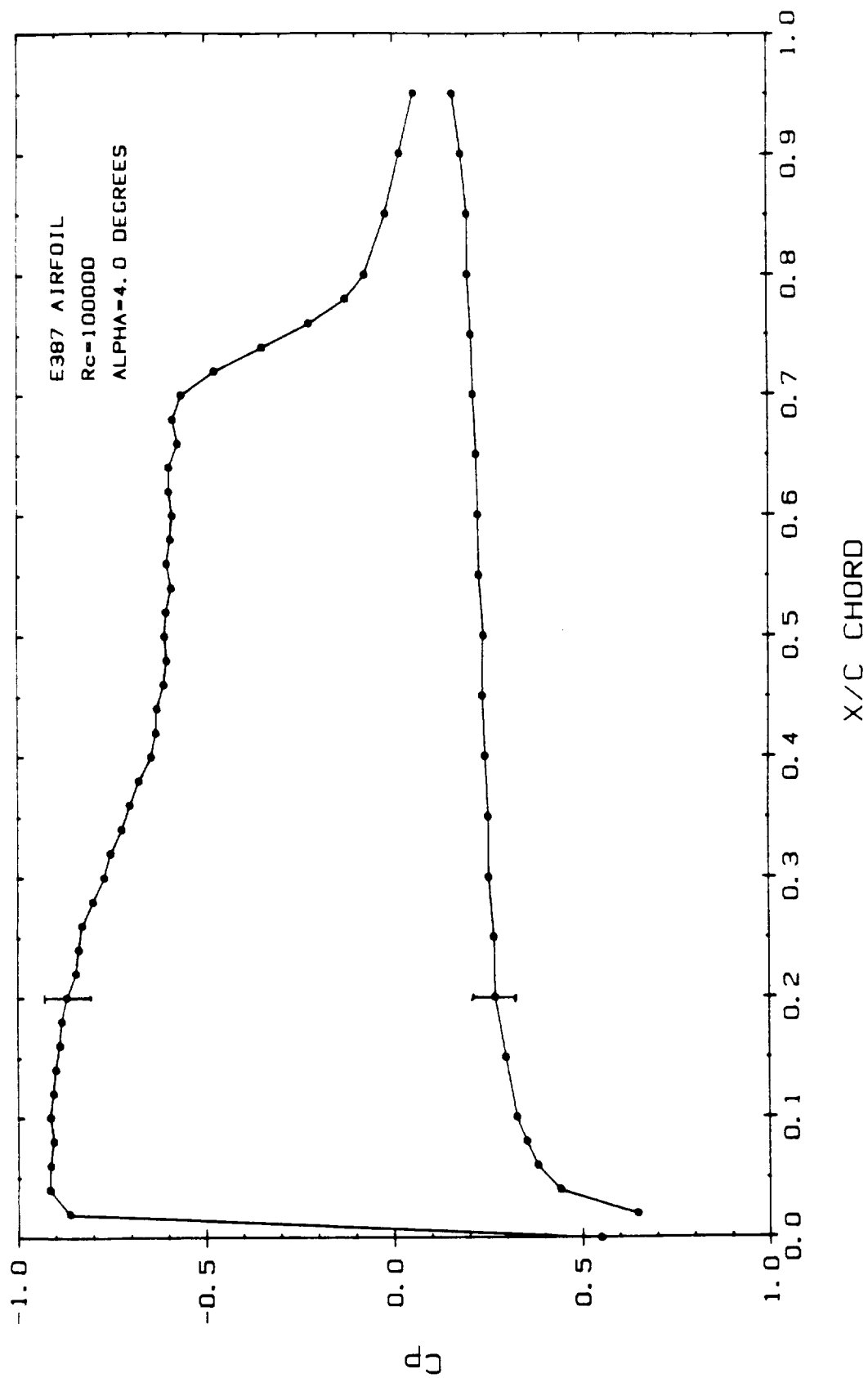
Figure 4.14 Static Pressure Distribution for E387 Airfoil
$R_c = 100,000$, $\alpha = 4.0°$

E387 AIRFOIL
Rc=100000
ALPHA=6.0 DEGREES

X/C CHORD

CP
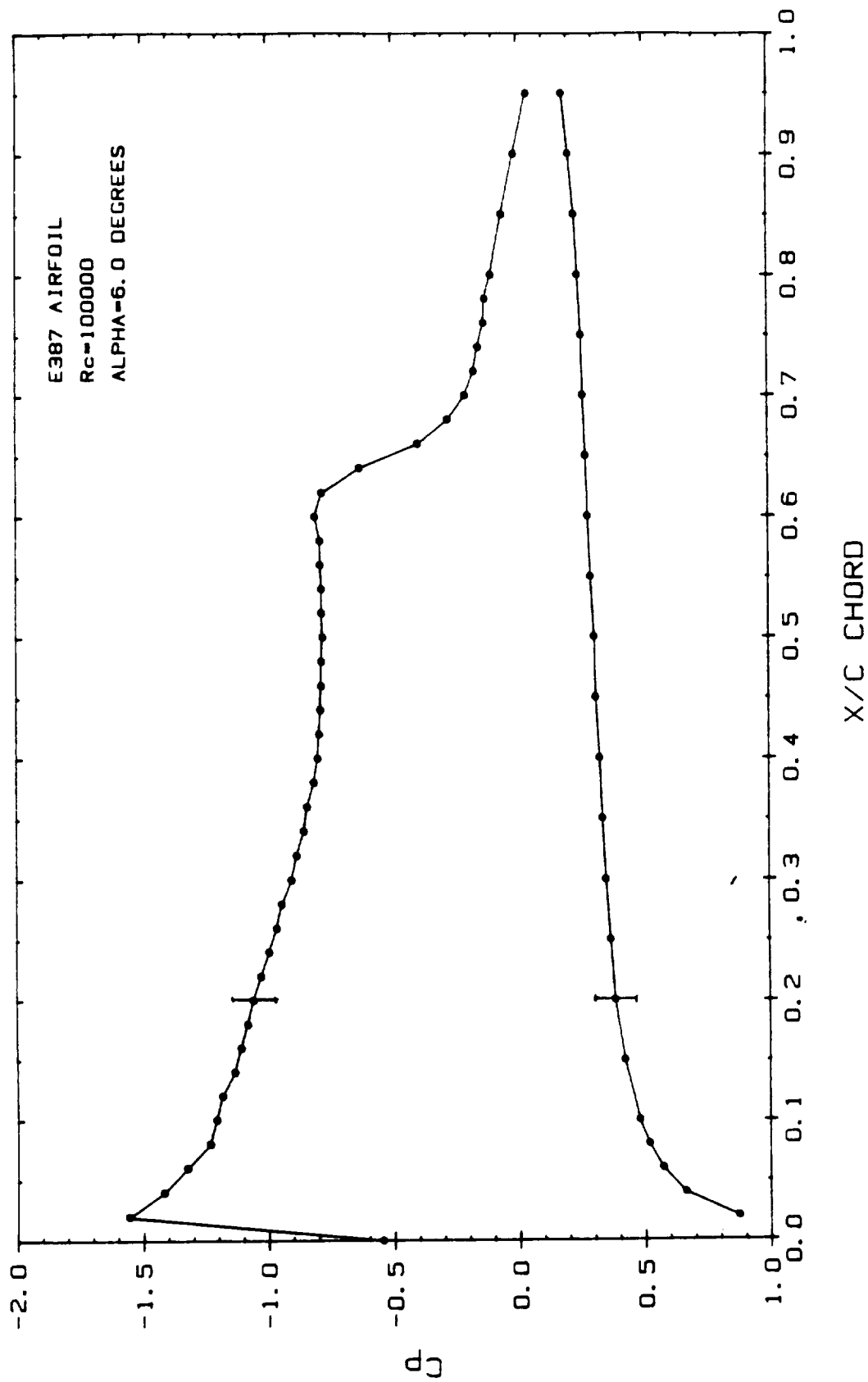
Figure 4.15 Static Pressure Distribution for E387 Airfoil
$R_c = 100,000$, $\alpha = 6.0°$

E387 AIRFOIL
Rc=100000
ALPHA=7.0 DEGREES

X/C CHORD
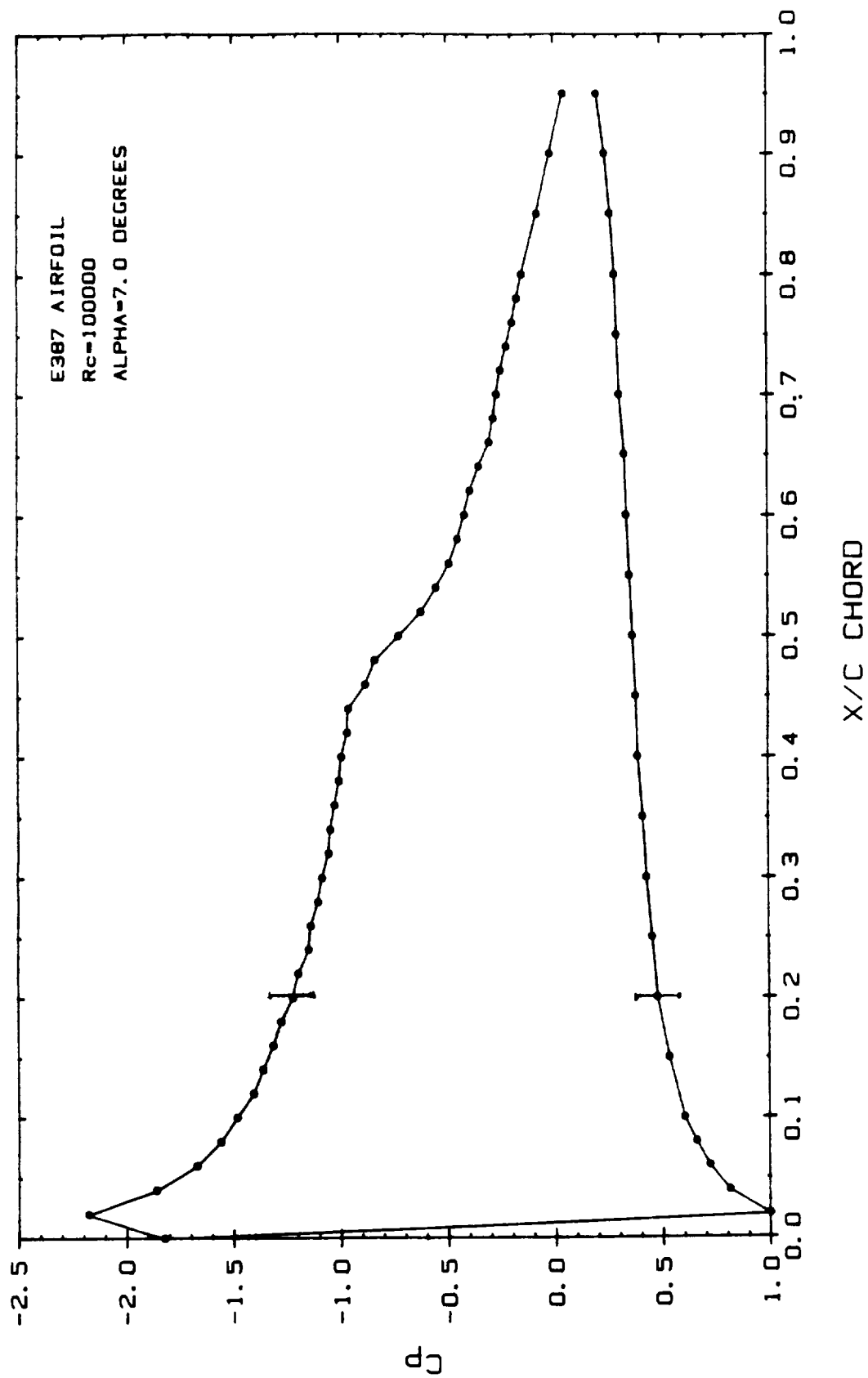
Figure 4.16   Static Pressure Distribution for E387 Airfoil
$R_c = 100,000$, $\alpha = 7.0°$

E387 AIRFOIL
Rc=100000
ALPHA=8.0 DEGREES

X/C CHORD

Cp
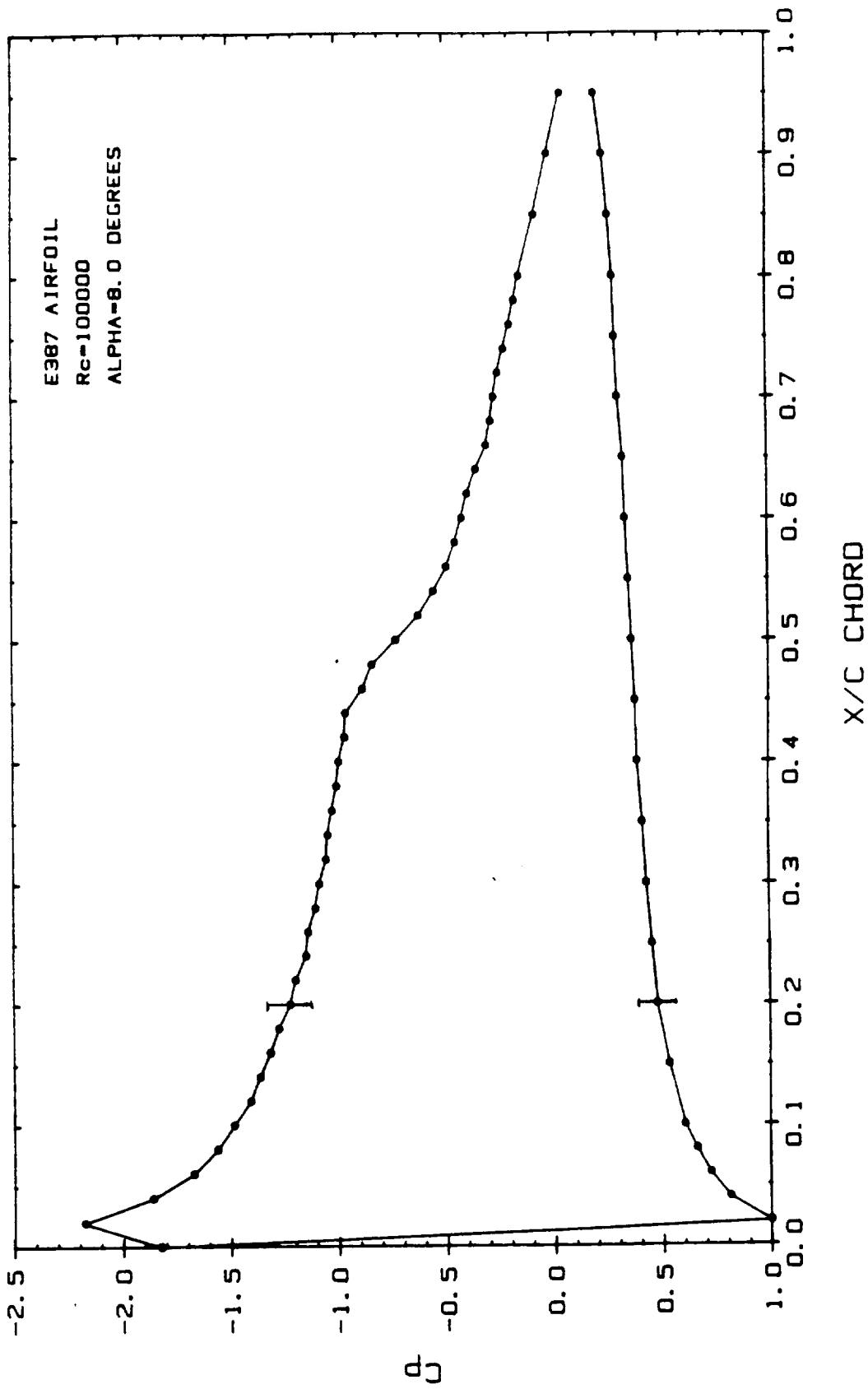
Figure 4.17   Static Pressure Distribution for E387 Airfoil
$R_c = 100,000$, $\alpha = 8.0°$
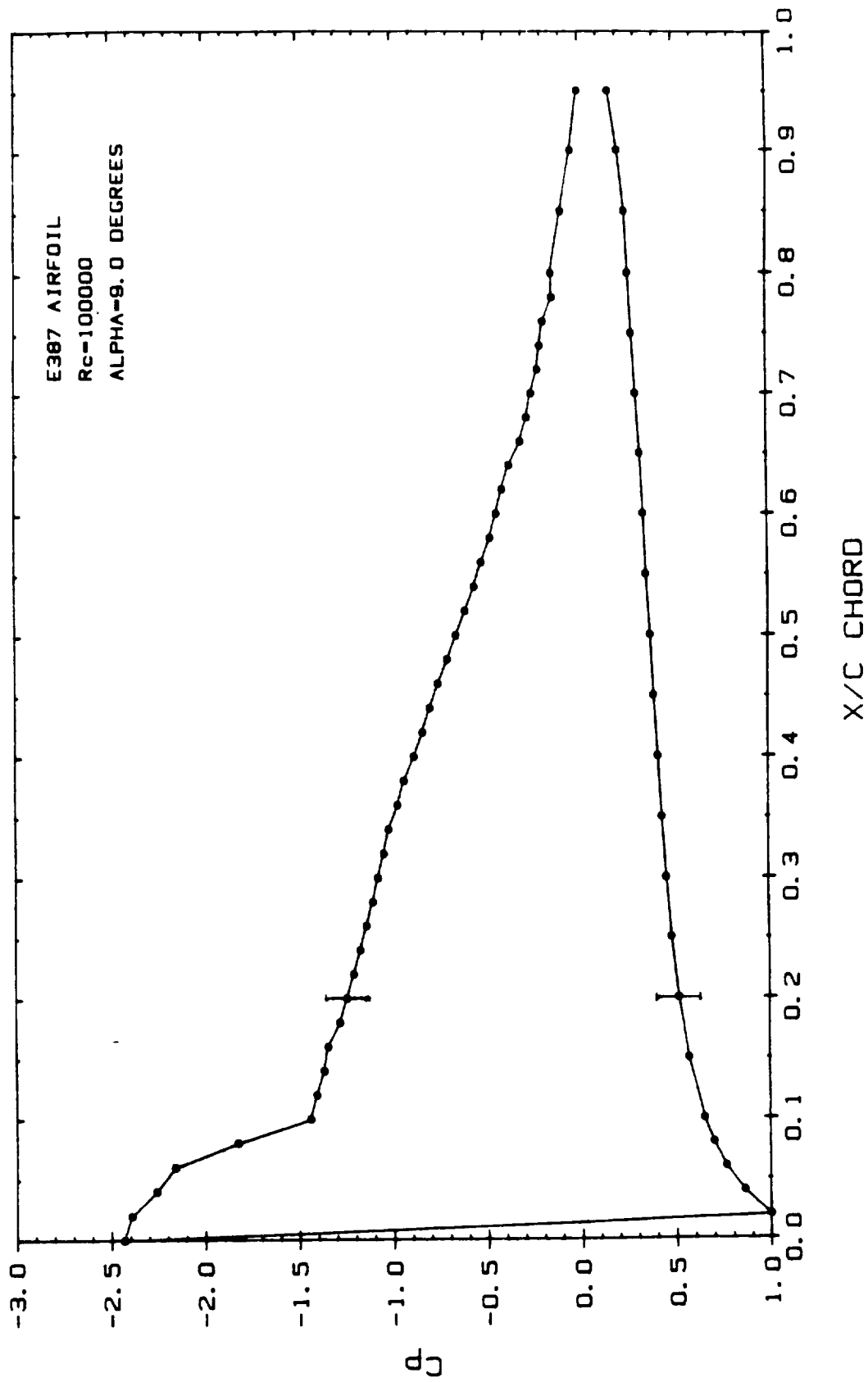
Figure 4.18   Static Pressure Distribution for E387 Airfoil
$R_c = 100,000$, $\alpha = 9.0°$

E387 AIRFOIL
Rc=100000
ALPHA=10.0 DEGREES

X/C CHORD
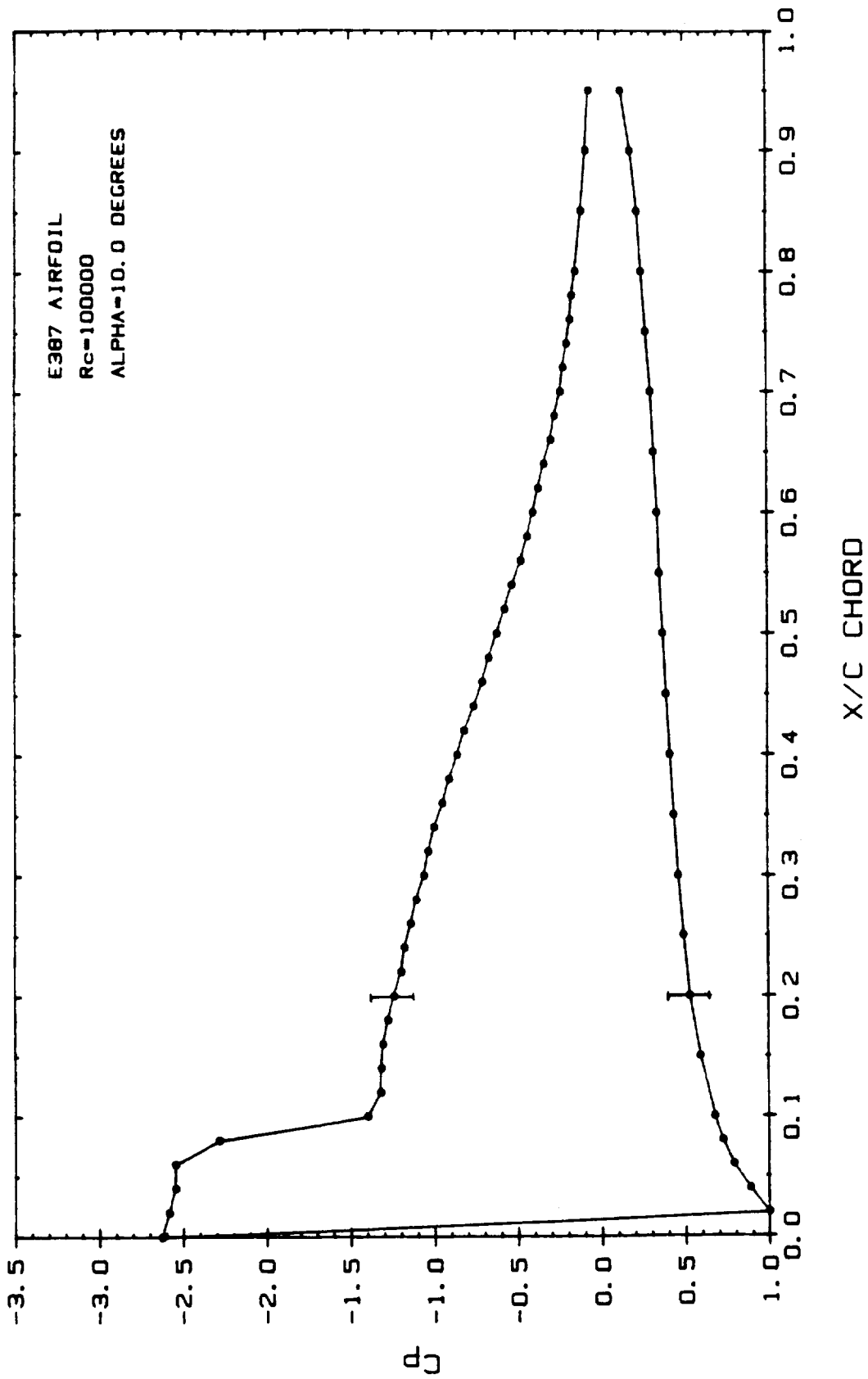
Figure 4.19   Static Pressure Distribution for E387 Airfoil
$R_c = 100,000$, $\alpha = 10.0°$
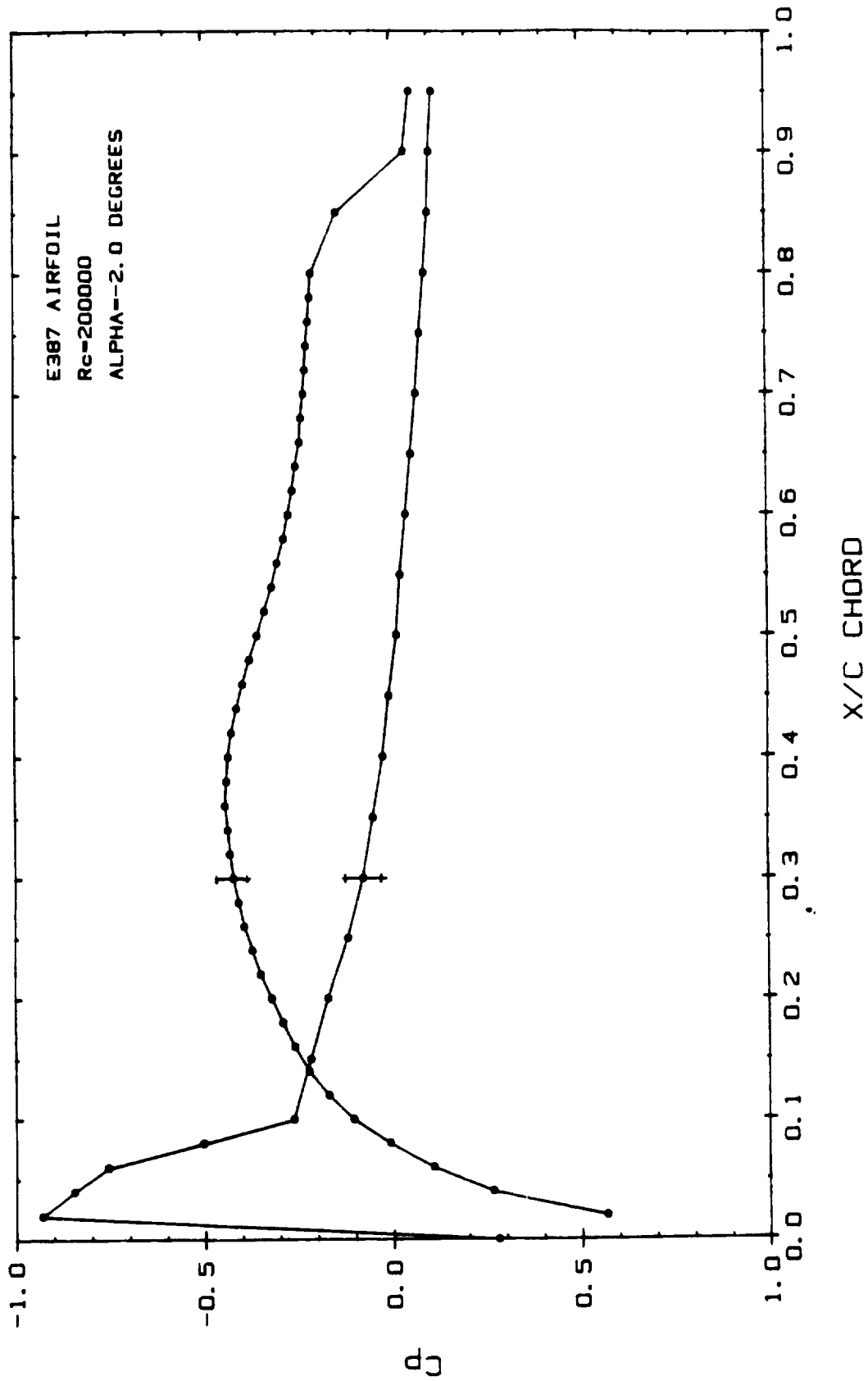
Figure 4.20 Static Pressure Distribution for E387 Airfoil
$R_c = 200,000$, $\alpha = -2.0°$

E387 AIRFOIL
Rc=200000
ALPHA=-1.0 DEGREE

X/C CHORD

CP
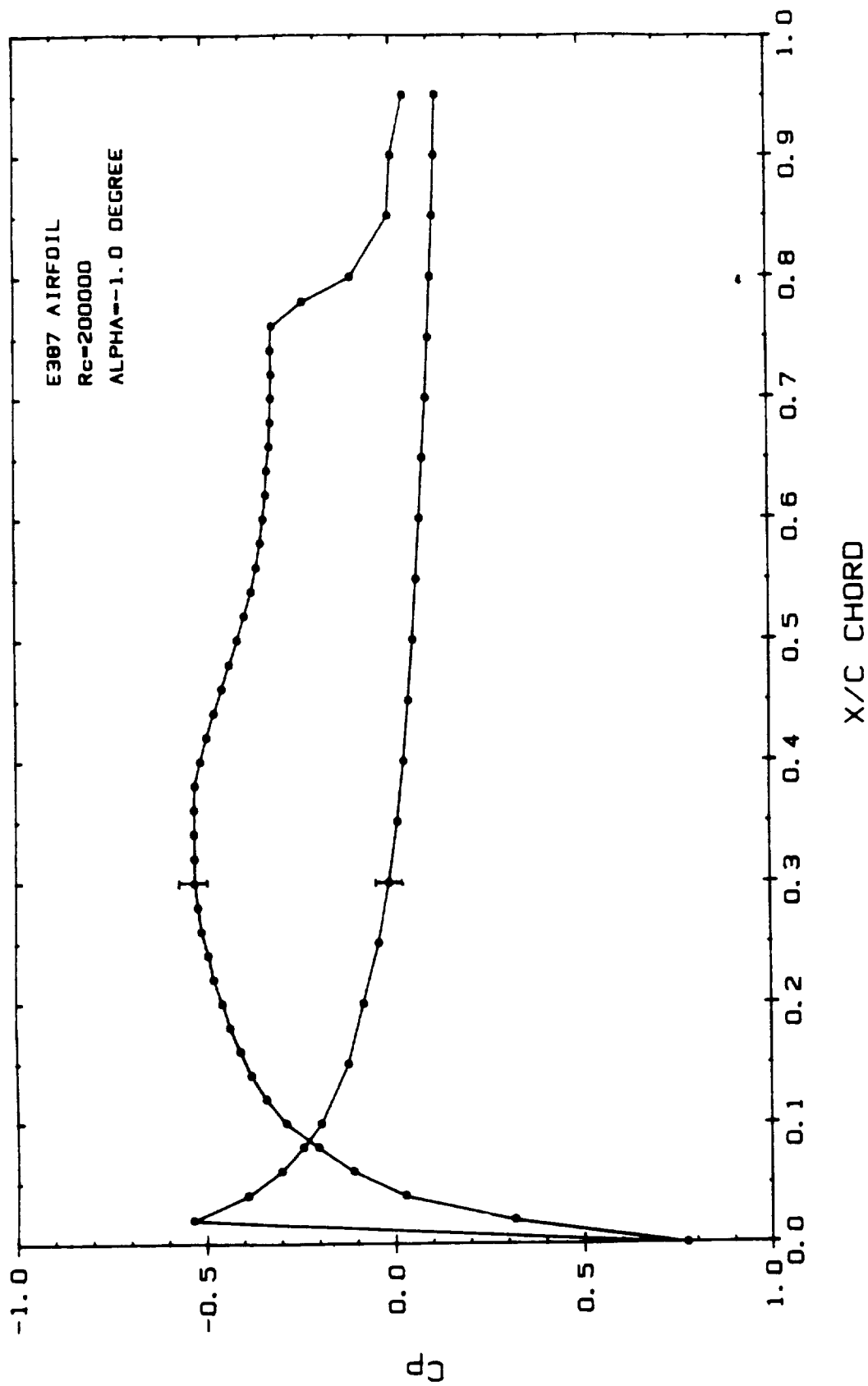
Figure 4.21   Static Pressure Distribution for E387 Airfoil
R_c = 200,000 , α = -1.0°

E387 AIRFOIL
Rc=200,000
ALPHA=0.0 DEGREES

X/C CHORD
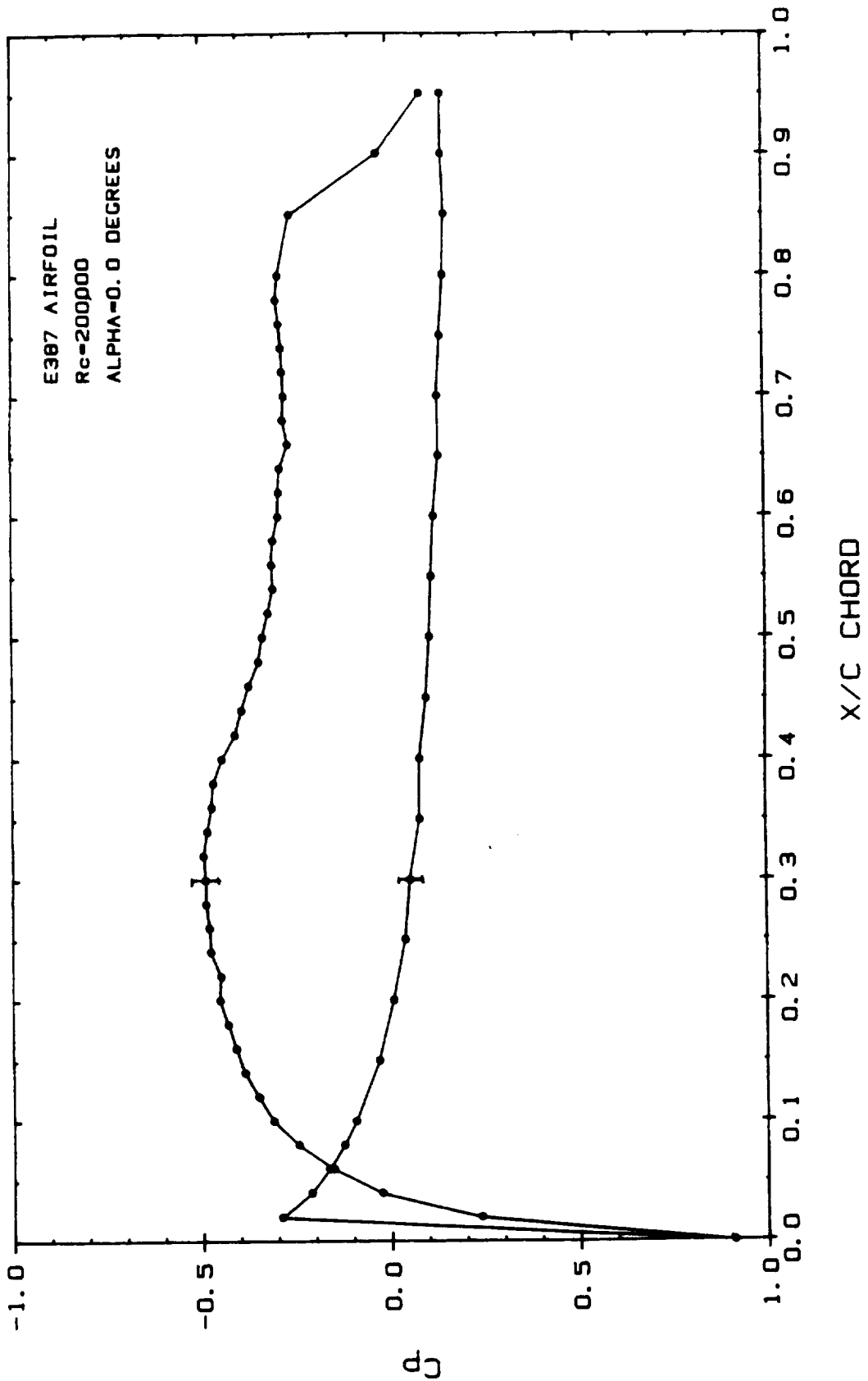
Figure 4.22 Static Pressure Distribution for E387 Airfoil
$R_c = 200,000$, $\alpha = 0.0°$
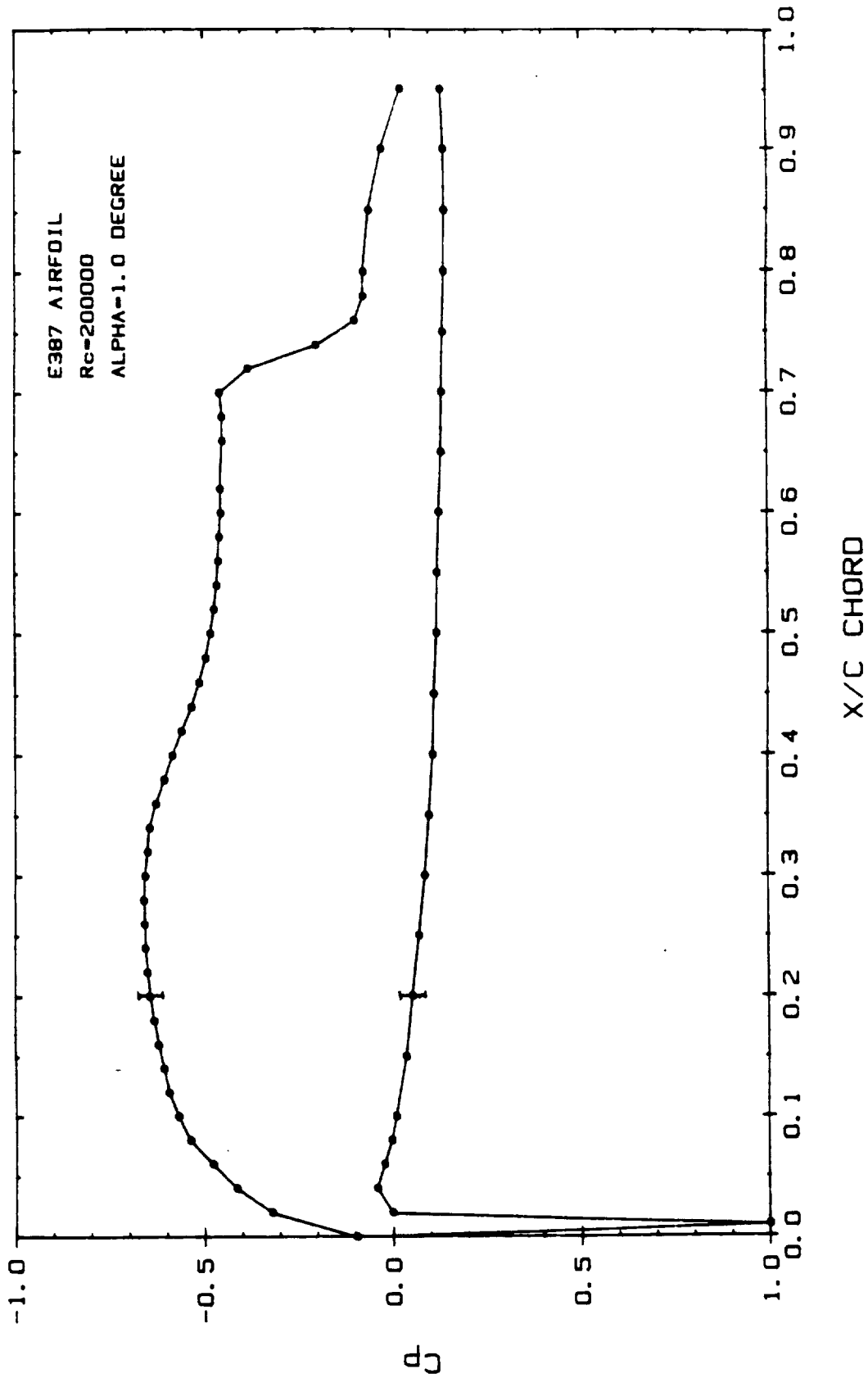
Figure 4.23 Static Pressure Distribution for E387 Airfoil
R_c = 200,000 , α = 1.0°

E387 AIRFOIL
Rc=200000
ALPHA=3.0 DEGREES

X/C CHORD
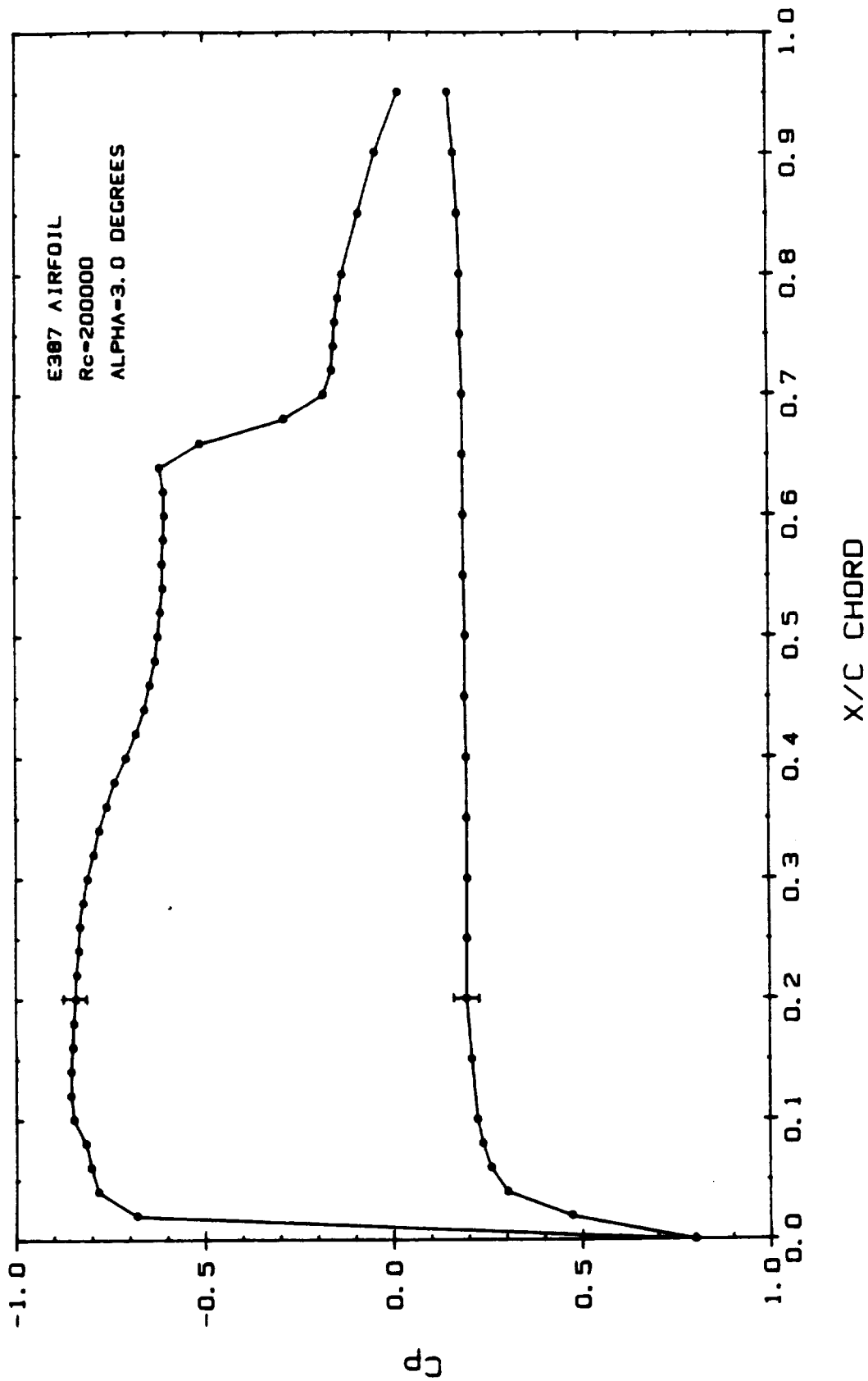
Figure 4.24 Static Pressure Distribution for E387 Airfoil
$R_c = 200,000$, $\alpha = 3.0°$

E387 AIRFOIL
Rc=200000
ALPHA=7.0 DEGREES

X/C CHORD

Cp
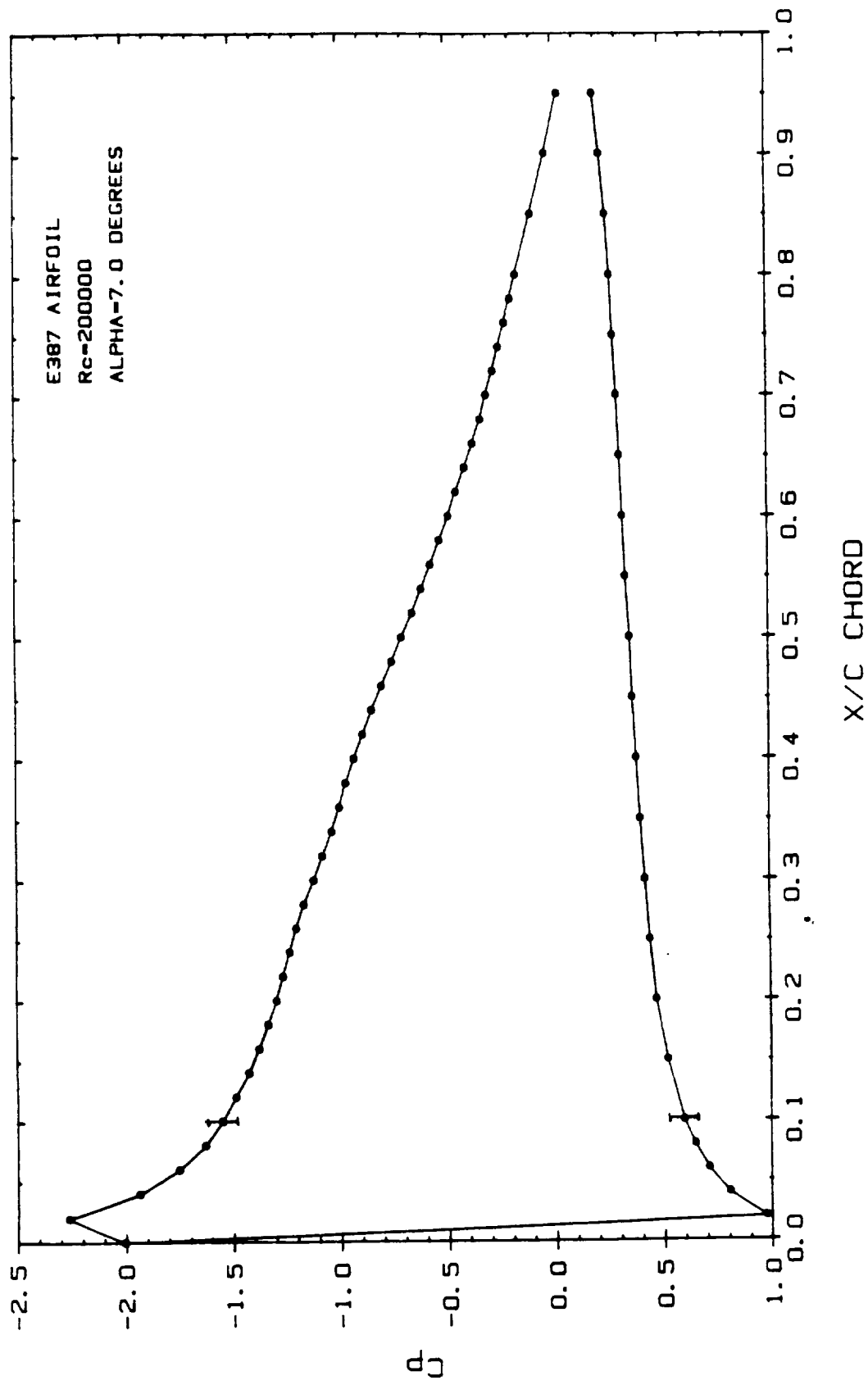
Figure 4.25   Static Pressure Distribution for E387 Airfoil
$R_c = 200,000$, $\alpha = 7.0°$

E387 AIRFOIL
Rc=200000
ALPHA=8.0 DEGREES

C_p

X/C CHORD
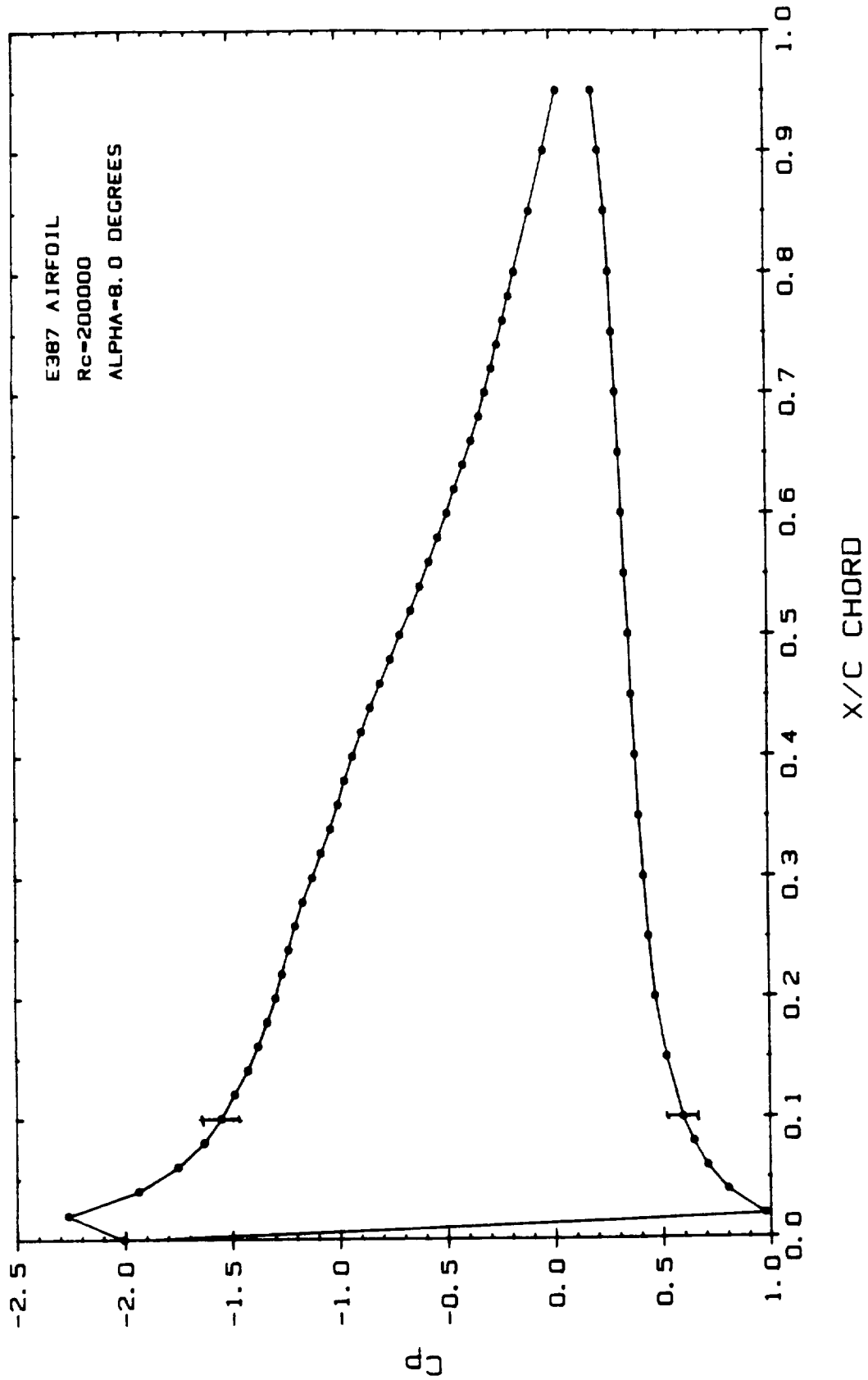
Figure 4.26 Static Pressure Distribution for E387 Airfoil
R_c = 200,000 , α = 8.0°

E387 AIRFOIL
Rc=200000
ALPHA=9.0 DEGREES

X/C CHORD
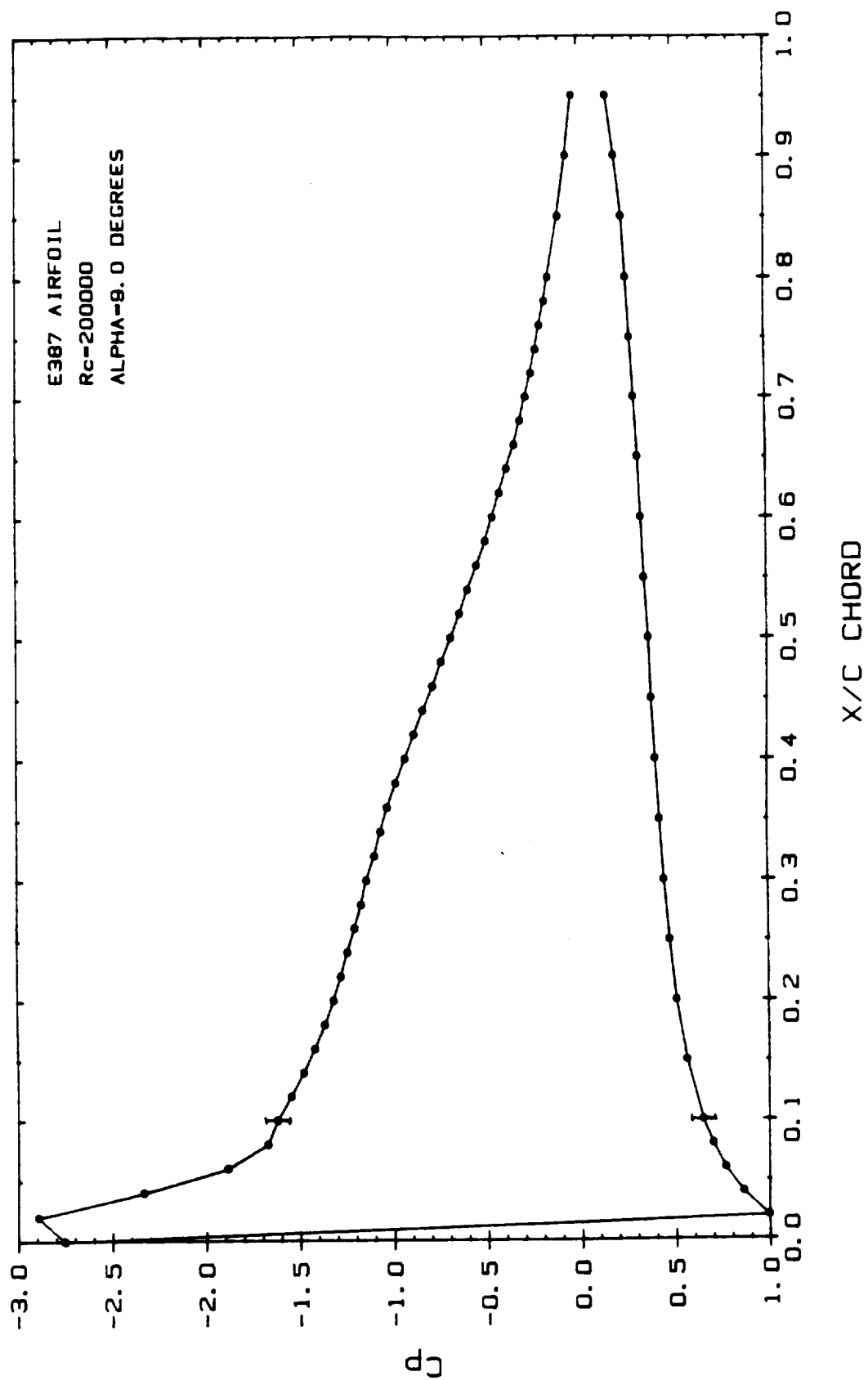
Figure 4.27   Static Pressure Distribution for E387 Airfoil
$R_c = 200,000$, $\alpha = 9.0°$

E387 AIRFOIL
Rc=200000
ALPHA=10.0 DEGREES

X/C CHORD

Cp
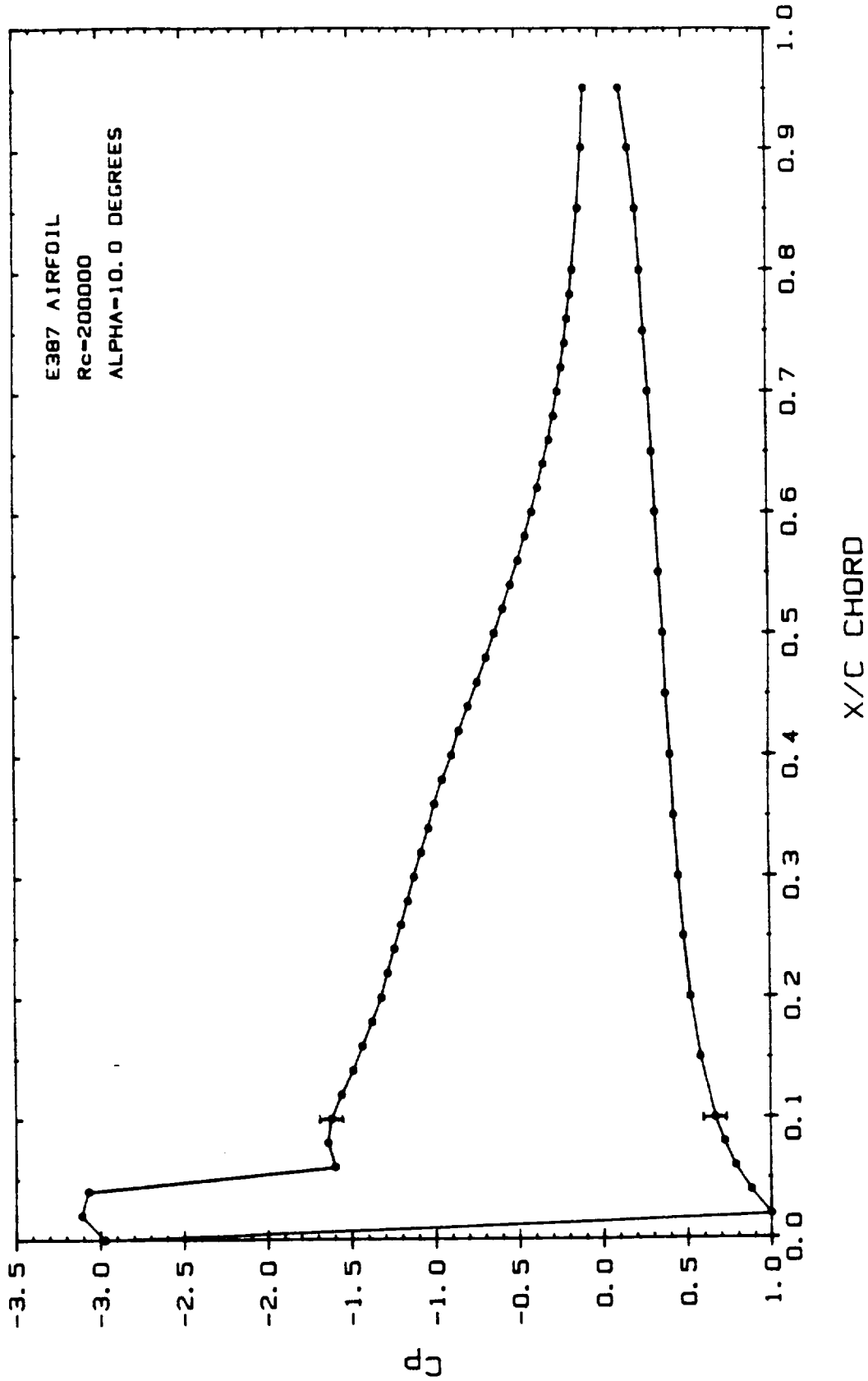
Figure 4.28   Static Pressure Distribution for E387 Airfoil
$R_c = 200,000$, $\alpha = 10.0°$

E387 AIRFOIL
Rc=300000
ALPHA=-2.0 DEGREES

X/C CHORD

CP
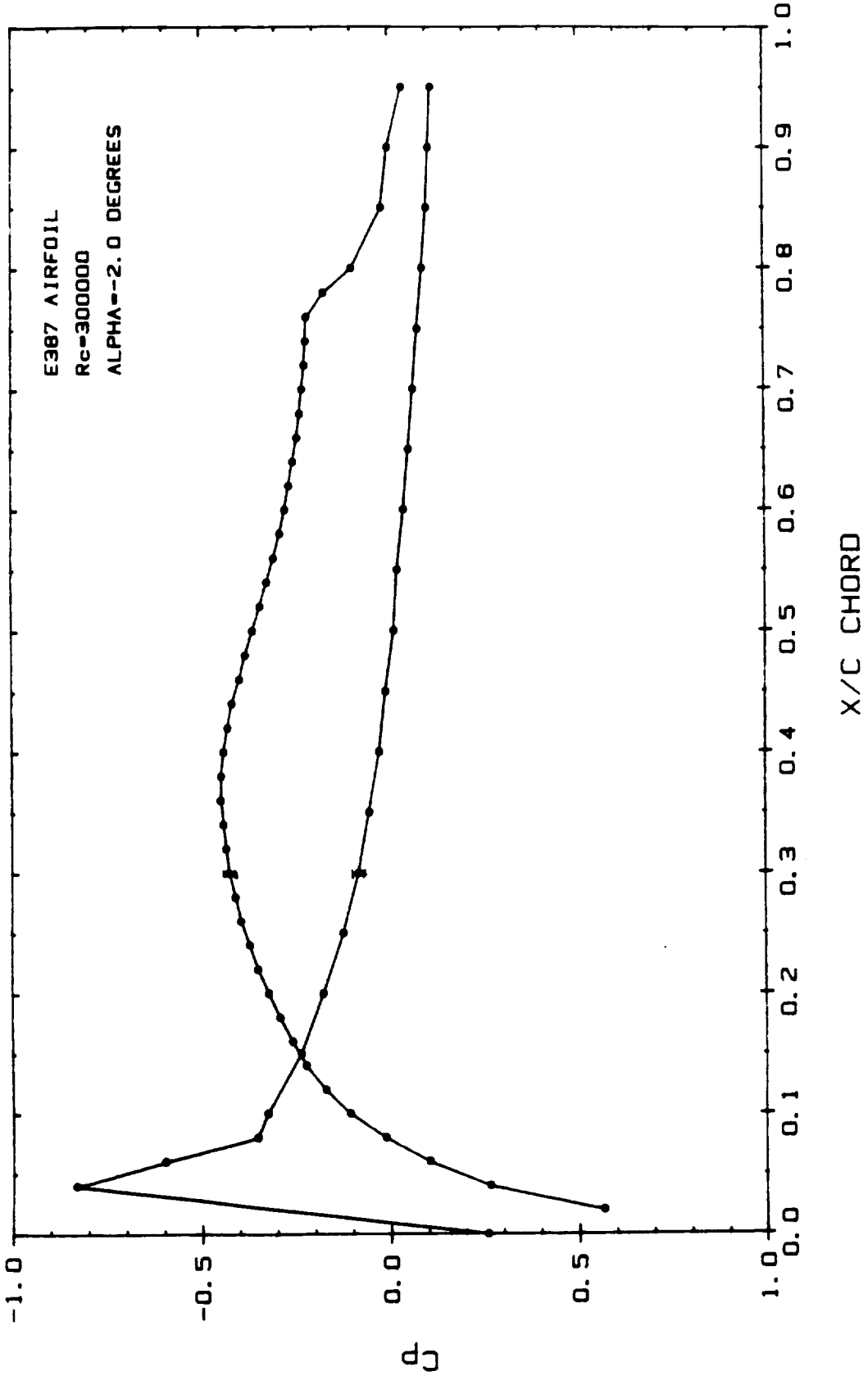
Figure 4.29   Static Pressure Distribution for E387 Airfoil
$R_c = 300,000$, $\alpha = -2.0°$

E387 AIRFOIL
Rc=300000
ALPHA=-1.0 DEGREE

X/C CHORD

Cp
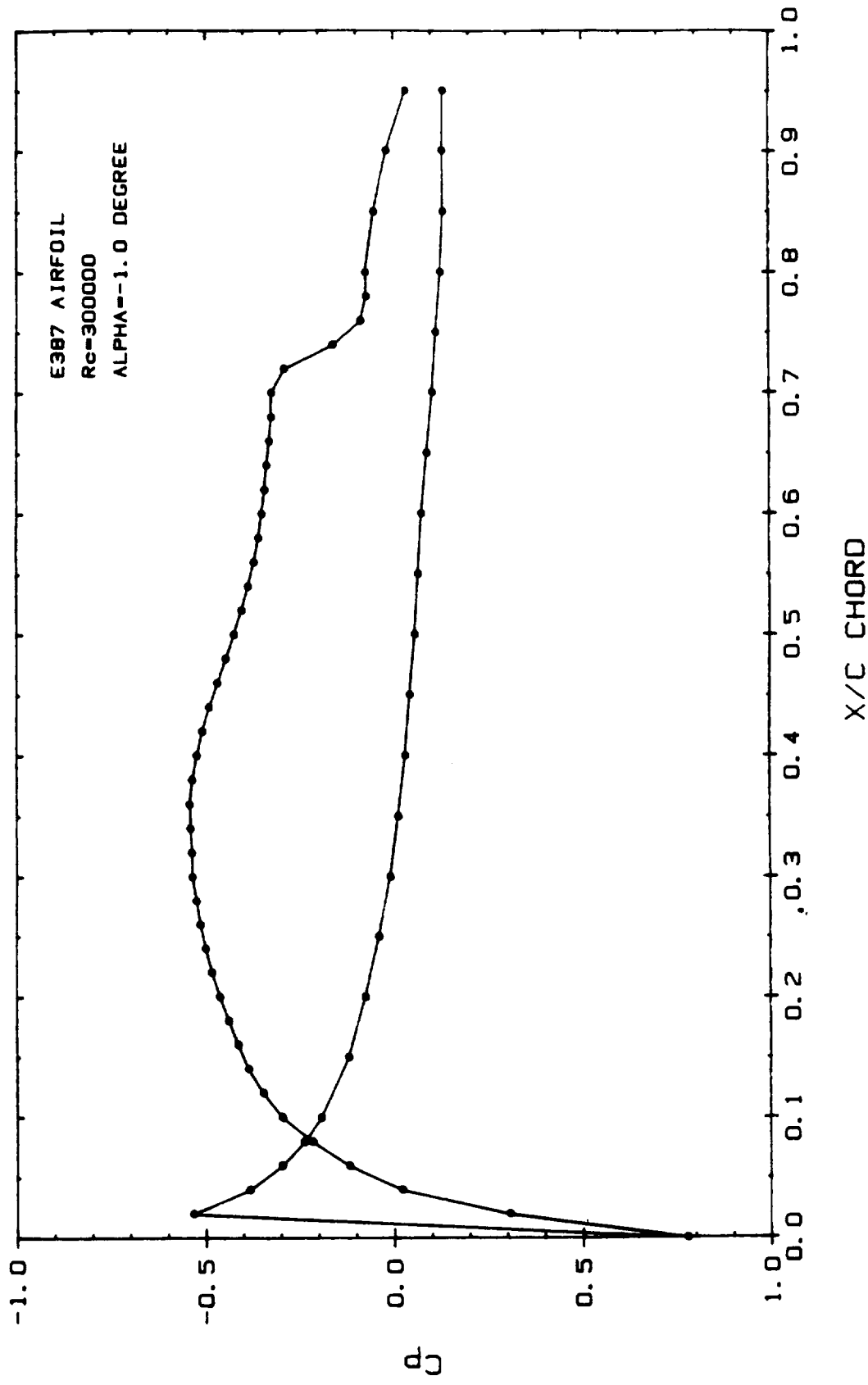
Figure 4.30   Static Pressure Distribution for E387 Airfoil
$R_c = 300,000$, $\alpha = -1.0°$
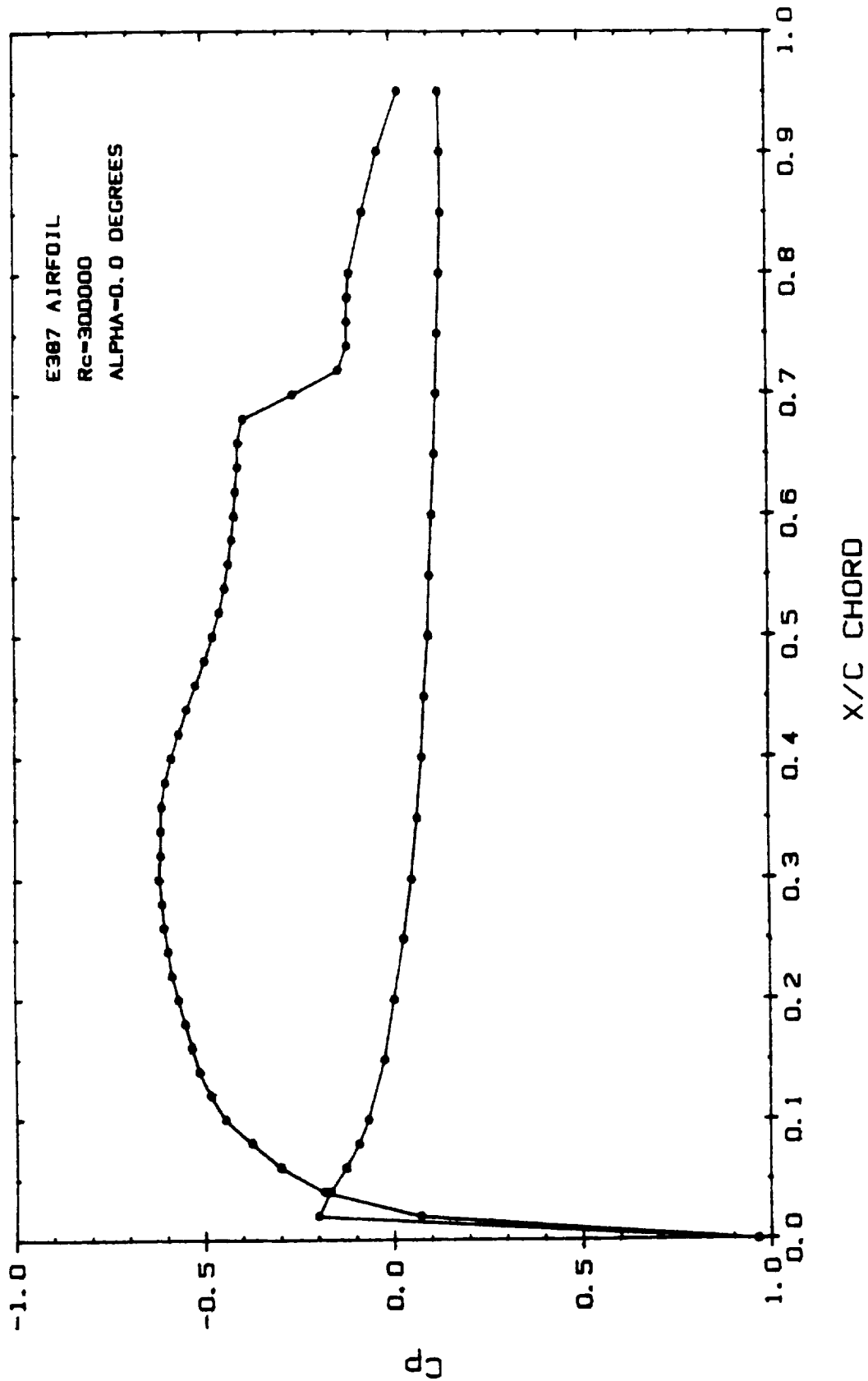
Figure 4.31   Static Pressure Distribution for E387 Airfoil
$R_c = 300,000$, $\alpha = 0.0°$
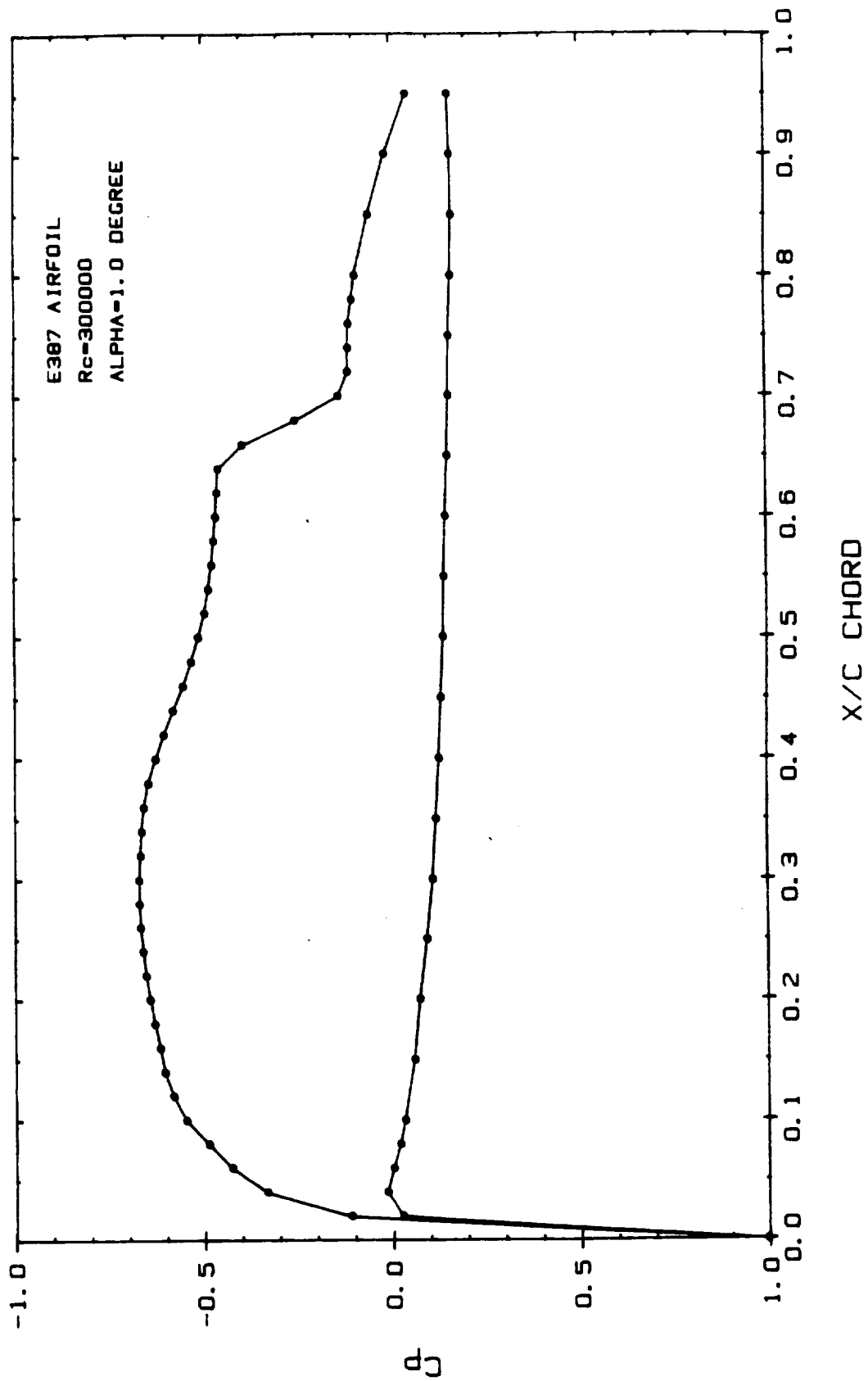
Figure 4.32   Static Pressure Distribution for E387 Airfoil
$R_c = 300,000$, $\alpha = 1.0°$

E387 AIRFOIL
Rc=300000
ALPHA=3.0 DEGREES

X/C CHORD

CP

Figure 4.33 Static Pressure Distribution for E387 Airfoil
$R_c = 300,000$, $\alpha = 3.0°$

Figure 4.34   Static Pressure Distribution for E387 Airfoil
$R_c = 300,000$, $\alpha = 7.0°$

X/C CHORD

Figure 4.35 Static Pressure Distribution for E387 Airfoil
R_c = 300,000 , α = 8.0°

Figure 4.36   Static Pressure Distribution for E387 Airfoil
$R_c = 300,000$, $\alpha = 10.0°$

Figure 4.37   Summary of Laminar Separation, Transition, and Turbulent
Reattachment Locations for Various Angles of Attack for the E387
Airfoil at R_c = 100,000
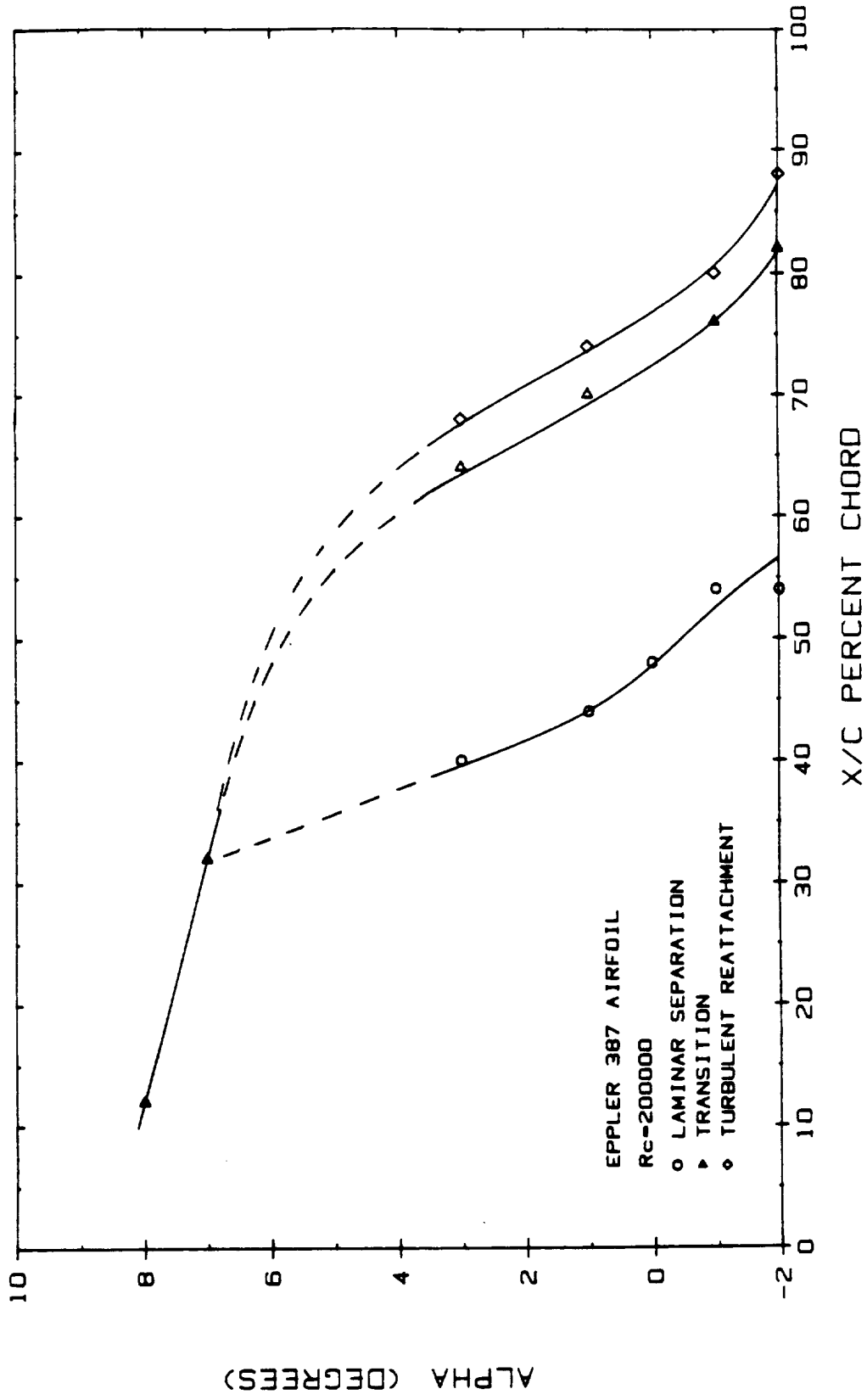
Figure 4.38 Summary of Laminar Separation, Transition, and Turbulent Reattachment Locations for Various Angles of Attack for the E387 Airfoil at R_c = 200,000
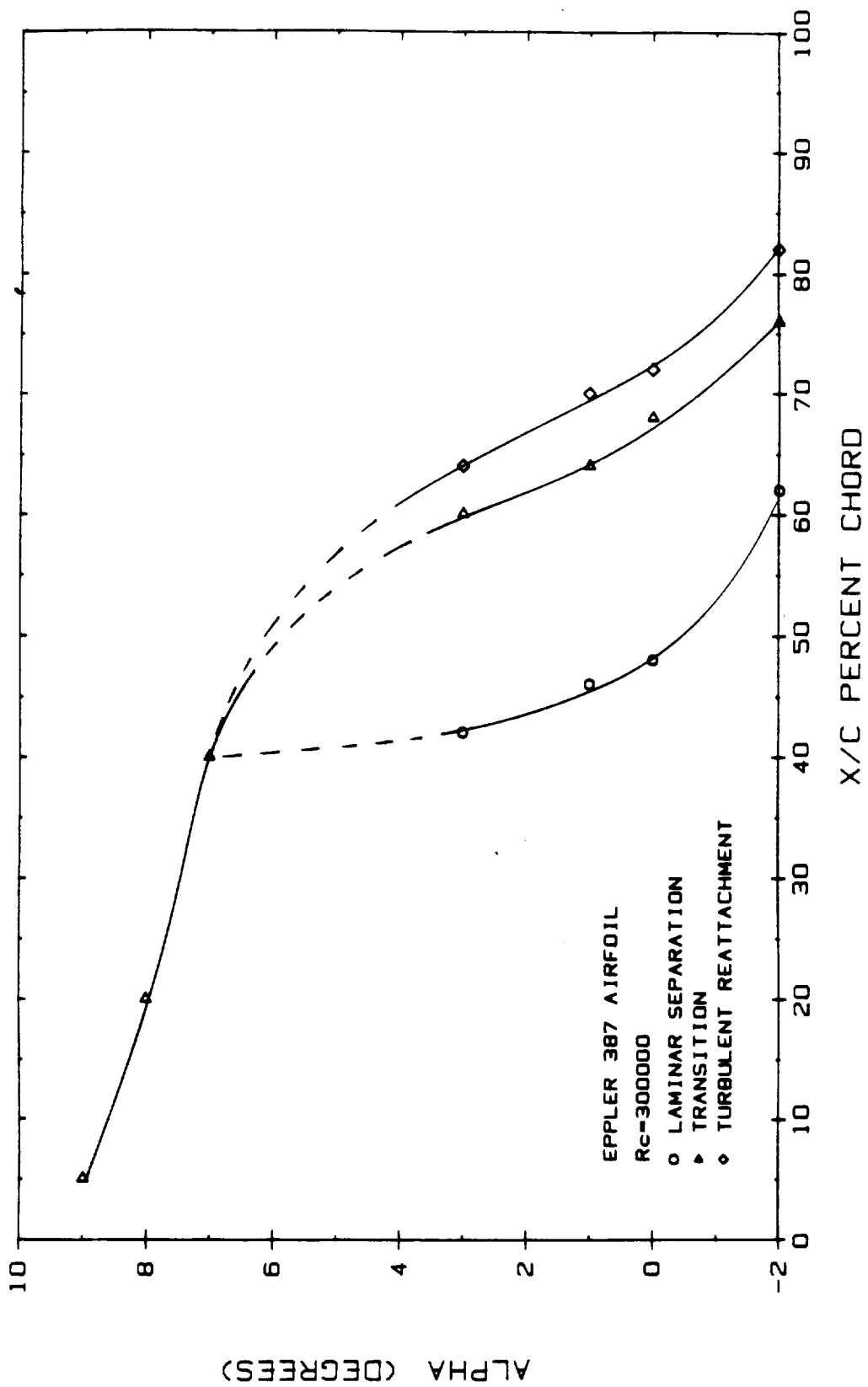
Figure 4.39 Summary of Laminar Separation, Transition, and Turbulent Reattachment Locations for Various Angles of Attack for the E387 Airfoil at R_c = 300,000
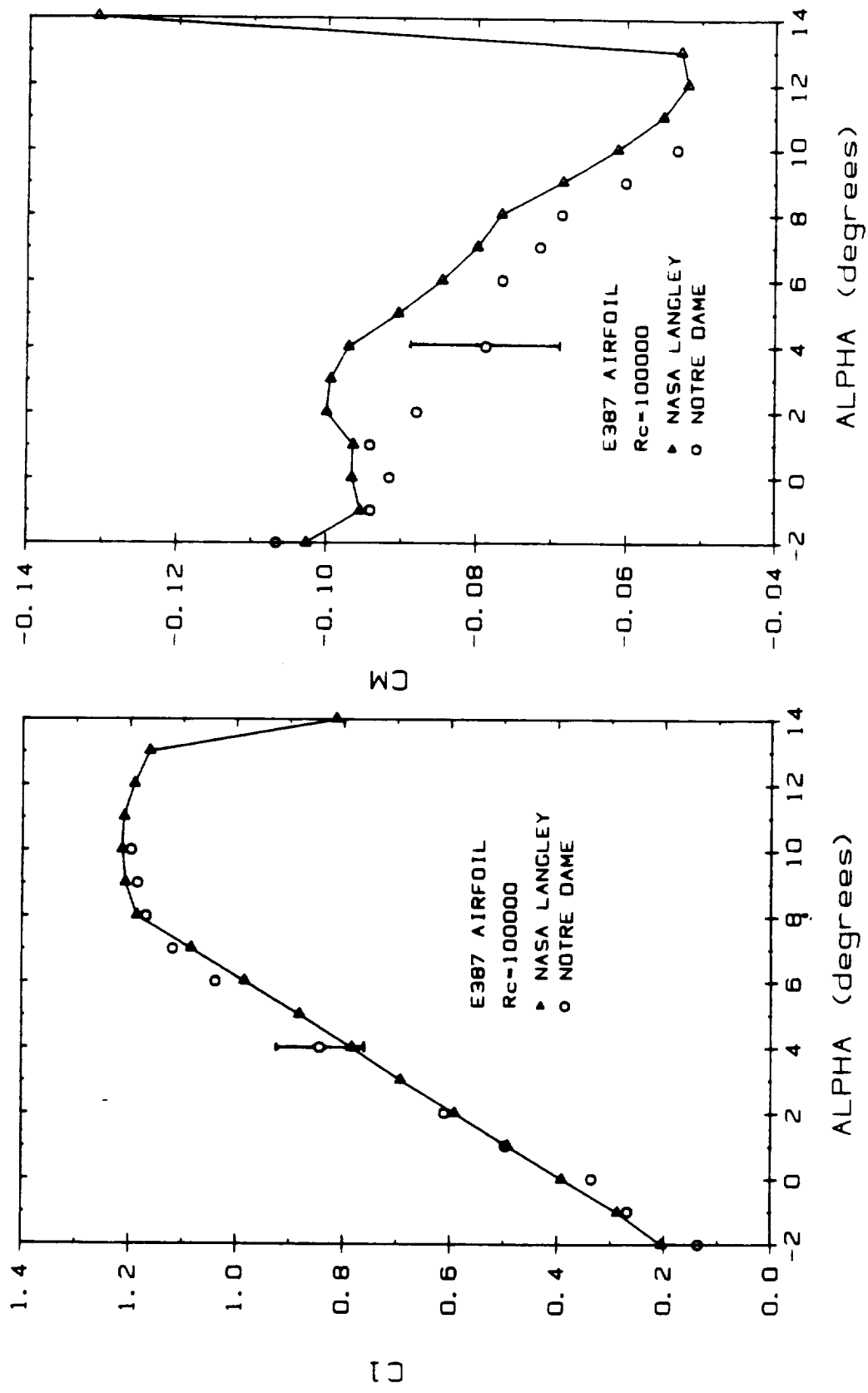
Figure 4.40 Comparison of Notre Dame and NASA Langley Lift and
Moment Curves for the E387 Airfoil at R_c = 100,000
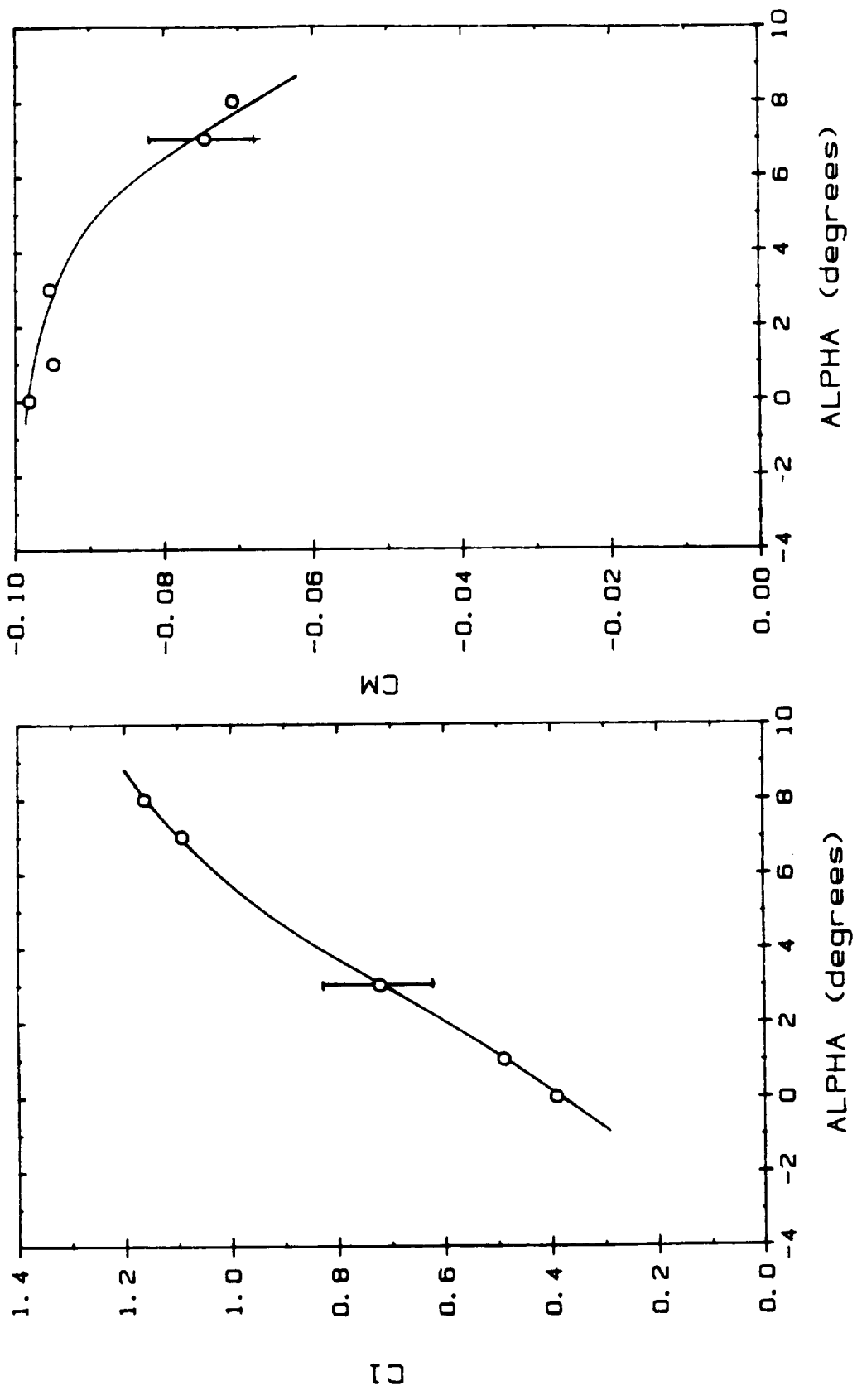
Figure 4.41 E387 Lift and Moment Curves for R_c = 75,000
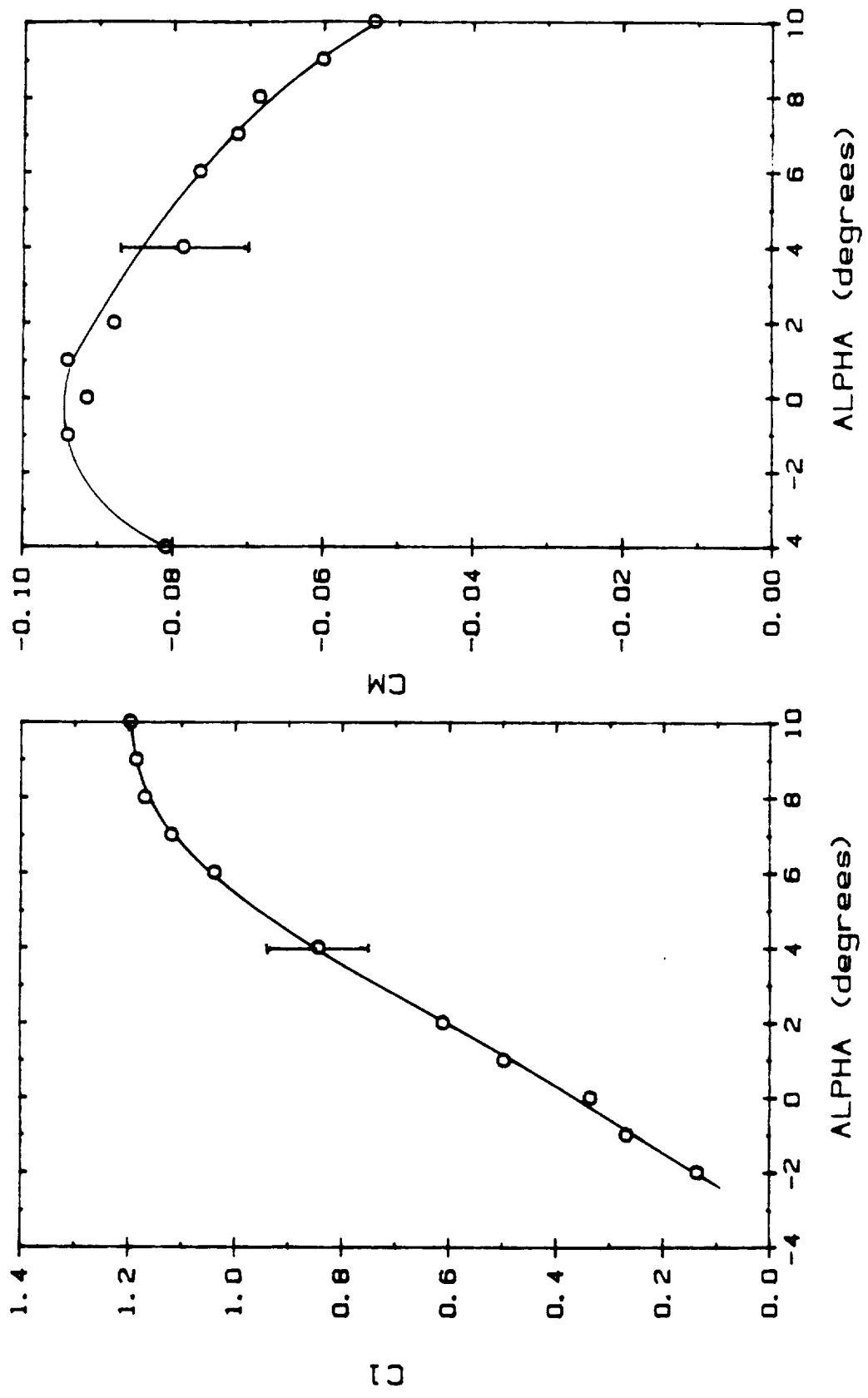
Figure 4.42 E387 Lift and Moment Curves for R_c = 100,000
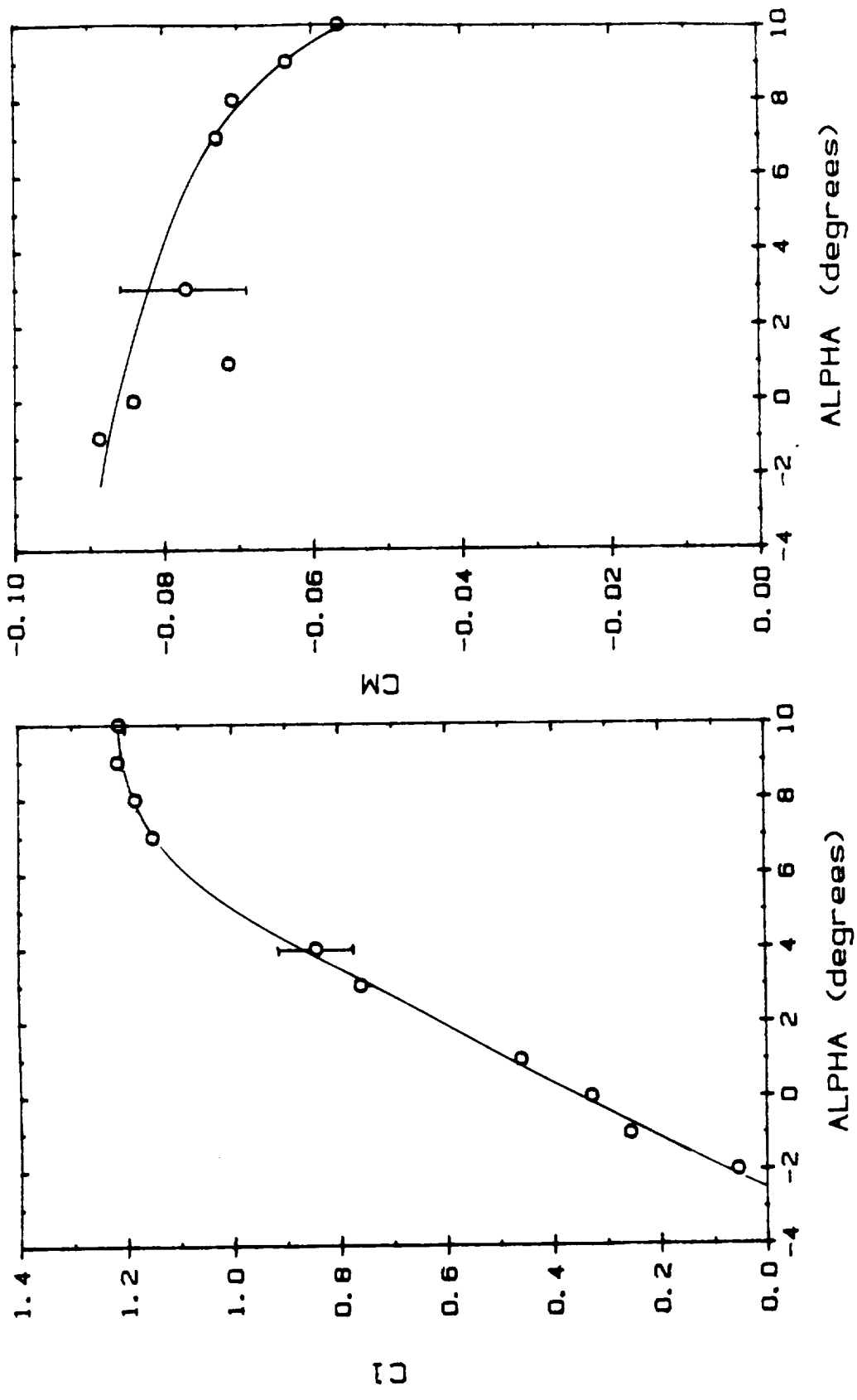
Figure 4.43   E387 Lift and Moment Curves for R_c = 200,000
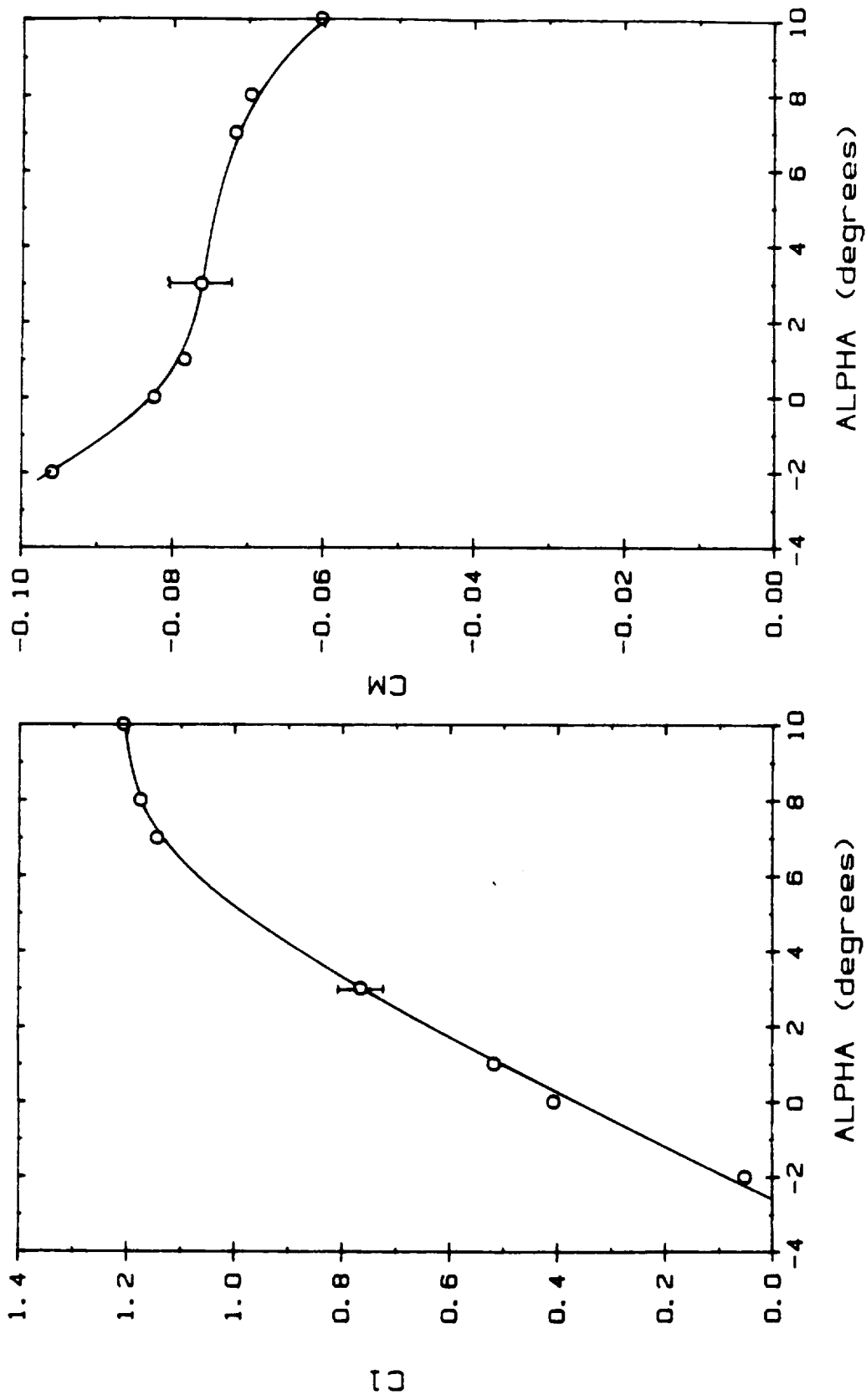
Figure 4.44 E387 Lift and Moment Curves for R_c = 300,000
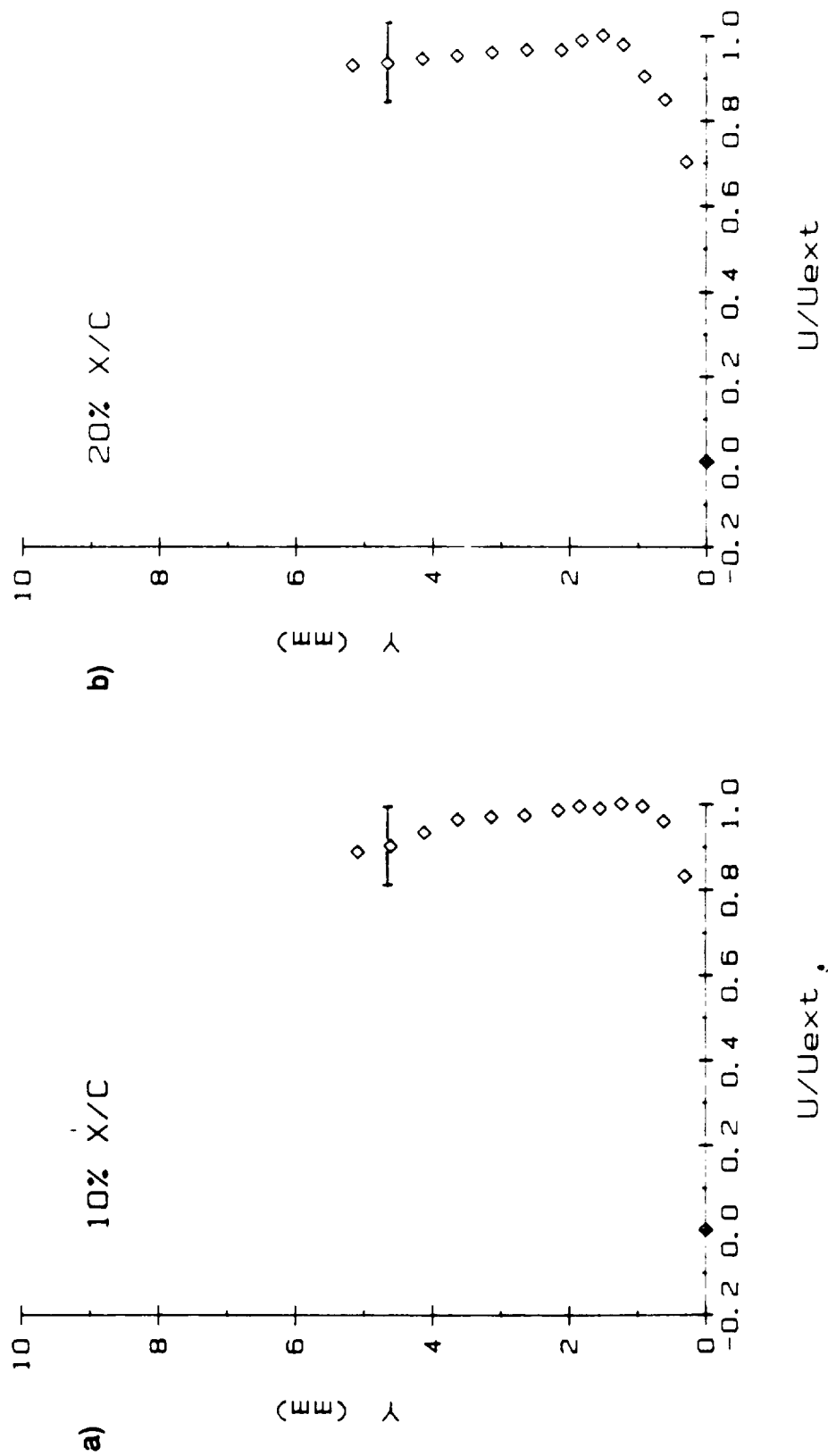
Figure 4.45 E387 Airfoil LDV U/U_{ext} Boundary Layer Velocity Profiles, 10% x/c and 20% x/c Chord Positions, R_c = 100,000 , α = 2.0°
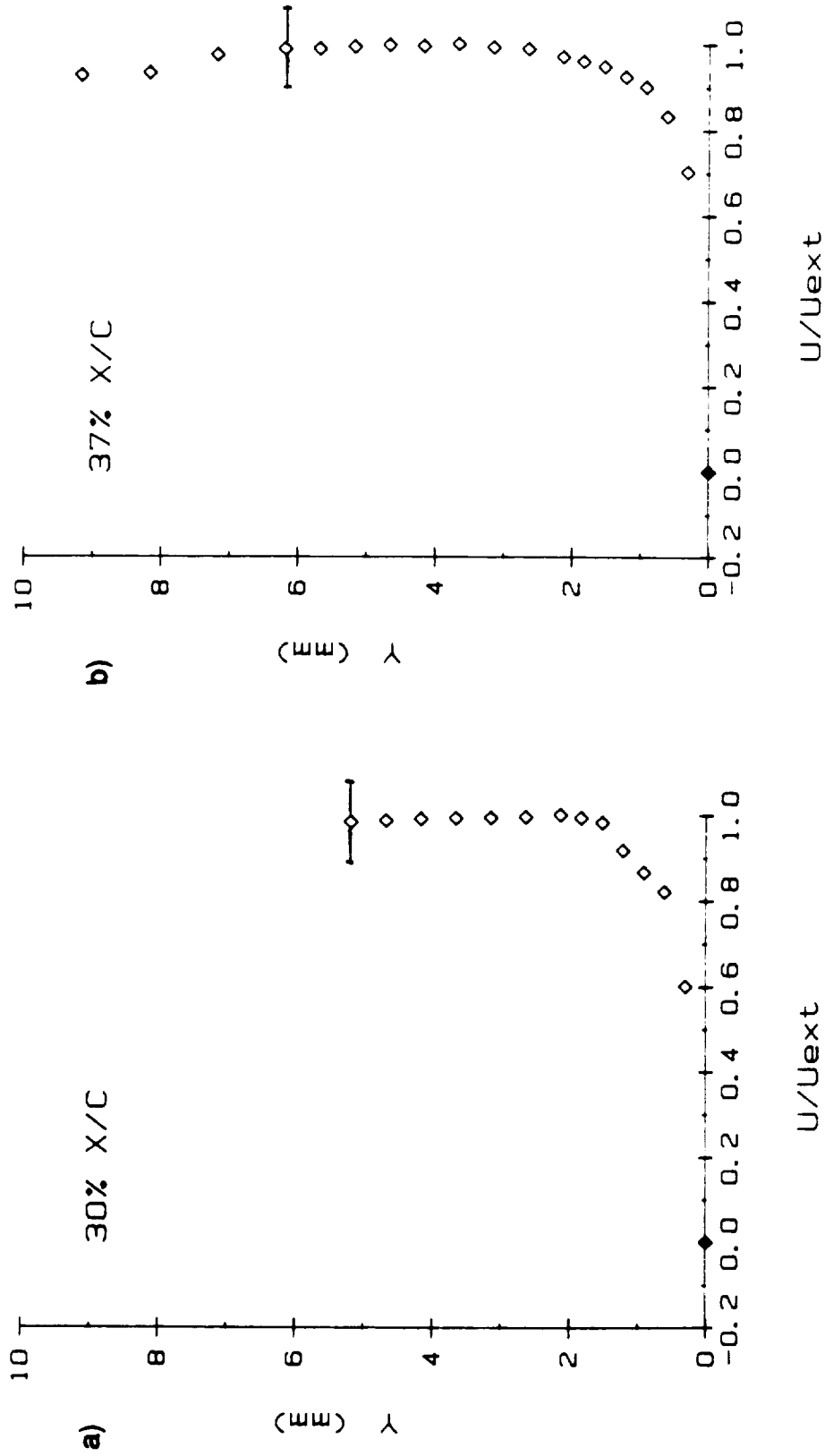
Figure 4.46 E387 Airfoil LDV U/U$_{ext}$ Boundary Layer Velocity Profiles, 30% x/c and 37% x/c Chord Positions, R$_c$ = 100,000 , α = 2.0°
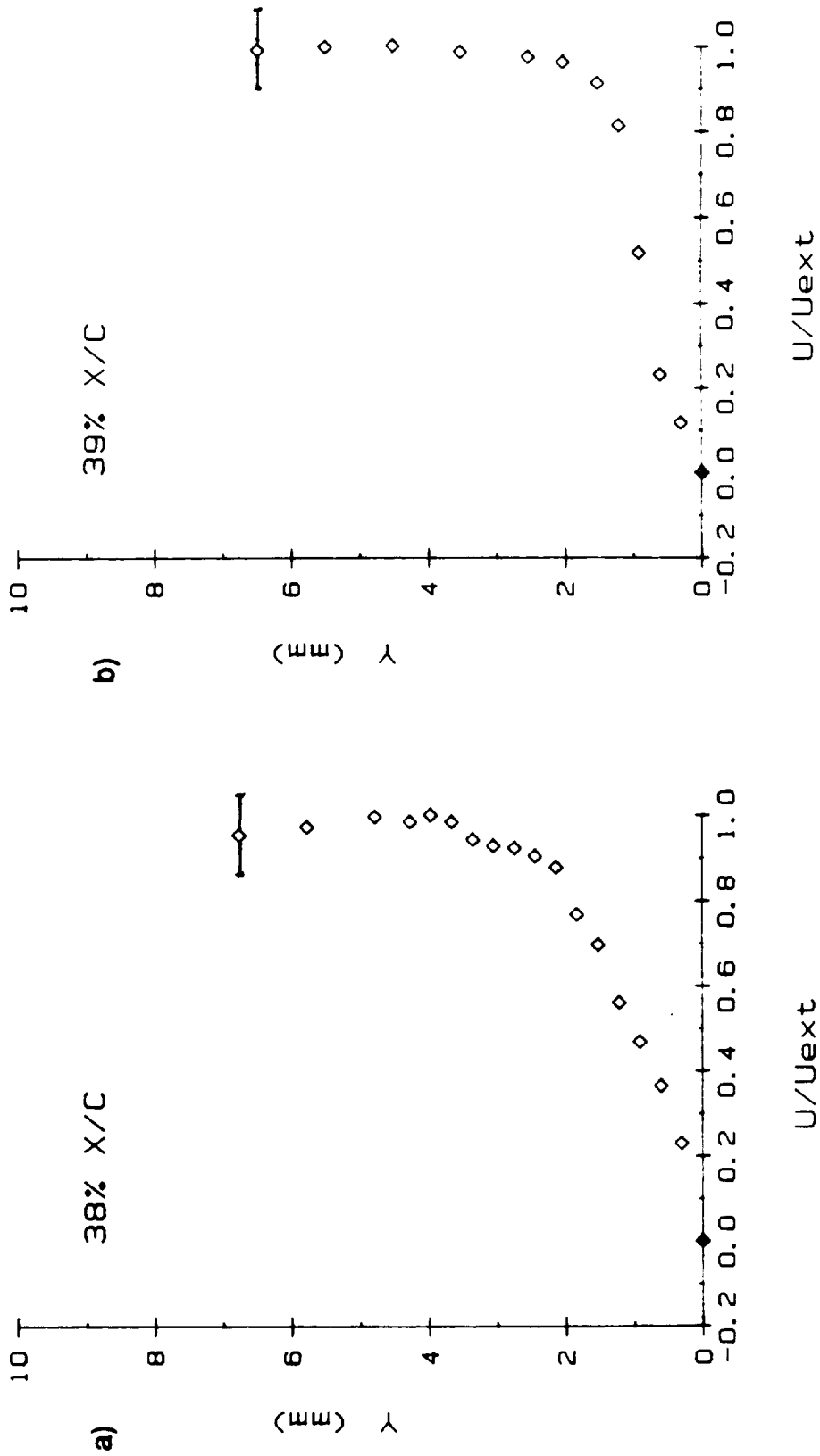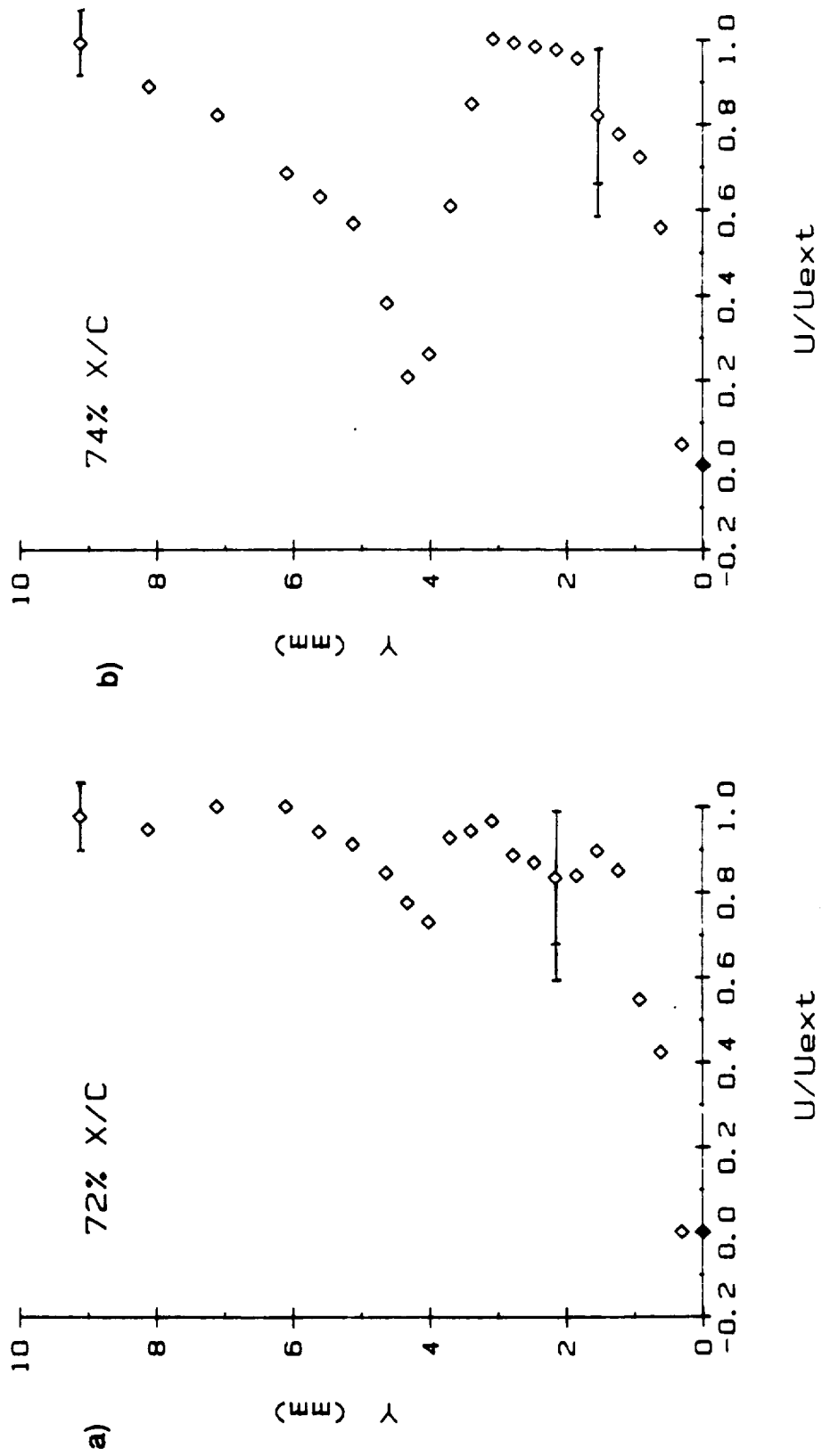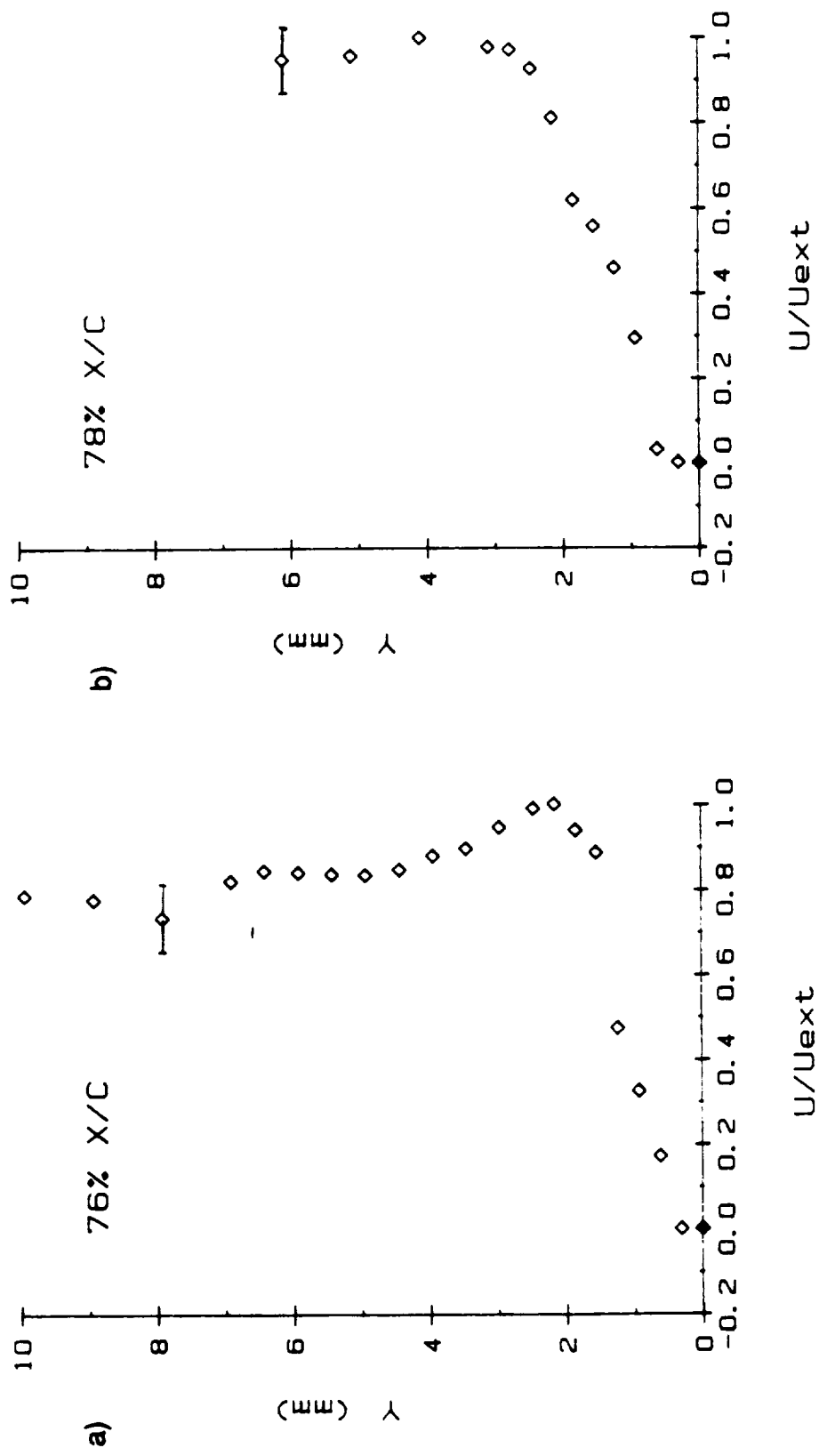
Figure 4.47 E387 Airfoil LDV U/U_{ext} Boundary Layer Velocity Profiles,
38% x/c and 39% x/c Chord Positions, R_c = 100,000 , α = 2.0°
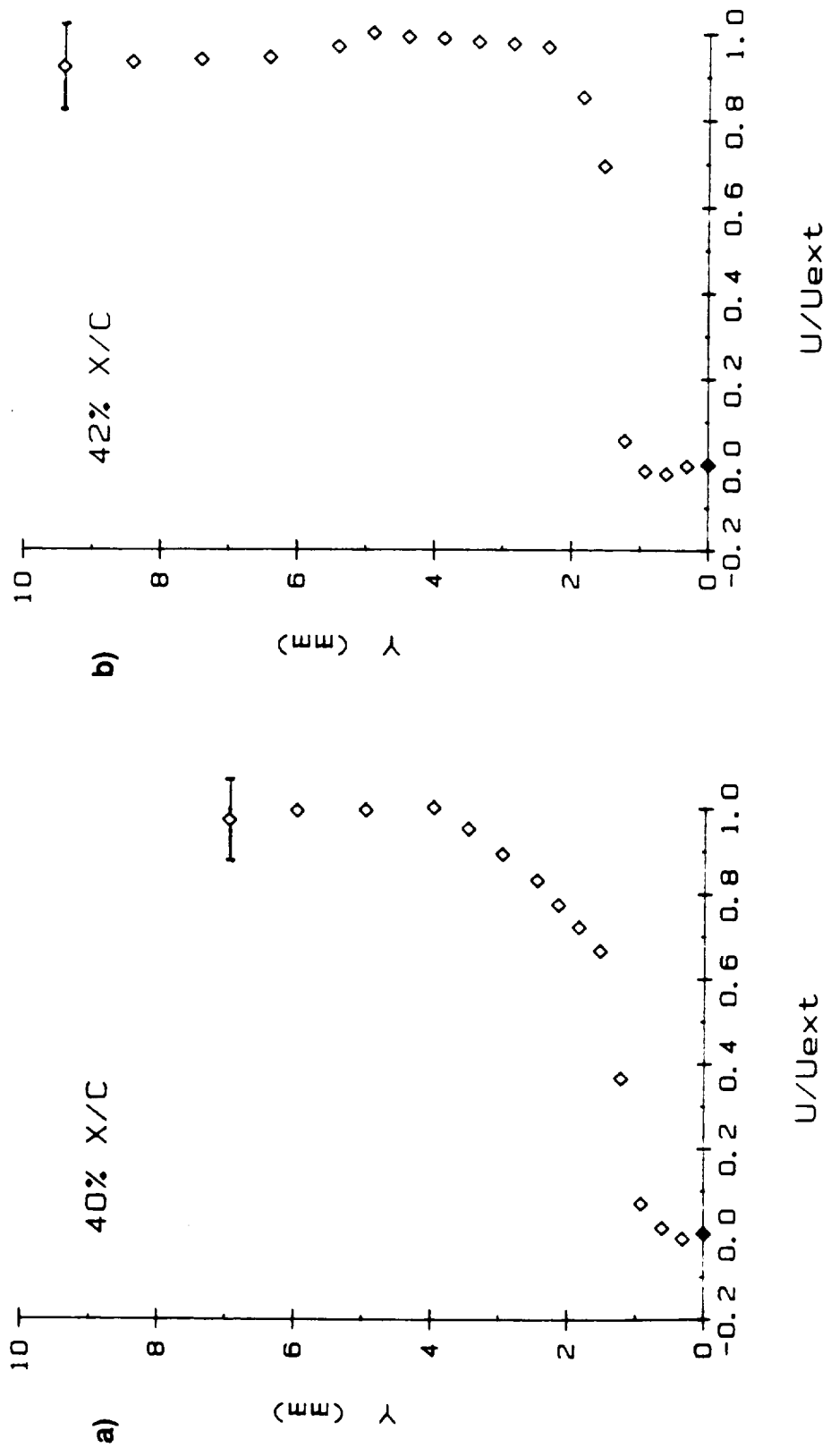
Figure 4.48   E387 Airfoil LDV U/U$_{ext}$ Boundary Layer Velocity Profiles, 40% x/c and 42% x/c Chord Positions, R$_c$ = 100,000 , α = 2.0°
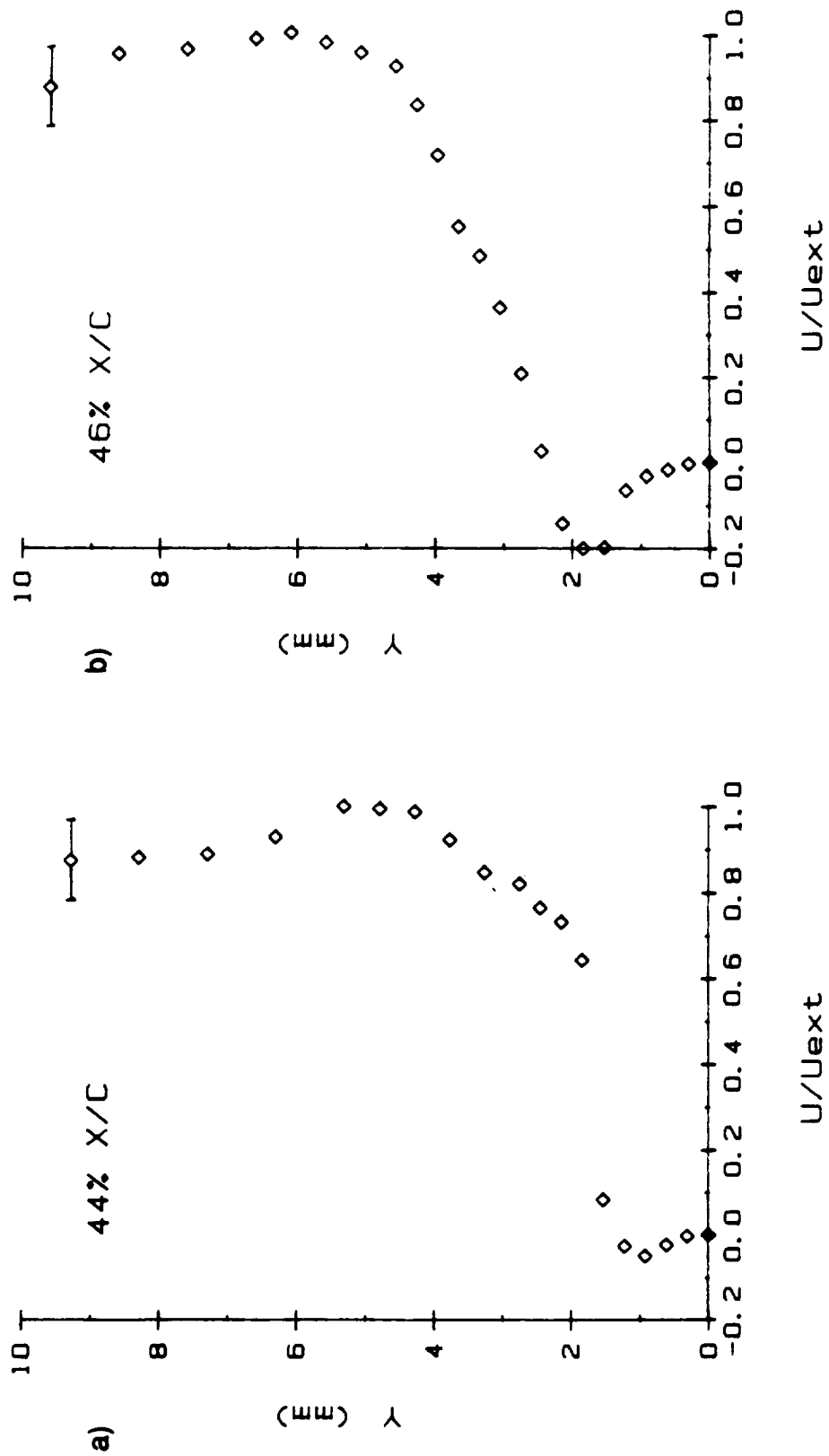
Figure 4.49 E387 Airfoil LDV U/U_{ext} Boundary Layer Velocity Profiles, 44% x/c and 46% x/c Chord Positions, $R_c = 100,000$, $\alpha = 2.0°$
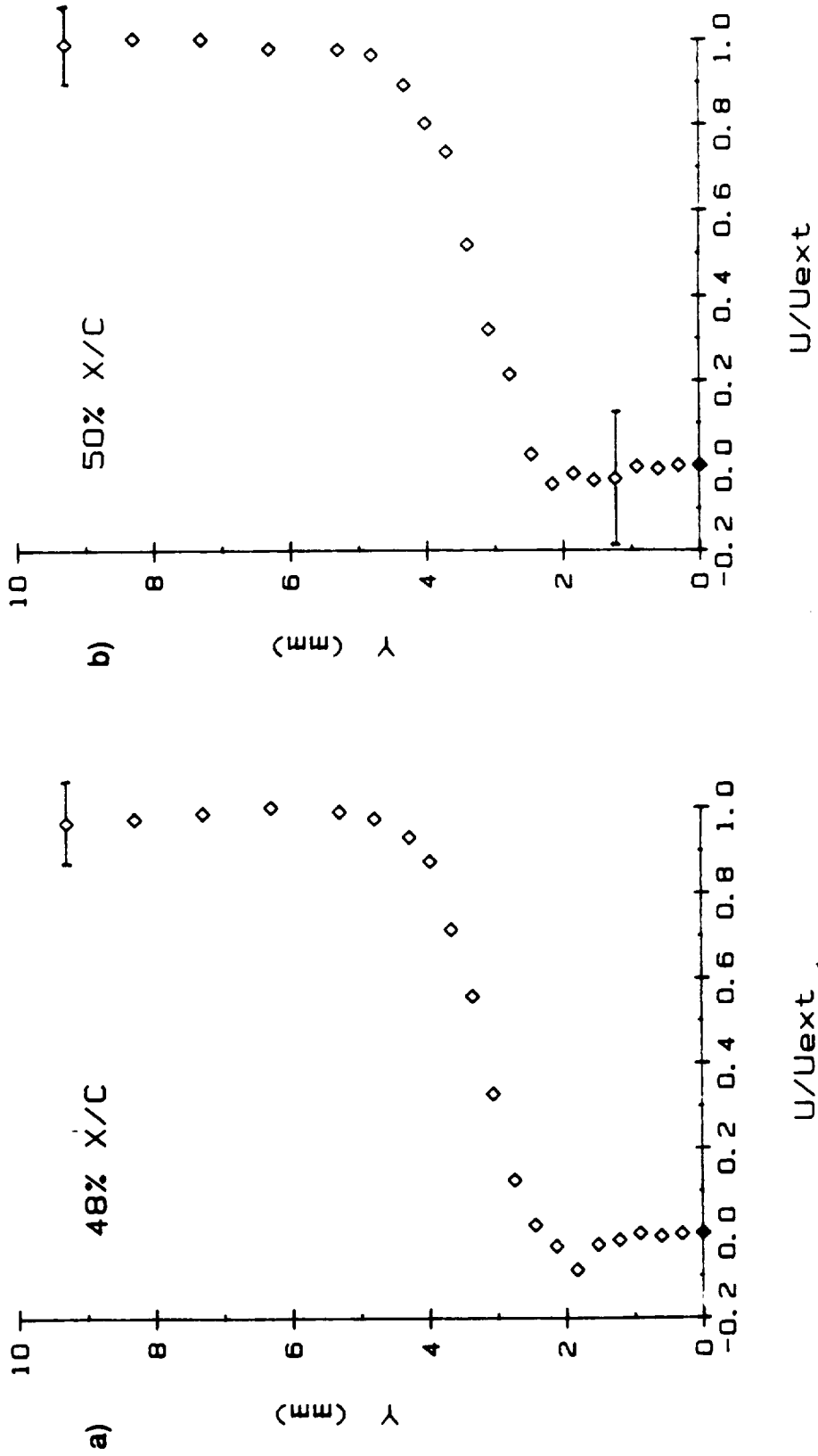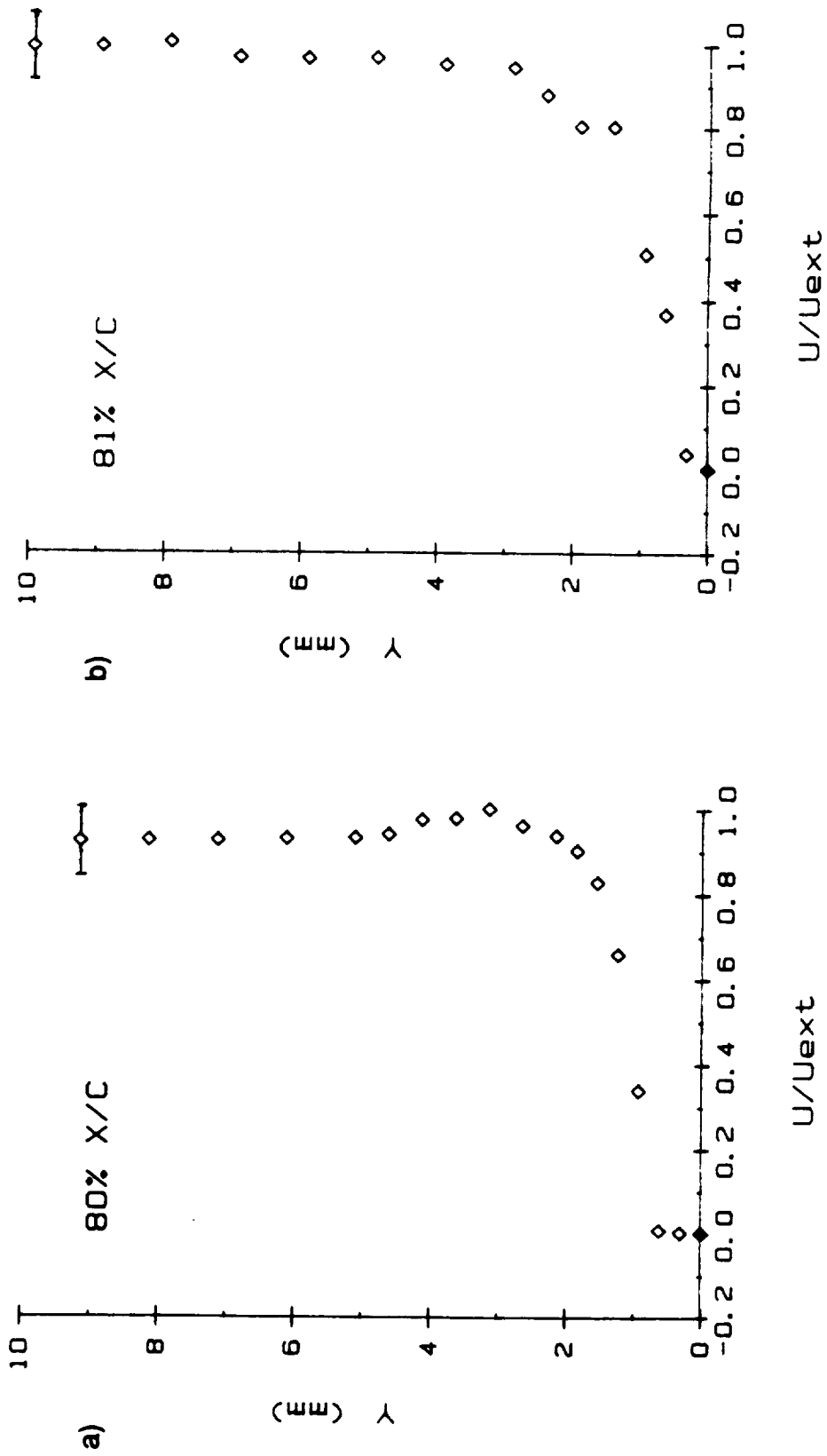
Figure 4.50   E387 Airfoil LDV U/U_{ext} Boundary Layer Velocity Profiles, 48% x/c and 50% x/c Chord Positions, $R_c = 100,000$, $\alpha = 2.0°$
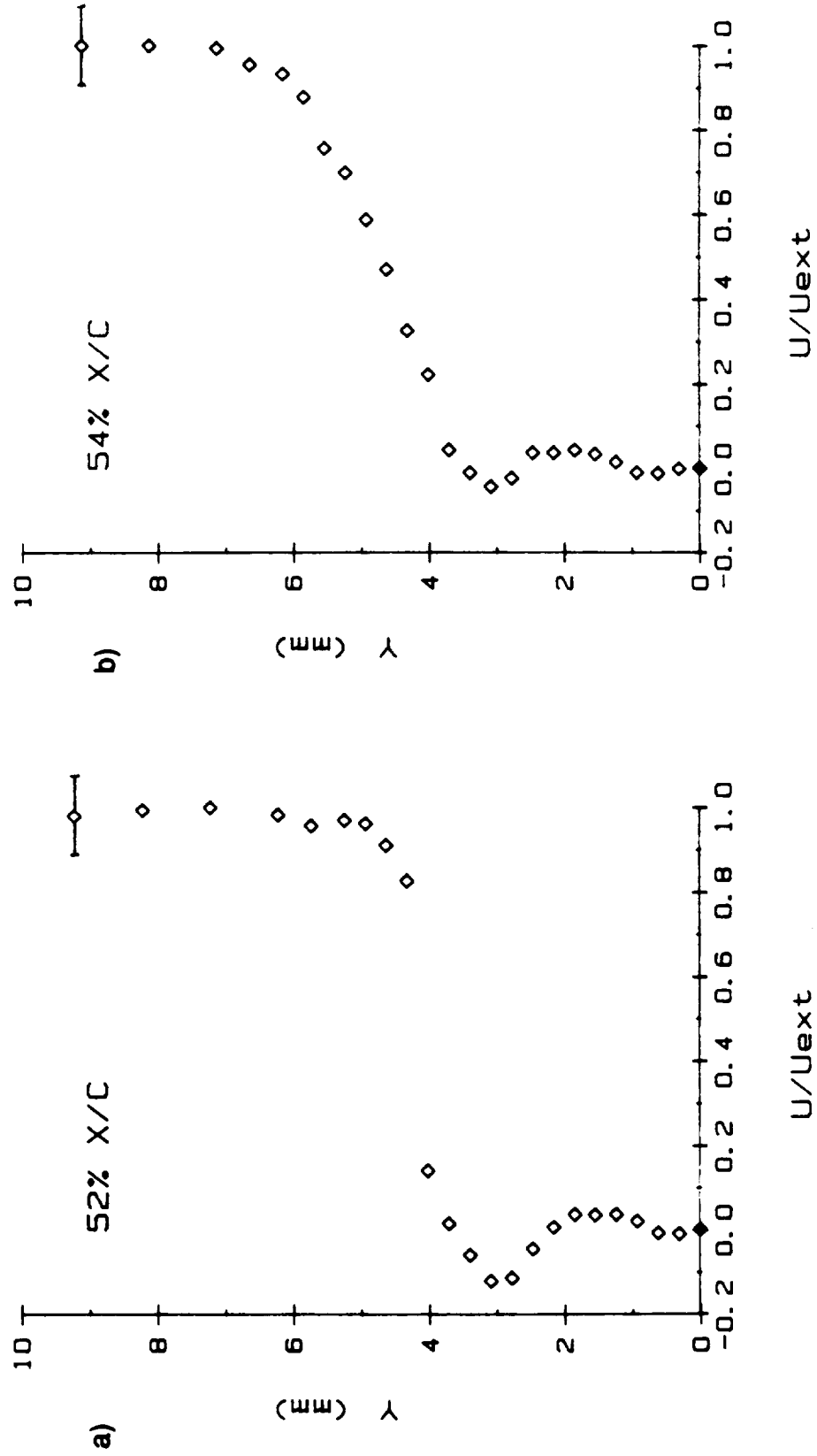
Figure 4.51 E387 Airfoil LDV U/U_{ext} Boundary Layer Velocity Profiles, 52% x/c and 54% x/c Chord Positions, R_c = 100,000 , α = 2.0°
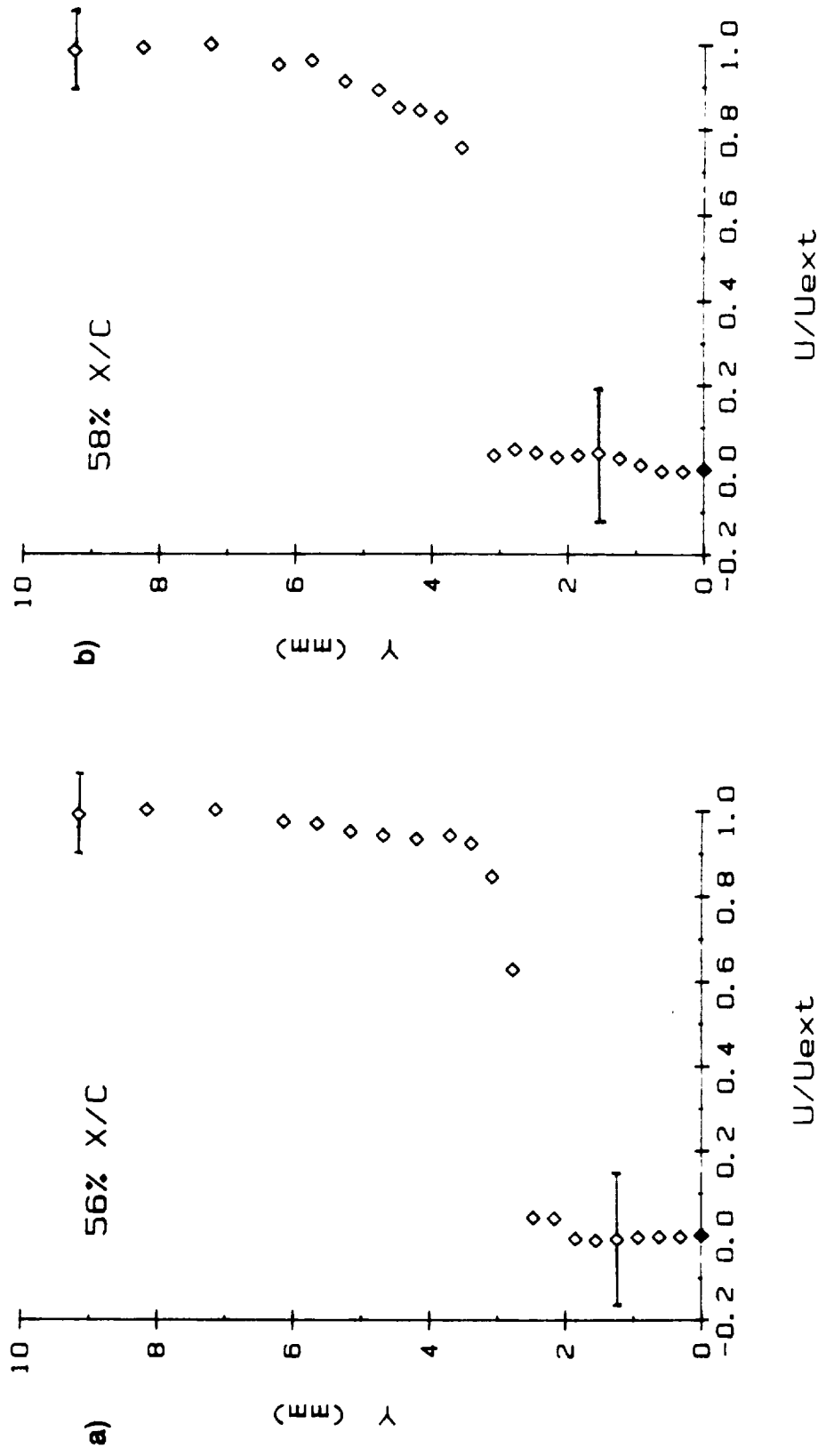
Figure 4.52 E387 Airfoil LDV U/U_{ext} Boundary Layer Velocity Profiles, 56% x/c and 58% x/c Chord Positions, $R_c = 100,000$, $\alpha = 2.0°$
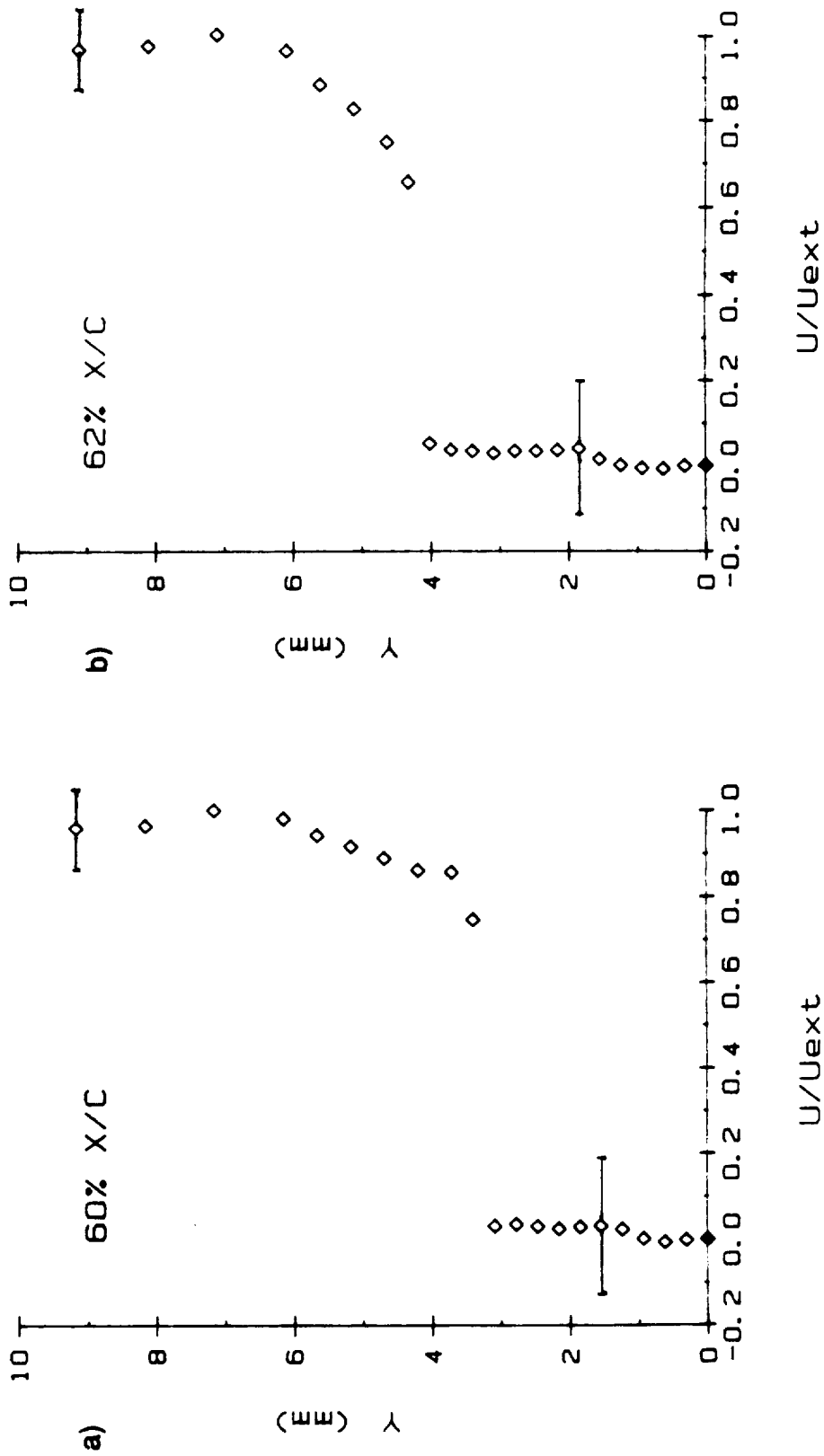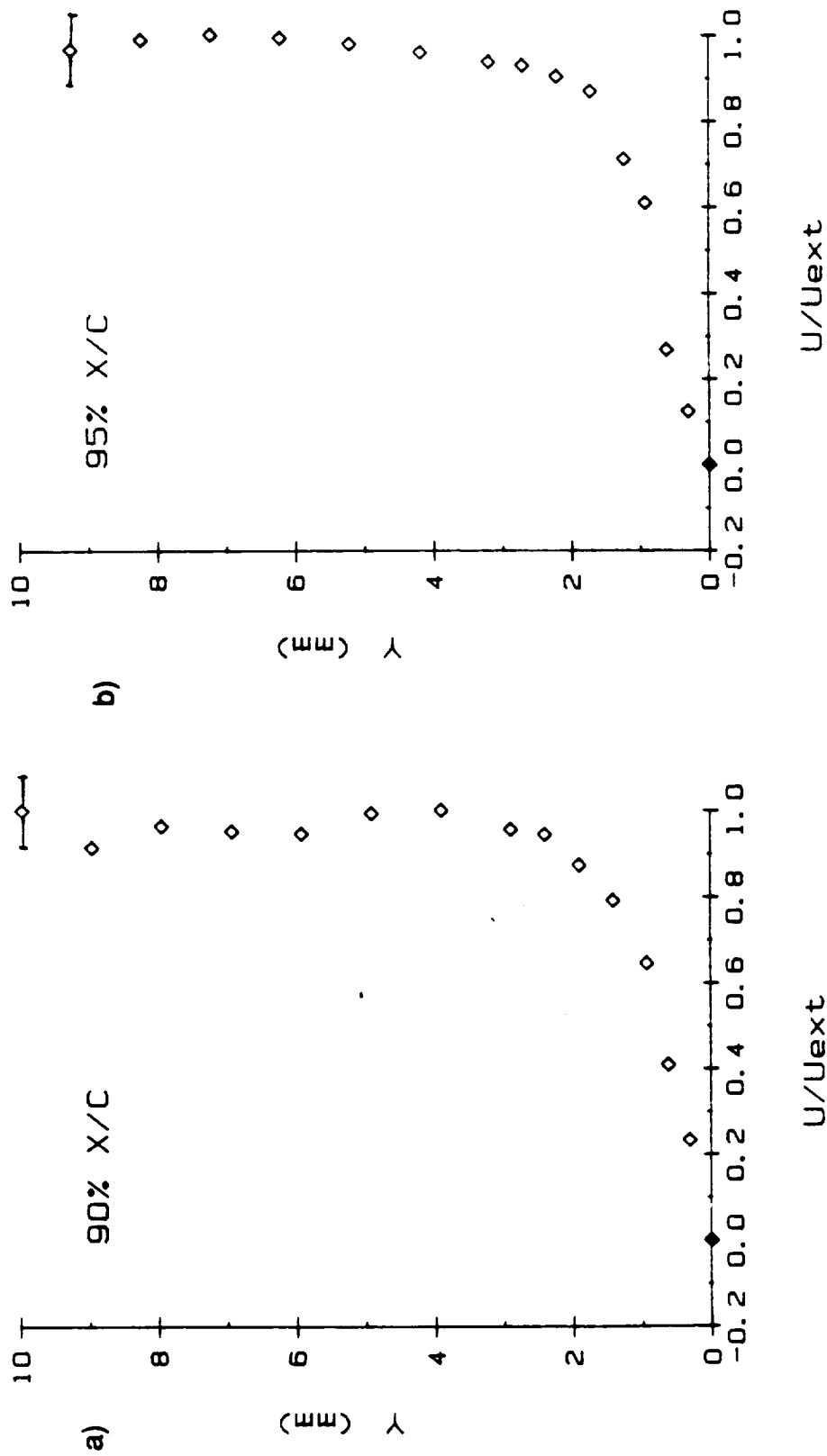
Figure 4.53 E387 Airfoil LDV U/U_{ext} Boundary Layer Velocity Profiles, 60% x/c and 62% x/c Chord Positions, R_c = 100,000 , α = 2.0°
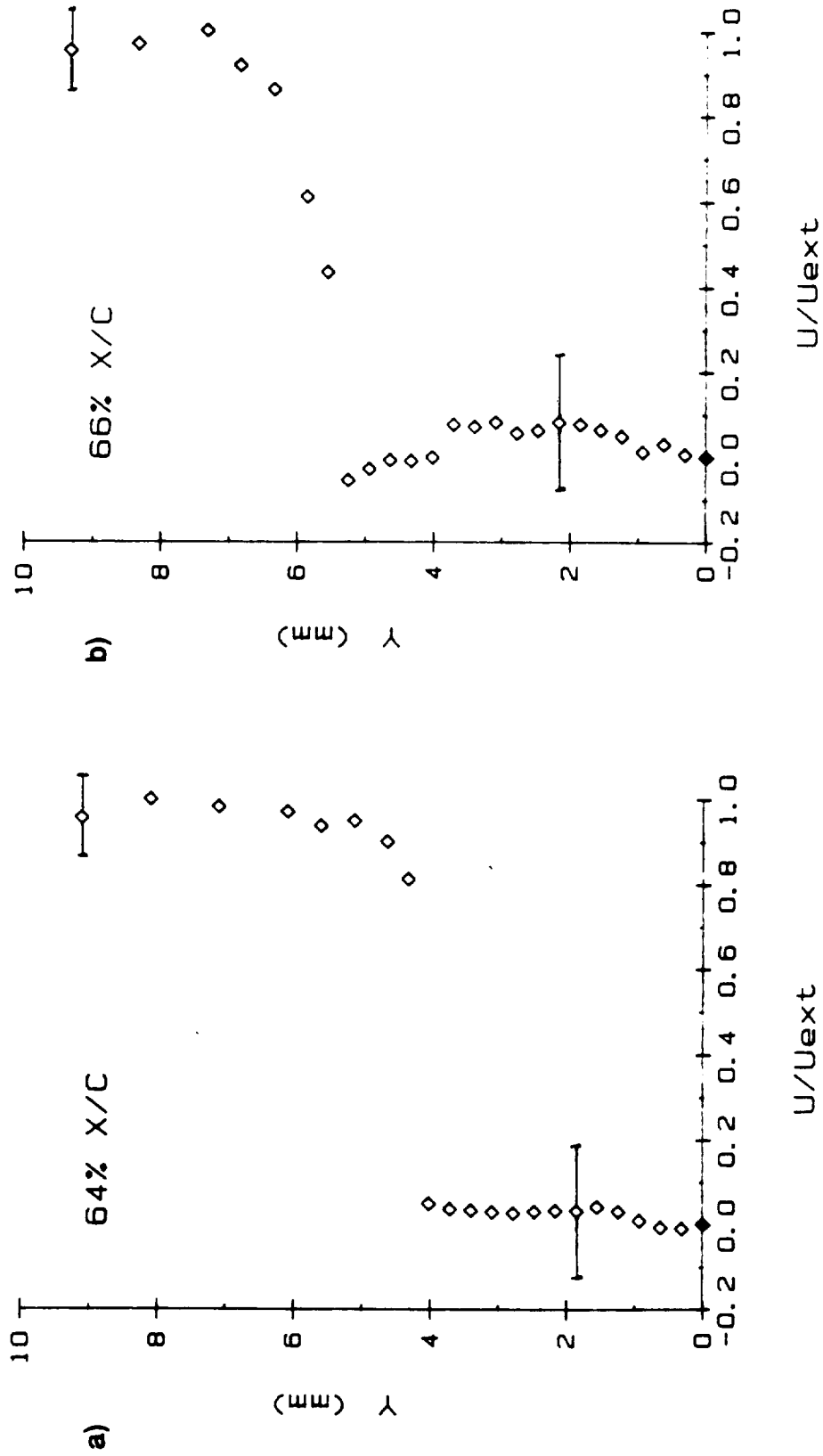
Figure 4.54 E387 Airfoil LDV U/U_{ext} Boundary Layer Velocity Profiles, 64% x/c and 66% x/c Chord Positions, R_c = 100,000 , α = 2.0°
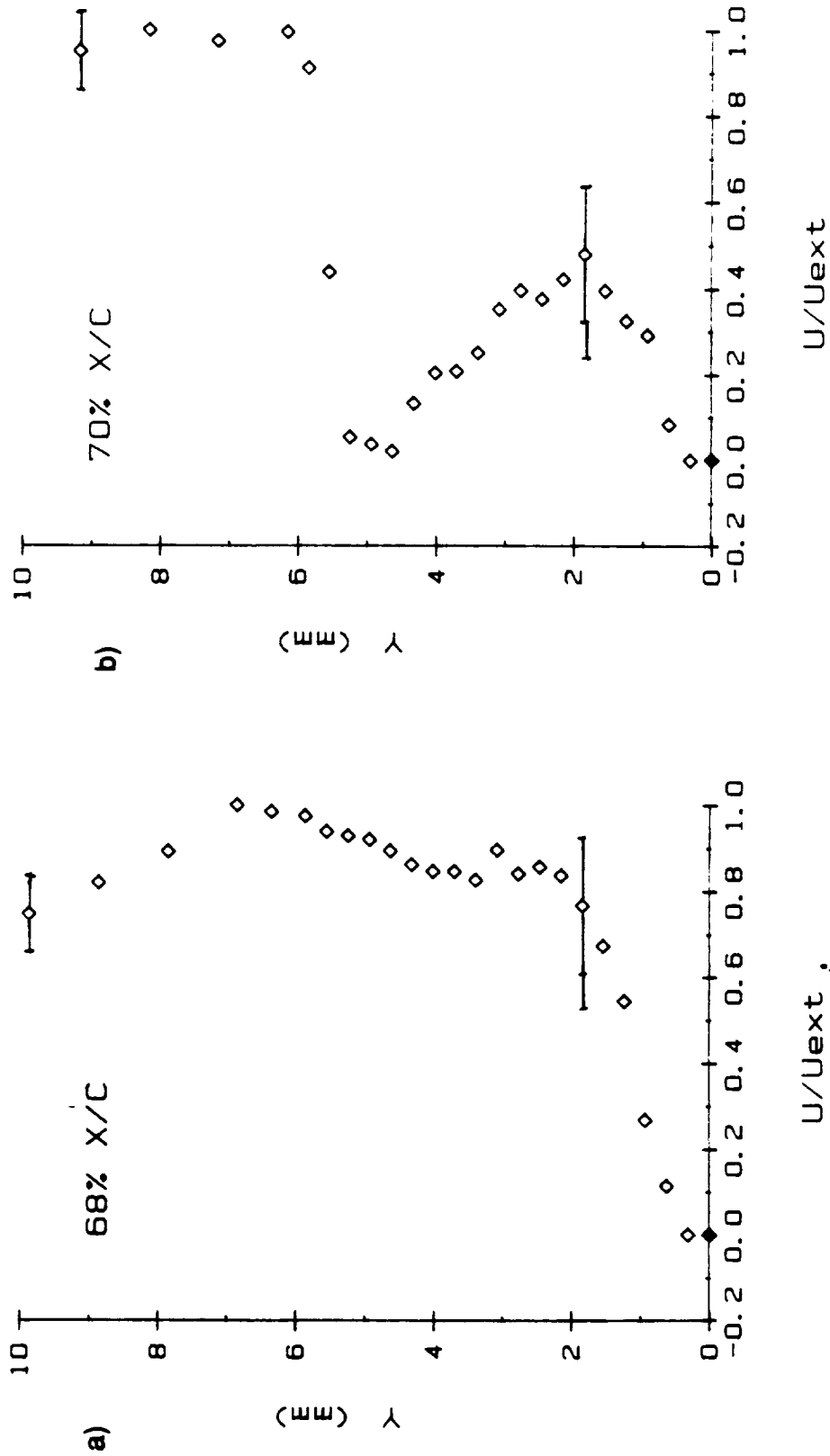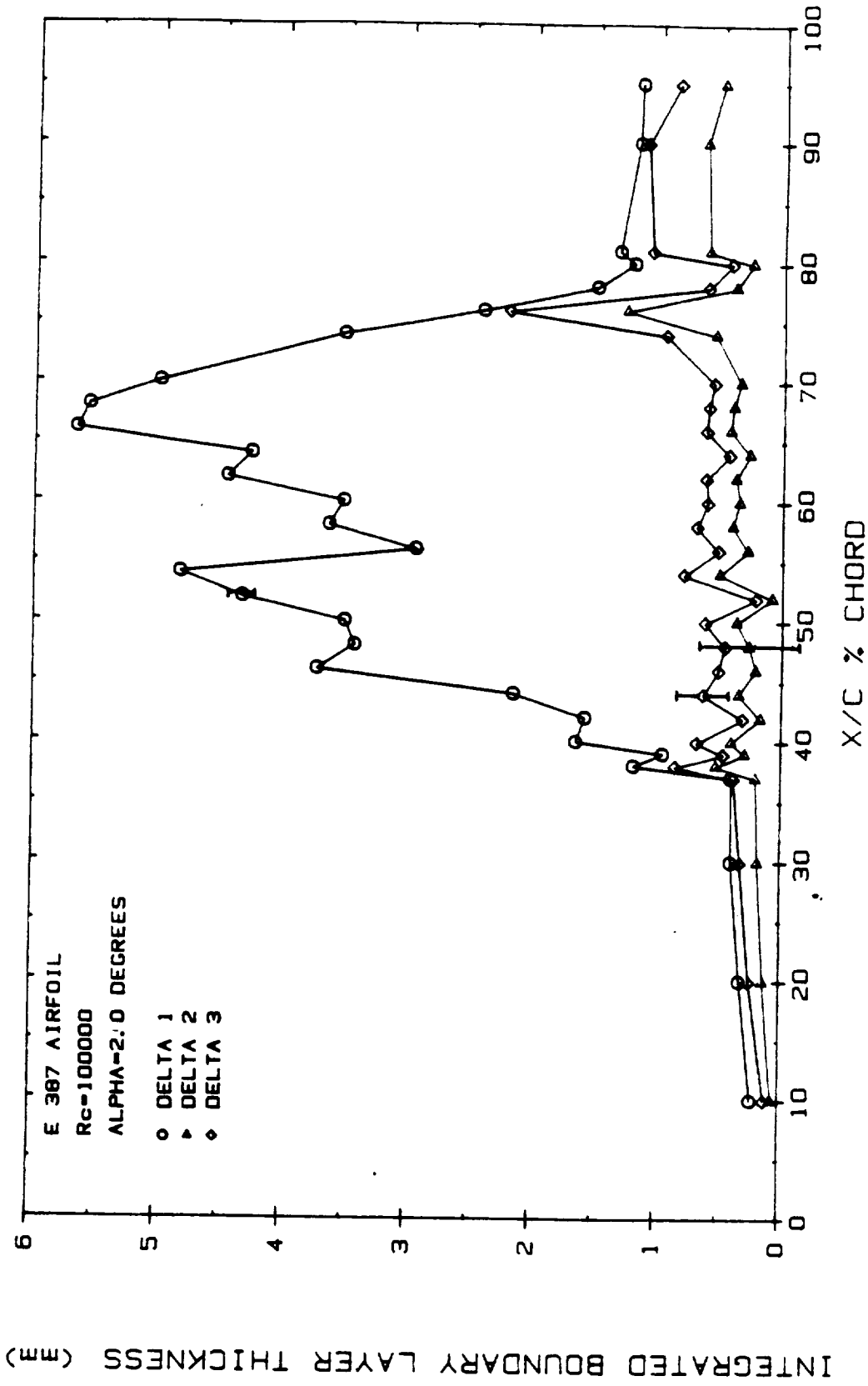
Figure 4.55   E387 Airfoil LDV U/U_{ext} Boundary Layer Velocity Profiles, 68% x/c and 70% x/c Chord Positions, R_c = 100,000 , α = 2.0°

Figure 4.56 E387 Airfoil LDV U/U$_{ext}$ Boundary Layer Velocity Profiles, 72% x/c and 74% x/c Chord Positions, R$_c$ = 100,000 , α = 2.0°

Figure 4.57 E387 Airfoil LDV U/U_{ext} Boundary Layer Velocity Profiles, 76% x/c and 78% x/c Chord Positions, $R_c = 100,000$, $\alpha = 2.0°$

Figure 4.58 E387 Airfoil LDV U/U_ext Boundary Layer Velocity Profiles, 80% x/c and 81% x/c Chord Positions, $R_c = 100,000$, $\alpha = 2.0°$
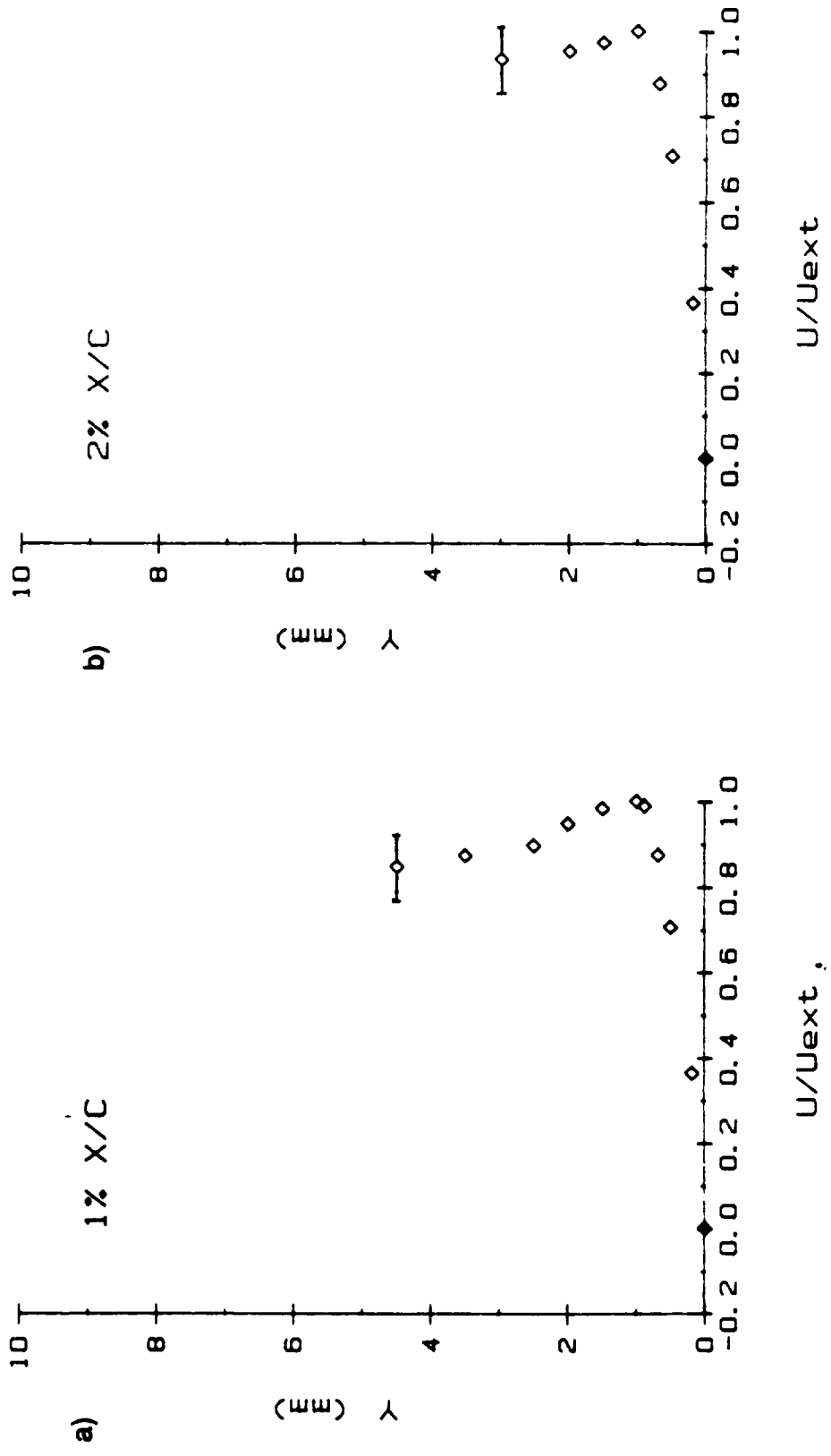
Figure 4.59 E387 Airfoil LDV U/U_{ext} Boundary Layer Velocity Profiles, 90% x/c and 95% x/c Chord Positions, R_c = 100,000 , α = 2.0°

Figure 4.60 Integrated Displacement, Momentum, and Energy Thicknesses for the E387 Airfoil, R_c = 100,000 and α = 2.0°
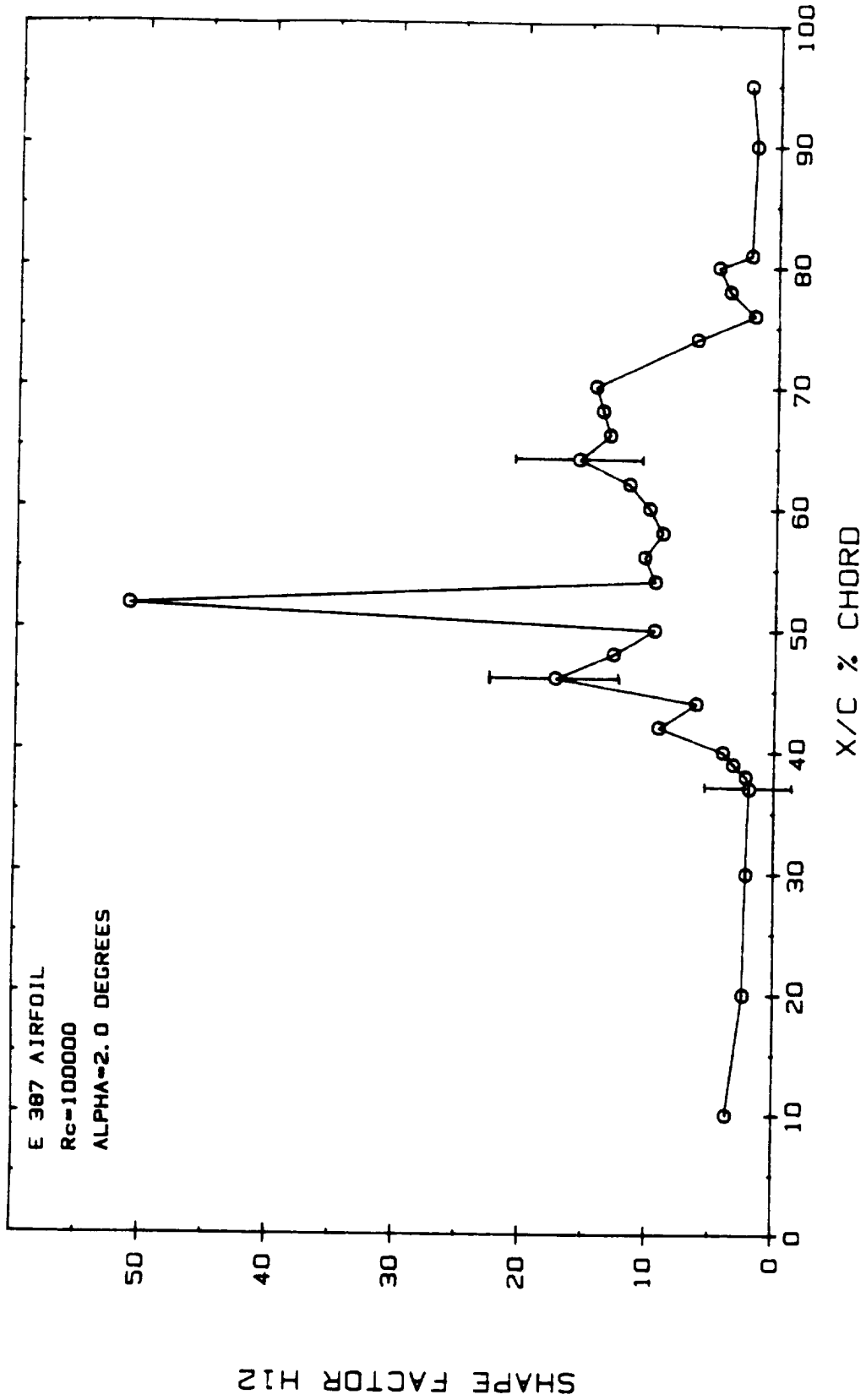
Figure 4.61 H_{12} Shape Factor Versus Chord Position
for the E387 Airfoil, R_c = 100,000 and α = 2.0°
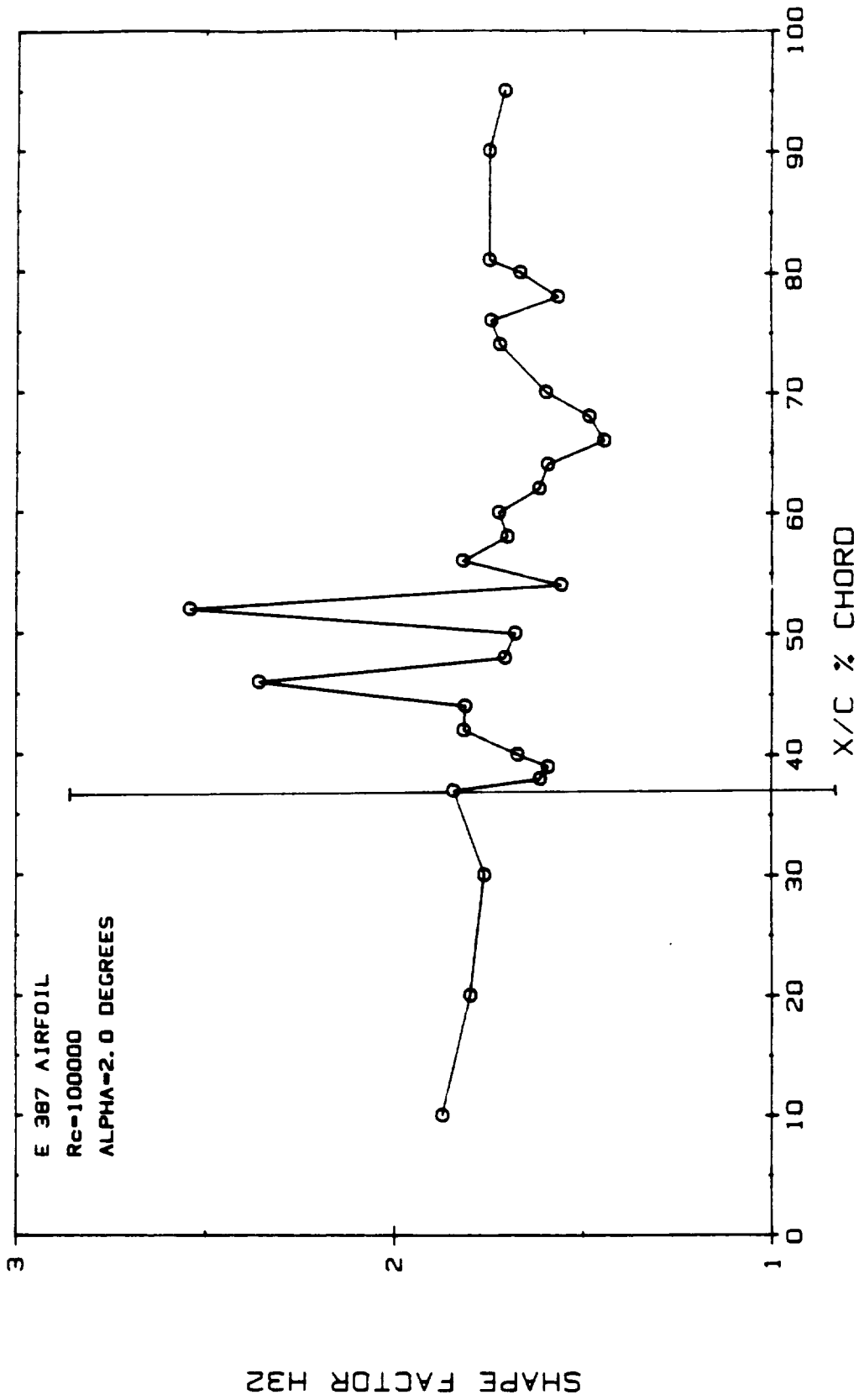
Figure 4.62 H_{32} Shape Factor Versus Chord Position for the E387 Airfoil, R_c = 100,000 and α = 2.0°

SHAPE FACTOR H32

X/C % CHORD

E 387 AIRFOIL
Rc=100000
ALPHA=2.0 DEGREES
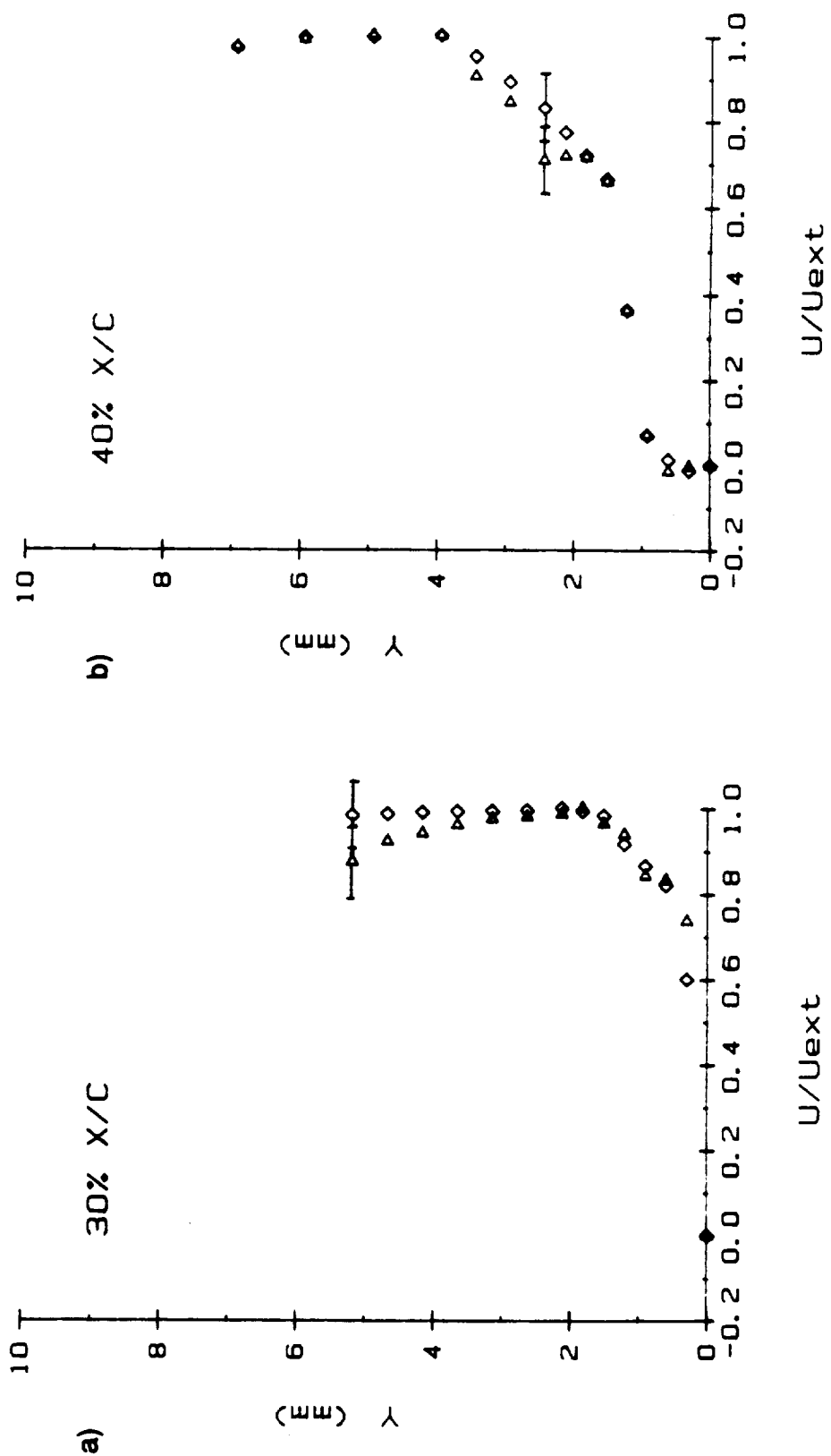
Figure 4.63 Repeatability comparison for LDV U/U_{ext} Boundary
Layer Velocity Profiles, $R_c = 100,000$, $\alpha = 2.0°$

NACA 663-018
Rc = 160.000
Alpha = 12 Degrees
0 Flow Restrictors
Uncorrected
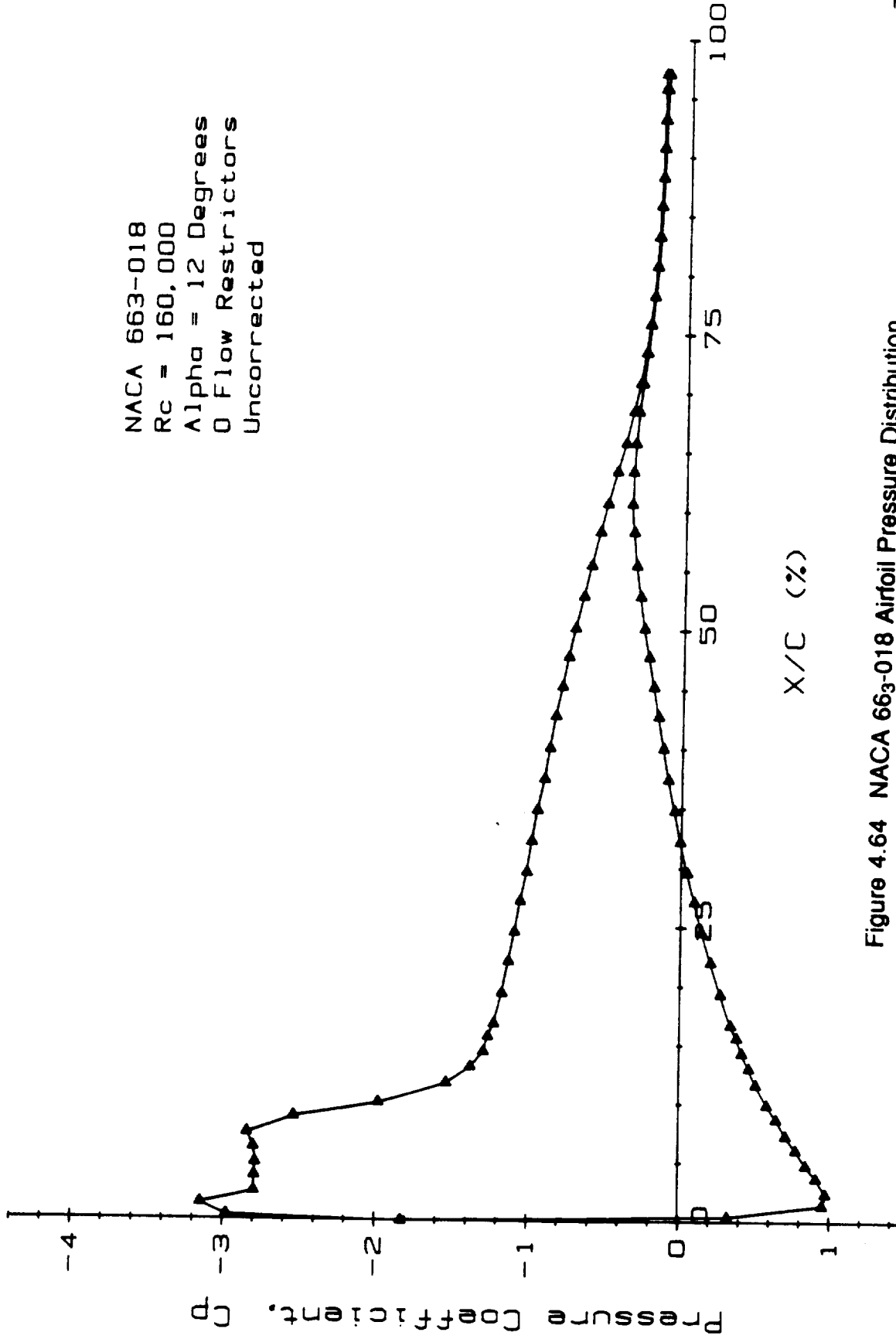
Figure 4.64 NACA 66₃-018 Airfoil Pressure Distribution
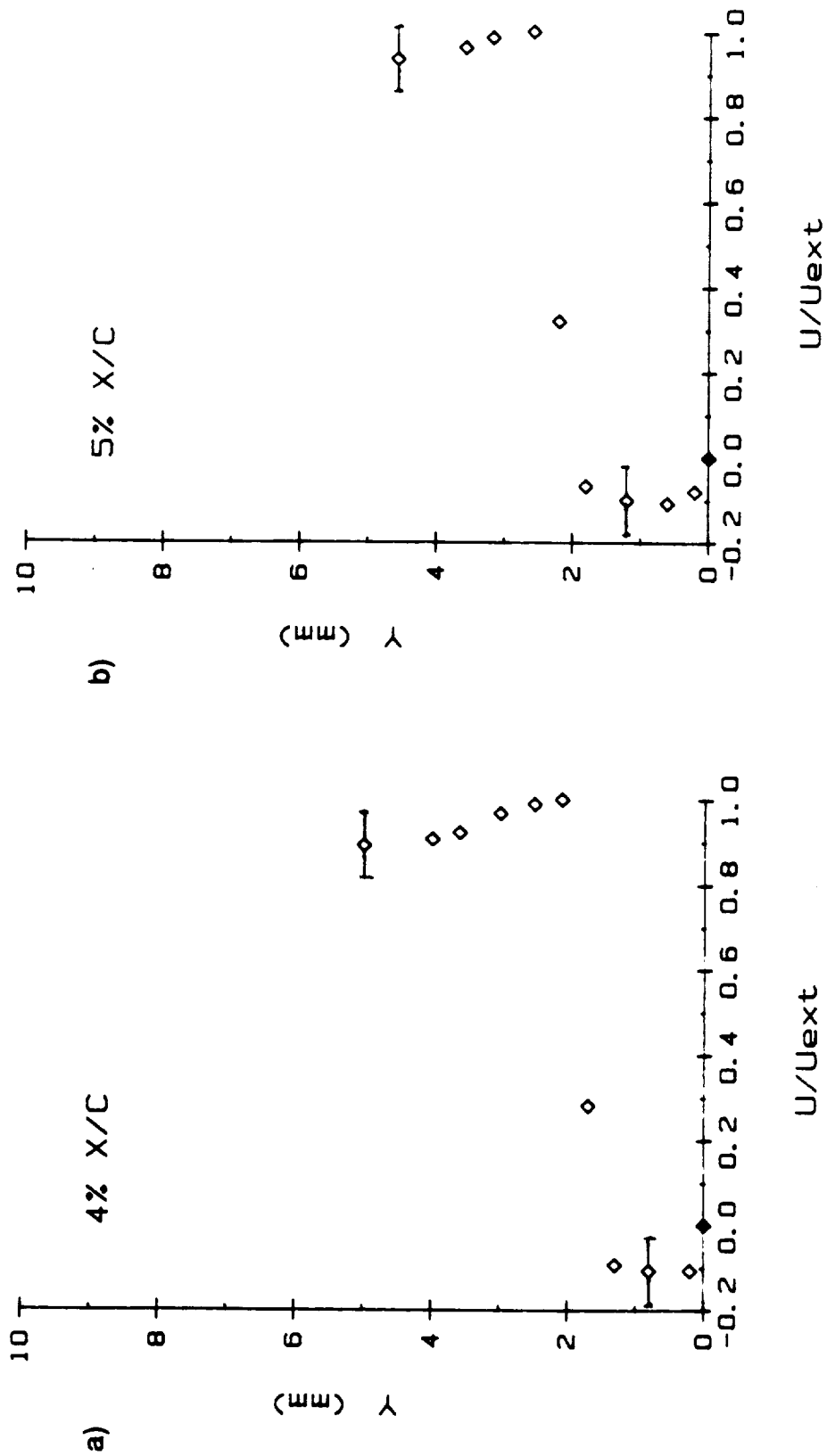R_c = 160,000 , α = 12.0°

Figure 4.65 NACA 66$_3$-018 Airfoil LDV U/U$_{ext}$ Boundary Layer Velocity Profiles, 1% x/c and 2% x/c Chord Positions, R$_c$ = 160,000 , α = 12.0°
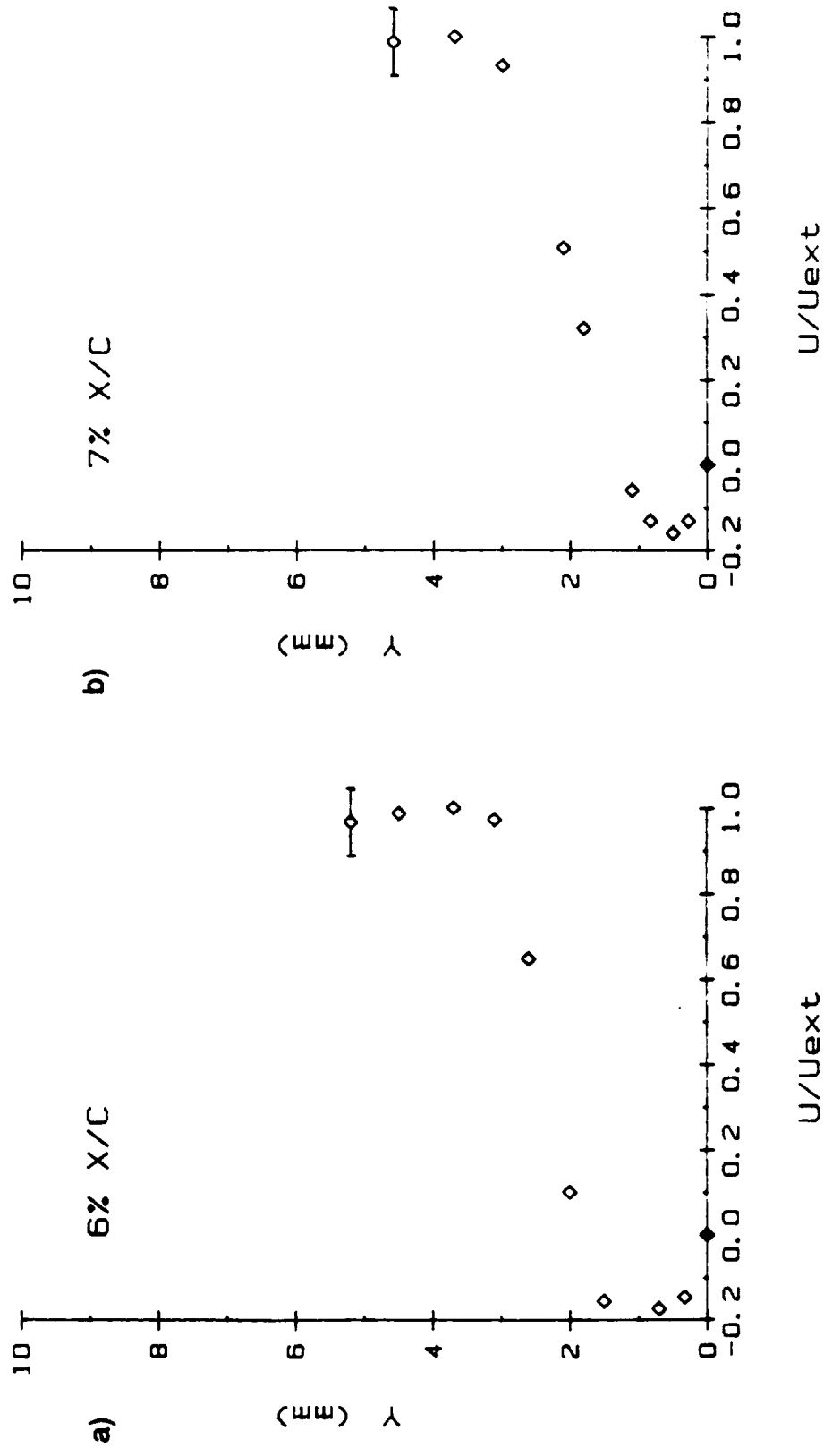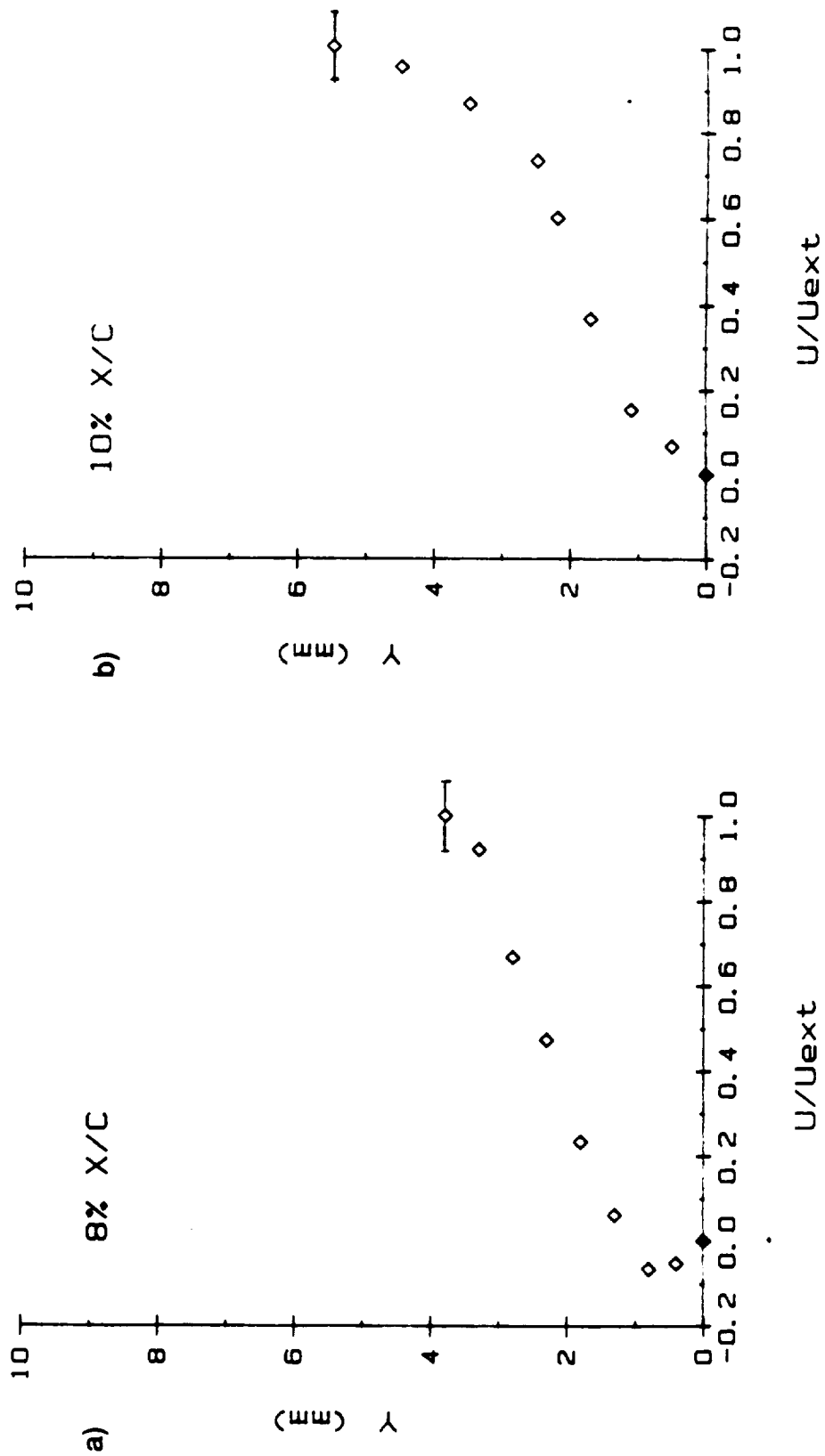
Figure 4.66 NACA 66₃-018 Airfoil LDV U/U_{ext} Boundary Layer Velocity Profiles, 4% x/c and 5% x/c Chord Positions, R_c = 160,000 , α = 12.0°

Figure 4.67 NACA 66₃-018 Airfoil LDV U/Uₑₓₜ Boundary Layer Velocity Profiles, 6% x/c and 7% x/c Chord Positions, R_c = 160,000 , α = 12.0°

Figure 4.68 NACA 66₃-018 Airfoil LDV U/U_ext Boundary Layer Velocity Profiles, 8% x/c and 10% x/c Chord Positions, $R_c = 160,000$, $\alpha = 12.0°$
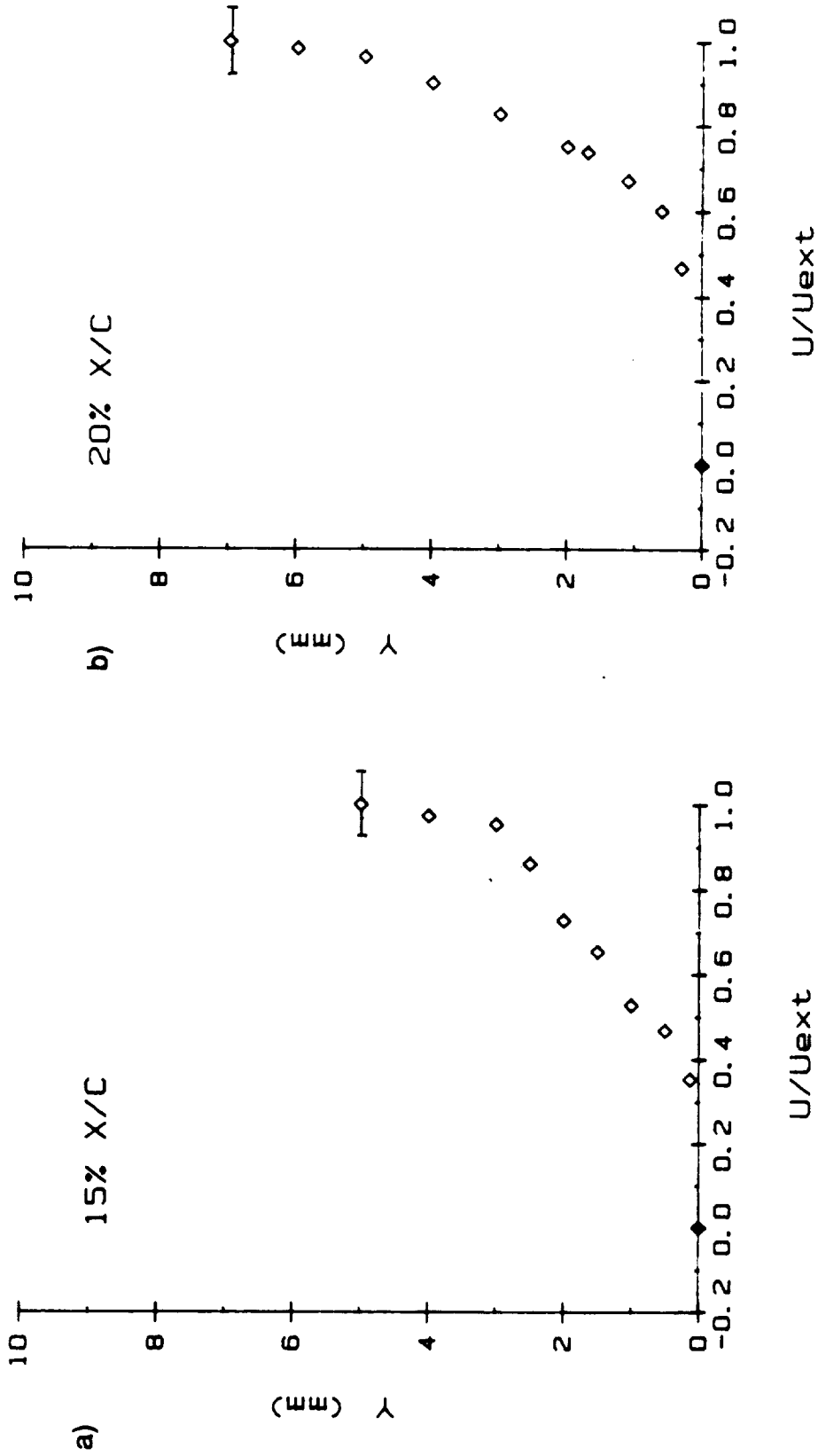
Figure 4.69 NACA 66_3-018 Airfoil LDV U/U_{ext} Boundary Layer Velocity Profiles, 15% x/c and 20% x/c Chord Positions, R_c = 160,000 , α = 12.0°
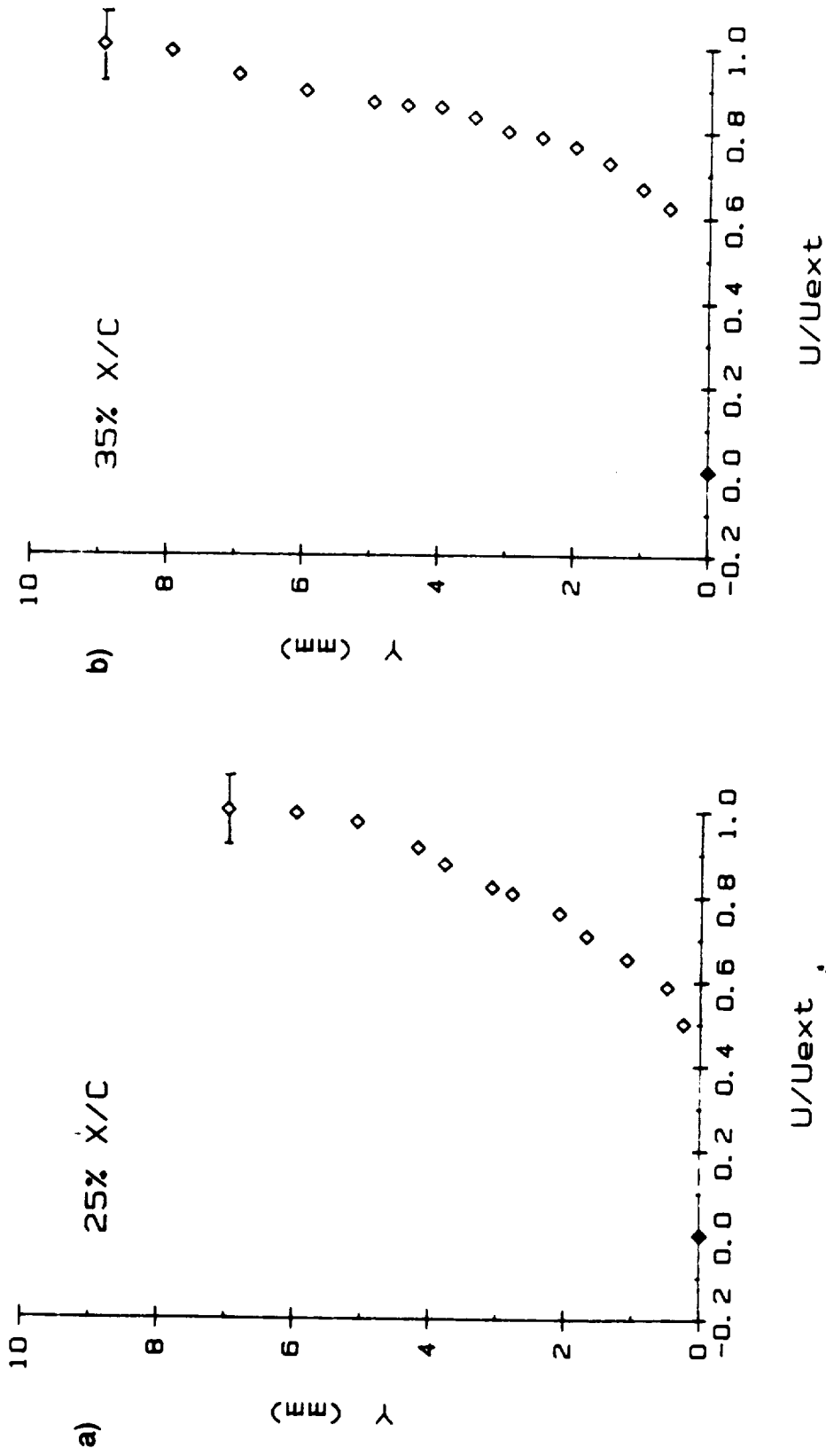
Figure 4.70 NACA 66₃-018 Airfoil LDV U/U_{ext} Boundary Layer Velocity Profiles, 25% x/c and 35% x/c Chord Positions, R_c = 160,000 , α = 12.0°
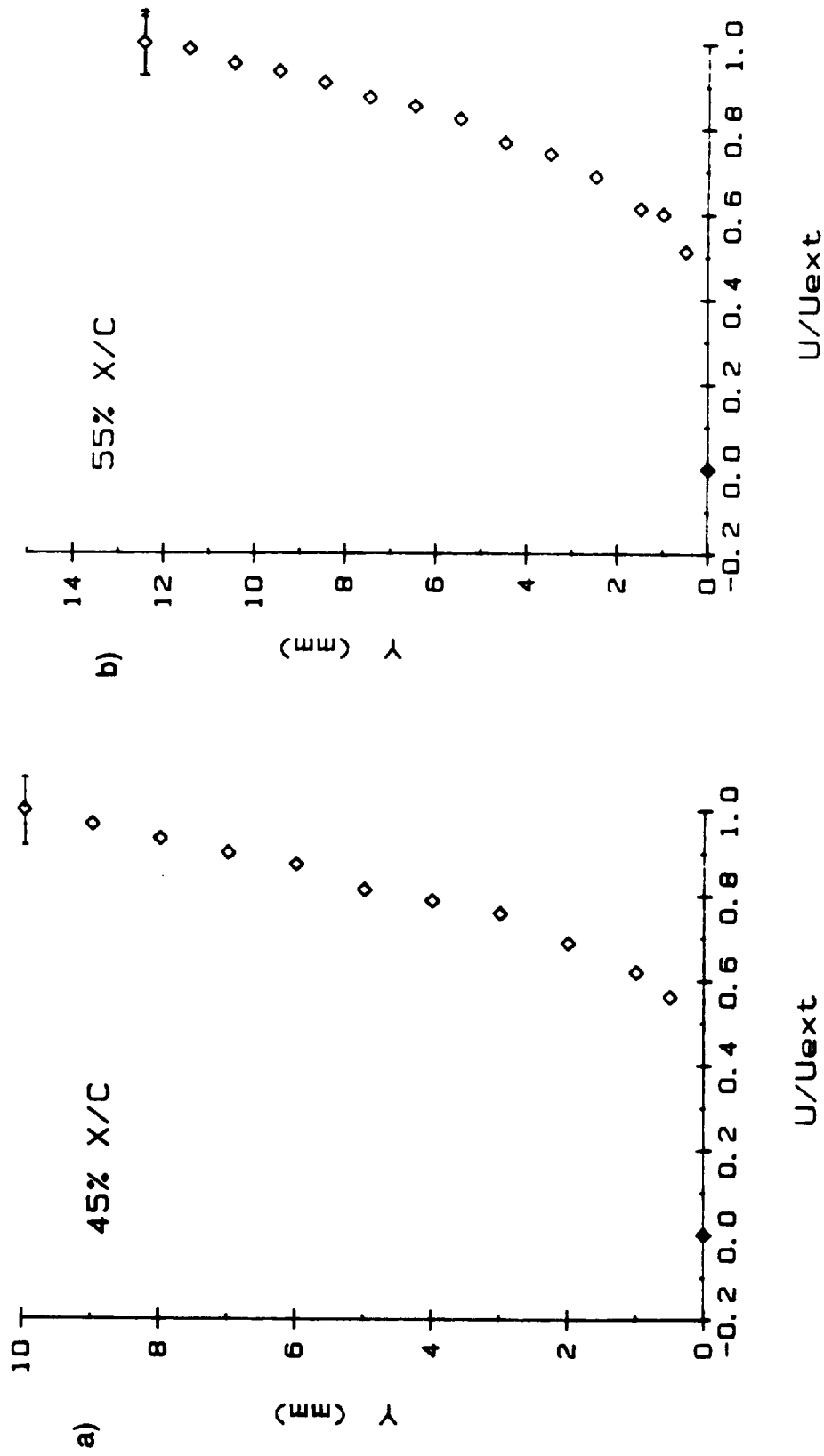
Figure 4.71 NACA 66₃-018 Airfoil LDV U/U_{ext} Boundary Layer Velocity Profiles, 45% x/c and 55% x/c Chord Positions, R_c = 160,000 , α = 12.0°
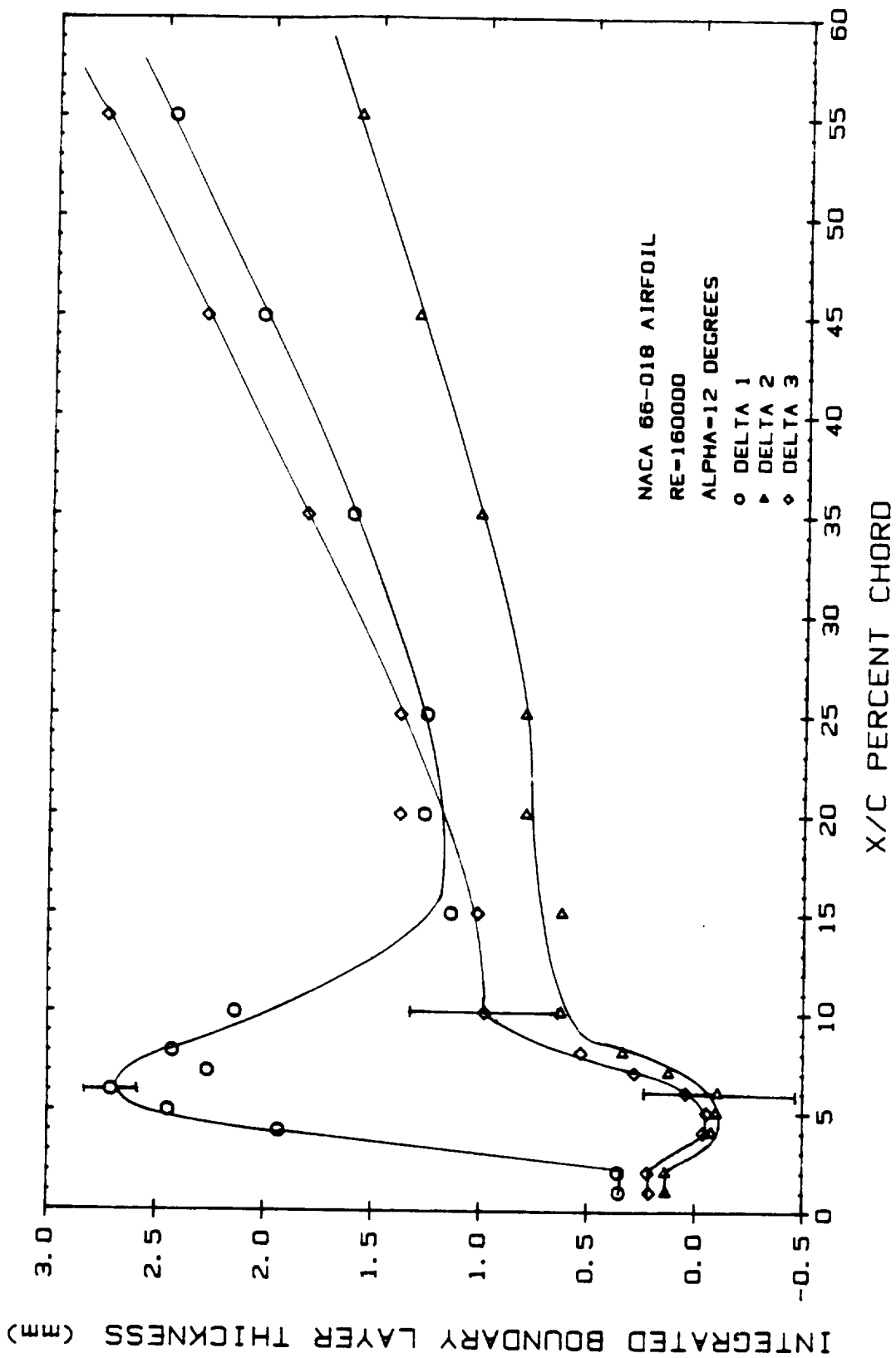
Figure 4.72 Integrated Displacement, Momentum, and Energy Thicknesses for the NACA 66_3-018 Airfoil, $R_c = 160,000$ and $\alpha = 12.0°$

NACA 66-018 AIRFOIL
RE=160000
ALPHA=12 DEGREES

X/C PERCENT CHORD
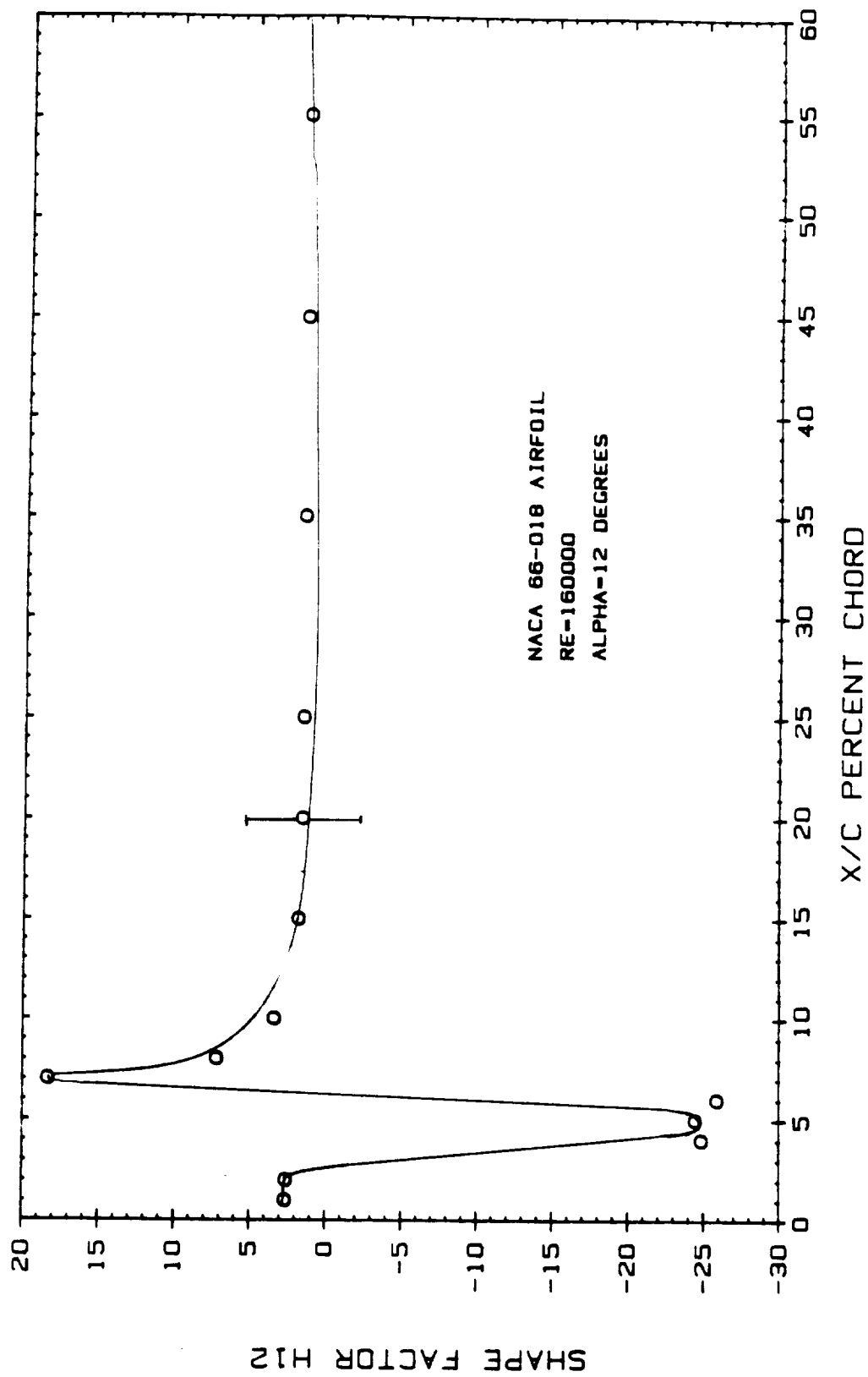
SHAPE FACTOR H12

Figure 4.73 H_{12} Shape Factor Versus Chord Position
for the NACA 66_3-018 Airfoil, R_c = 160,000 and α = 12.0°
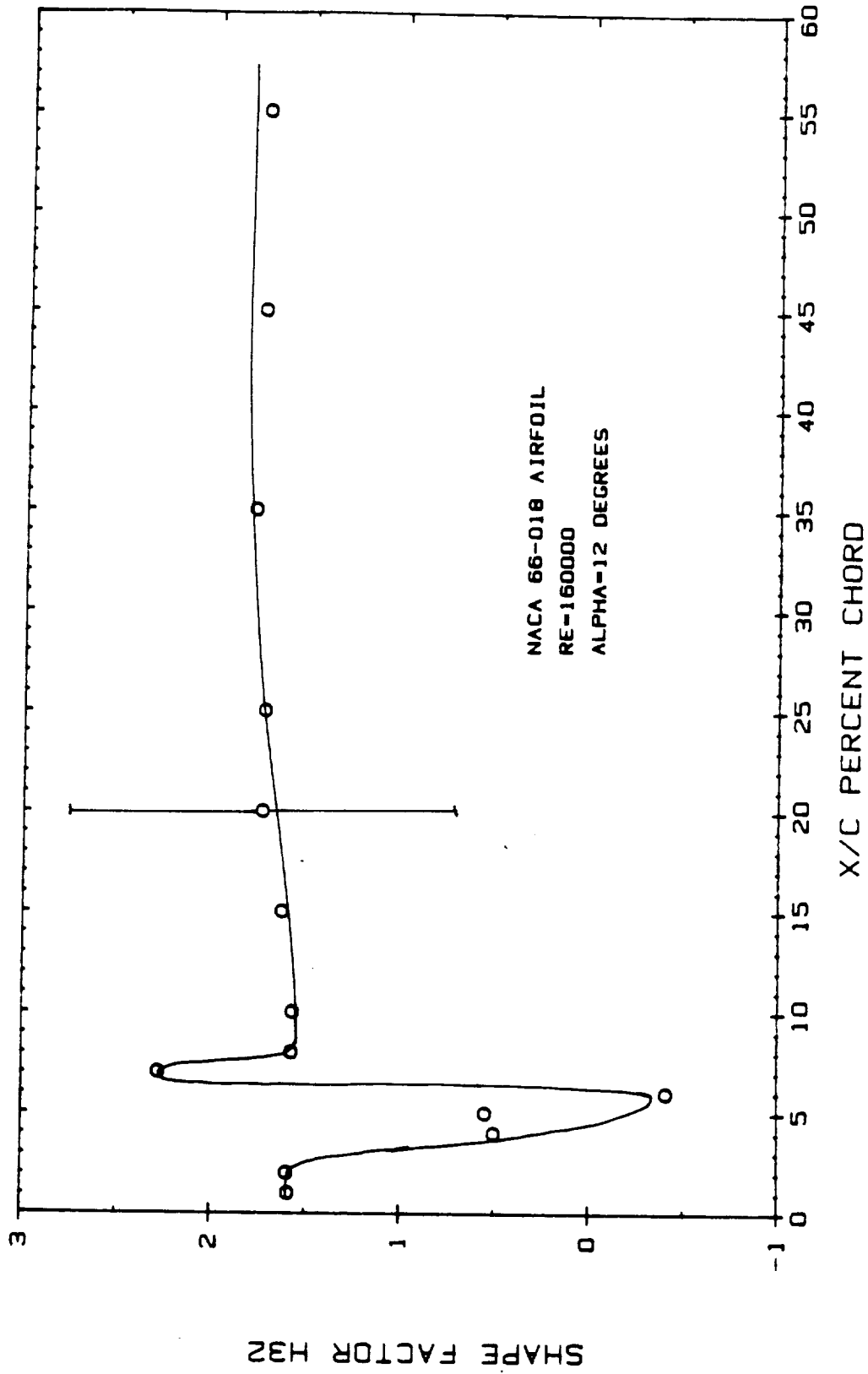
Figure 4.74 H_{32} Shape Factor Versus Chord Position
for the NACA 66_3-018 Airfoil, R_c = 160,000 and α = 12.0°

Figure 4.75   Laminar Separation Bubble Flow Visualization Photograph, E387 Airfoil included for Scale, R_c = 100,000 and α = 2.0°
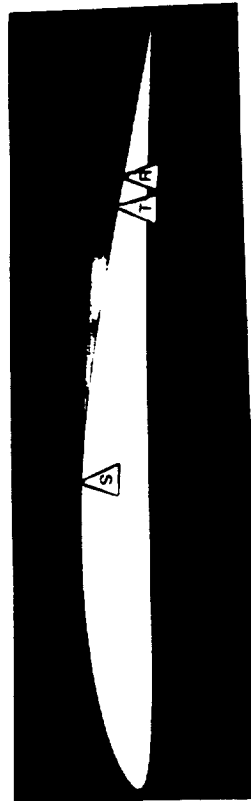
Figure 4.76 Laminar Separation Bubble Flow Visualization Photograph, E387 Airfoil, $R_c = 100,000$ and $\alpha = 2.0°$

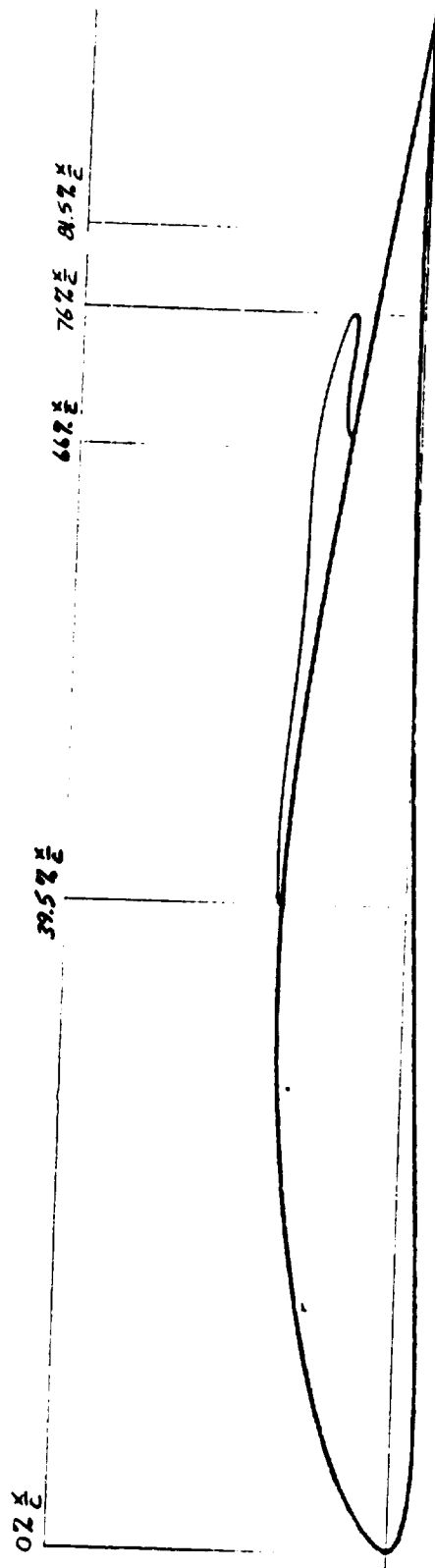Figure 4.77   Laminar Separation Bubble Flow Visualization Photograph, E387 Airfoil, R_c = 100,000 and α = 2.0°

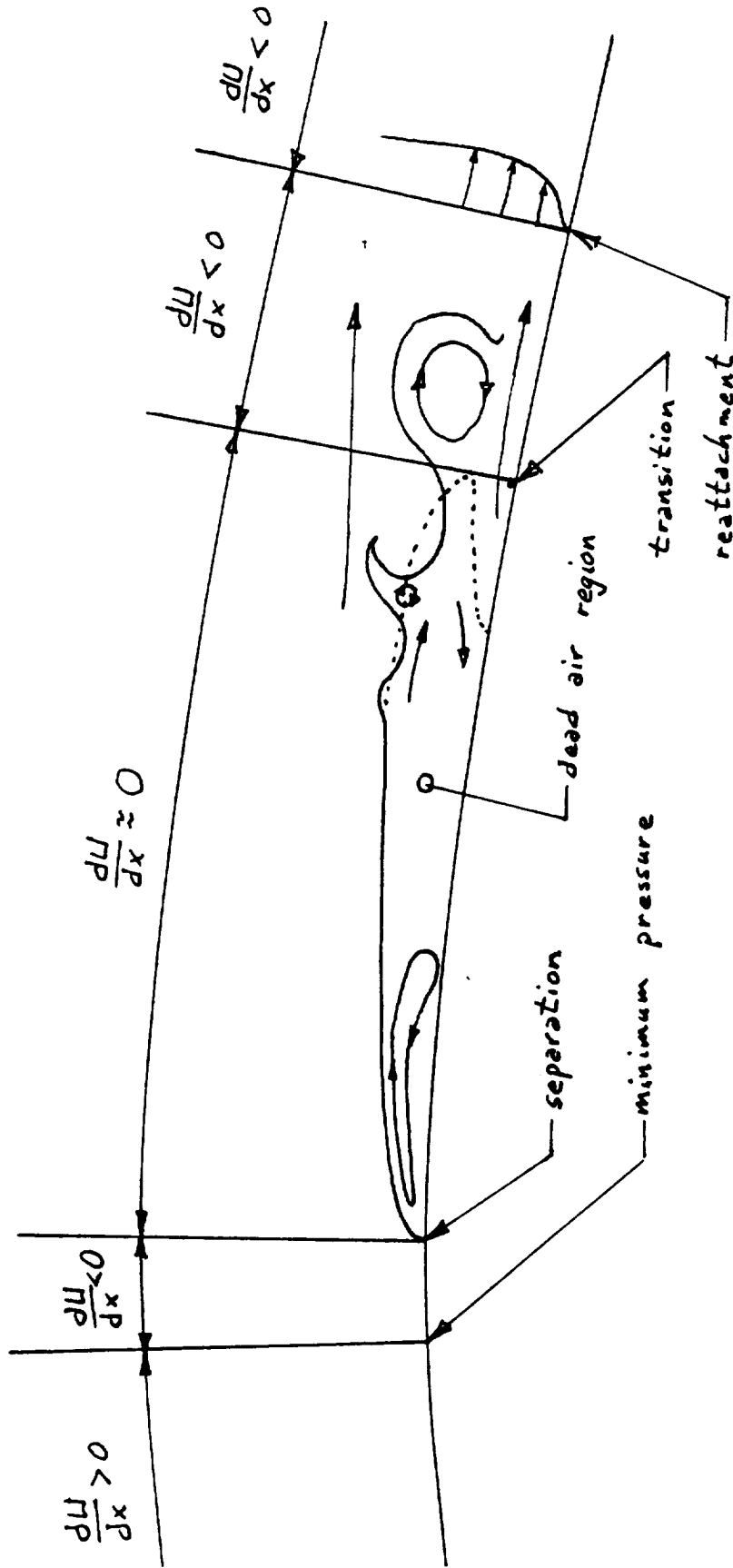Figure 4.78 E387 Airfoil Dividing Streakline Geometry, R_c = 100,000 , α =2.0°

Figure 5.1 E387 Laminar Separation Bubble Flow Field,
$R_c = 100{,}000$ and $\alpha = 2.0°$

REFERENCES

Althaus, D. (1986): "Recent Wind Tunnel Experiments at Low Reynolds Number, "Aerodynamics at Low Reynolds Numbers $10^4 <Re<10^6$ International Conference", Vol II Proceedings, October, pp. 18.1-18.42.

Batill, S. M. and T. J. Mueller (1980): "Visualization of the Laminar-Turbulent Transition in the Flow Over an Airfoil Using the "Smoke-Wire" Technique," AIAA Paper 80-0421.

Boermans, L. M. M., F. J. Donker Duyvis, and J. L. van Ingen (1989): "Experimental Aerodynamic Characteristics of the Airfoils LA 5055 and DU 86-084/18 at Low Reynolds Numbers," Conference on Low Reynolds Number Aerodynamics, Preliminary Proceedings, Editor T.J. Mueller, June.

Bogard, David G. and Tiederman, W. G. (1979): "Experimental Evaluation of Sampling Bias in Naturally Seeded Flows," *Laser Velocimetry and Particle Sizing*, edited by H. Doyle Thompson and Warren H. Stevenson, Hemisphere Publishing Corporation.

Brendel, M. (1986): "Experimental Study of the Boundary Layer on a Low Reynolds Number Airfoil in steady and Unsteady Flow," Ph.D. Dissertation, University of Notre Dame.

Brendel, M., and T. J. Mueller (1987): "Boundary Layer Measurements on an Airfoil at Low Reynolds Numbers," AIAA Paper 87-0495.

Drela, M. (1987): "Viscous-Inviscid Analysis of Transonic and Low Reynolds Number Airfoils," AIAA Journal, Vol. 25, No. 10, October.

Drela, M. (1988): "Low Reynolds Design for the M.I.T. Daedalus Prototype: A Case Study," Journal of Aircraft, Vol. 25, No. 8, August.

Drela, M. (1989): "XFOIL: An Analysis and Design System for Low Reynolds Number Airfoils," Conference on Low Reynolds Number Aerodynamics, Preliminary Proceedings, Editor T.J. Mueller, June.

Eppler, R. and D. M. Somers (1980): "A Computer Program for the Design and Analysis of Low-Speed Airfoils," NASA TM 80210, August.

Eppler, R. (1986): "Recent Developments in Boundary Layer Computation, "Aerodynamics at Low Reynolds Numbers $10^4 <Re<10^6$ International Conference", Vol. II Proceedings, October, pp. 12.1-12.18.

Fitzgerald, E. J. (1988): "Experimental Studies of the Transitional Separation Bubble on the NACA 66_3-018 Airfoil at Low Reynolds Numbers," M.S. Thesis, University of Notre Dame.

Hamma, F. R. (1962): "Streaklines in a Perturbed Shear Flow," The Physics of Fluids, Vol. 5, No. 6, pp. 644-650

Horstmann, K. H., and A. Quast (1981): "Reduction of Section Drag By Blowing Through Rows of Holes in Areas of Laminar Separation Bubbles," Technical Soaring, Vol. VII, No. 1, September.

Horton, H. P. (1968): "Laminar Separation Bubbles in Two and Three Dimensional Incompressible Flow," Ph.D. Thesis, University of London.

Ingen, J. L. van, and L. M. M. Boermans (1985): "Research on Laminar Separation Bubbles at Delft University of Technology in Relation to Low Reynolds Number Airfoil Aerodynamics," Proceedings of the Conference on Low Reynolds Number Airfoil Aerodynamics, UNDAS-CP-77B123, University of Notre Dame, June, pp. 89-124.

Marchman, J. F. (1987): "Aerodynamic Testing at Low Reynolds Numbers," Journal of Aircraft, Vol. 24, No. 2, February.

McGhee, Robert J. , Betty S. Walker, and Betty F. Millard (1988): Experimental Results for the Eppler 387 Airfoil at Low Reynolds Numbers in the Langley Low-Turbulence Pressure Tunnel," NASA Technical Memorandum 4062, October.

McMasters, J. H., and M. L. Henderson (1979): "Low-Speed Single-Element Airfoil Synthesis," Technical Soaring, Vol. VI, No. 2.

Meyers, James F. (1979): "Applications of Laser Velocimetry To Large Scale and Specialized Aerodynamic Tests," TSI Quarterly, Vol. V, Issue 4, December.

Mueller, T. J. (1985): "Low Reynolds Number Vehicles," AGARDograph No. 288.

Mueller, T. J. (1985): "The Influence of Laminar Separation and Transition on Low Reynolds Number Airfoil Hysteresis," Journal of Aircraft, Vol. 22, No. 9, September, pp 763-770.

Mueller, T. J., and S.M. Batill (1980): "Experimental Studies of the Laminar Separation Bubble on a Two-Dimensional Airfoil at Low Reynolds Numbers," AIAA Paper 80-1440.

O'Meara, M. M. (1985): "An Experimental Investigation of the Separation Bubble Flow Field Over an Airfoil at Low Reynolds Numbers," M.S. Thesis, University of Notre Dame.

O'Meara, M. M., and T.J. Mueller (1987): "Laminar Separation Bubble Characteristics on an Airfoil at Low Reynolds Numbers," AIAA Journal, Vol. 25, No. 8, August, pp. 1033-1041.

Pfenninger, W., and C. S. Vemura (1988): "Design of Low Reynolds Number Airfoils-I," AIAA Paper 88-2572-CP.

Russell, John M. (1979): "Length and Bursting of Separation Bubbles: A Physical Interpretation," Science and Technology of Low Speed and Motorless Flight, NASA Conference Publication 2085 part I.

Selig, M. S. (1984): "The Design of Airfoils at Low Reynolds," Soartech III, published by H. A. Stokely, 1504 Horseshoe Circle, Virginia Beach, VA, 23451.

Schmidt, G. S. (1986): "The Prediction of Transitional Separation Bubbles at Low Reynolds Numbers," Ph.D. Dissertation, University of Notre Dame.

Visser, K. D. (1988): Preliminary Departmental Particle Sizing Report, University of Notre Dame.